Condition/Health Monitoring of Railroad Bridges for Structural Safety, Integrity, and Durability

Final Report
November 2022

Principal Investigator: Ramesh B. Malla, Ph.D., F. ASCE, F. EMI, Professor
UConn Institutional Lead for US DOT Region 1 UTC-TIDC Program
Department of Civil & Environmental Engineering, University of Connecticut, Storrs, CT

Authors
Ramesh B. Malla, Ph.D., F. ASCE, F. EMI, A.F. AIAA, M. CASE (Professor),
Celso de Oliveira, Research Assistant (Ph.D. Student), and
Santosh Dhakal (M.S. Student).

Sponsored By
Transportation Infrastructure Durability Center
U.S. Department of Transportation, University Transportation Center Programs

TIDC
Transportation Infrastructure Durability Center
AT THE UNIVERSITY OF MAINE

A report from
University of Connecticut
Department of Civil & Environmental Engineering
261 Glenbrook Road. Unit - 3037
Storrs, CT 06269-3037, U.S.A.
Phone: +1 (860) 486-2992
Website: http://malla.engr.uconn.edu

THE UNIVERSITY OF MAINE 1865 · UMASS LOWELL · WESTERN NEW ENGLAND UNIVERSITY WNE · UCONN · THE UNIVERSITY OF RHODE ISLAND · The UNIVERSITY of VERMONT

About the Transportation Infrastructure Durability Center

The Transportation Infrastructure Durability Center (TIDC) is the 2018 US DOT Region 1 (New England) University Transportation Center (UTC) located at the University of Maine Advanced Structures and Composites Center. TIDC's research focuses on efforts to improve the durability and extend the life of transportation infrastructure in New England and beyond through an integrated collaboration of universities, state DOTs, and industry. The TIDC is comprised of six New England universities, the University of Maine (lead), the University of Connecticut, the University of Massachusetts Lowell, the University of Rhode Island, the University of Vermont, and Western New England University.

U.S. Department of Transportation (US DOT) Disclaimer

Acknowledgements

Funding for this research is in part provided by the Transportation Infrastructure Durability Center at the University of Maine under grant 69A3551847101 from the U.S. Department of Transportation's University Transportation Centers Program. The principal investigator of the project would like to acknowledge and thank the following individuals and organizations whose support (financial, material, and/or in-kind) assisted in this research and significantly contributed to the success of the project:

Graduate assistants involved in this project:

Celso de Oliveira, Ph.D. student
Santosh Dhakal, M.S. student
Sachin Tripathi, Ph.D. student
Mark Castaldi, M.S. Student

The following members of the project's Expert Panel for their time and attention by serving as technical champions and providing many valuable comments during the course of this project:

Mr. Haresh Dholakia, P.E., Transportation Engineering Supervisor, Rail Design (ConnDOT)
Mr. Manesh Dodia, P.E., Supervising Rail Officer, Rail Construction (ConnDOT)
Mr. Warren Best, P.E., Deputy Director- Structures (Metro-North Railroad Company)

The Connecticut Department of Transportation, Newington, Connecticut, for their support making the Devon railroad bridge and the Cos Cob railroad bridge available for testing and other in-kind contribution (Contact: Mr. Haresh Dholakia and Mr. Manesh Dodia).

Metro-North Railroad Company for facilitating access to the Devon and the Cos Cob railroad bridge and other in-kind contribution (Contact: Mr. Warren Best and Ms. McConnel Hong, Senior Structural Engineer).

Polytec, Inc., Hudson, MA for providing field test equipment (Single Point Laser Doppler Vibrometer), data processing software, software and equipment training and other in-kind contribution. (Contact: Mario Pineda, Territory Manager; Arend Von der Lieth, Application Engineering Manager and David Damiani, Application Engineer).

Amtrak, Philadelphia, PA for continued support and providing the train specifications. (Contact: Paul DelSignore, Deputy Chief Engineer – Structures; René S. Asuncion, Sr. Principal Engineer - Structures Maintenance and Inspection, and David Inman, Sr. Engineer, Structures-Movable Bridges).

Dr. Lesley D. Frame, Assistant Professor, Department of Material Science at University of Connecticut for providing feedback during the material testing.

Western New England University (WNEU), Springfield, MA for providing access to the material testing laboratory. (Contact: Dr. Moochul Shin and Dr. Lisa K. Murray).

Dr. Nicholas Eddy at the Department of Material Science, University of Connecticut for the access and the training with the tensile testing machine.

The following University of Connecticut Civil & Environmental Engineering Department graduate students who assisted significantly in the field testing:

Supporting Role:

- Suvash Dhakal, Civil Engineering (Ph.D. Candidate)
- David Jacob, Civil Engineering (Graduate in Ph.D., May 2021)
- Sachin Tripathi, Civil Engineering (Ph.D. Student)
- Francis Almonte, Materials Science and Engineering (M.S. Student)

Undergraduate Students:

- Hernan Cortez, Civil Engineering
- Sean Doolittle, Chemical Engineering
- Liam Gerety, Material Science and Engineering
- Stephanie Kreitler, Civil Engineering
- Andrew Schroder, Civil Engineering
- Kelly Voong, Civil Engineering
- Max Raha, Civil Engineering

Special thanks to Sushrut Vaidya, Ph.D., and Sachin Tripathi for proofreading the report and providing valuable comments/edits.

Last, but not least, the University of Connecticut, its Department of Civil and Environmental Engineering, and Connecticut Transportation Institute (CTI) for cost share, in-kind support, laboratory facilities, and project administration help.

Technical Report Documentation Page

1. Report No.	2. Government Accession No.	3. Recipient Catalog No.
4 Title and Subtitle Condition/Health Monitoring of Railroad Bridges for Structural Safety, Integrity, and Durability		**5 Report Date** November 30, 2022 **6 Performing Organization Code**
7. Author(s) Ramesh B. Malla: https://orcid.org/0000-0002-8035-8402 Celso de Oliveira: https://orcid.org/0000-0002-6074-8358 Santosh Dhakal: https://orcid.org/0000-0001-8806-7725		**8 Performing Organization Report No.**
9 Performing Organization Name and Address University of Connecticut, Department of Civil & Environmental Engineering, 261 Glenbrook Road, Storrs, Connecticut 06269-3037, U.S.A.		**10 Work Unit No. (TRAIS)** **11 Contract or Grant No.**
12 Sponsoring Agency Name and Address U.S. DOT Region 1 University Transportation Center (UTC) -Transportation Infrastructure Durability Center (TIDC), ASCC, University of Maine, 35 Flagstaff Rd., Orono, Maine, U.S.A.		**13 Type of Report and Period Covered** Final Report: 10/01/2018 to 9/30/2022 **14 Sponsoring Agency Code**
15 Supplementary Notes		

16 Abstract

Long-haul passenger, commuter, and freight railroads are essential to maintaining a thriving economy, especially in New England, with its many urban areas, industries, and significant national defense activities. Amtrak's Northeast Corridor (NEC) is the busiest passenger rail corridor in the United States (US). The US Department of Transportation and the Federal Railroad Administration have designated NEC as the country's highest priority route for upgrading high-speed rail. In addition, freight service is a vital economic driver; a single train can carry the freight of several hundred trucks, reducing highway gridlock, the cost of maintaining existing highways, and the need to build expensive new ones. Unfortunately, many of the region's rail bridges are old and exhibit unusual characteristics due to wear and tear. This report presents the health monitoring methodologies for structural safety and integrity of old railroad bridges, using material study, field-testing and computational modeling.

The report starts with a description of the dynamic structural theory of railroad bridges due to moving vehicles. Then, the tensile tests performed on original materials from the bridge replaced during maintenance are discussed, including the analysis of test results in accordance with ASTM specifications. Subsequently, the time- and frequency-domain analyses of the bridge response data recorded during the field tests on the selected bridges to extract the dynamic structural response characteristics of the bridge structure are described. Finally, detailed descriptions of Finite Element (FE) models of the respective bridges are given, and the results of FE simulations are compared against those obtained from the field data. The outcome is a correlation between the field test data and the predictions of the dynamic theory of bridge spans under moving vehicle loads. Interpretations of the field test observations using theoretical results are provided. The material tensile test results have shown consistency with values recommended by the design codes. Similarly, the results presented here have shown a reasonable agreement between the theoretical values, field test data and computational models. The methodology presented in this report can be applied to better understand and help mitigate dynamic structural problems encountered in typical railroad bridges.

17 Key Words	18 Distribution Statement		
Railroad Bridges, Bridge Monitoring, Laser Doppler Vibrometer, Accelerometers, Dynamic Response, Displacement, Velocity, Acceleration, Finite Element Model, Field Testing, Railroad Bride Material Testing	No restrictions. This document is available to the public through…		
19 Security Classification (of this report) Unclassified	**20 Security Classification (of this page)** Unclassified	**21 No. of pages** 126	**22 Price**

Form DOT F 1700.7 (8-72)

Table of Contents

List of Figures

List of Tables

List of Key Terms

AREMA: American Railway Engineering and Maintenance-of-Way Association.

ASTM: American Society of Testing and Materials.

CONN DOT (CT DOT): Connecticut Department of Transportation.

FE: Finite Element.

FRA: Federal Railroad Administration.

HSR: High Speed Rail (110 to 160 MPH).

LDV: Laser Doppler Vibrometer.

MAS: Maximum Allowable Speed (MAS).

MTNR: Metro-North Railroad Company.

NEC: Northeast Corridor.

SHMS: Structural Health Monitoring System.

US DOT: United States Department of Transportation.

Table of Conversions

Unitary Value	Unit	Equivalent Value	Unit
1.0	lbs	4.44	N
1.0	ksi	6.9	MPa
1.0	inch	25.4	mm
1.0	feet	304.8	mm
1.0	mph	1.61	km/h
1.0	Hz	6.28	rad/sec

Abstract

Long-haul passenger, commuter, and freight railroads are essential to maintaining a thriving economy, especially in New England, with its many urban areas, industries, and significant national defense activities. Amtrak's Northeast Corridor (NEC) is the busiest passenger rail corridor in the United States (US). In addition, state-owned rail commuter operations provide trains along the entire southern coastline of Connecticut and serve major urban areas such as Hartford and New Haven in Connecticut, Springfield and Boston in Massachusetts, and Providence, Rhode Island. The US Department of Transportation and the Federal Railroad Administration have designated NEC as the country's highest priority route for upgrading high-speed rail. In addition, freight service is a vital economic driver; a single train can carry the freight of several hundred trucks, reducing highway gridlock, the cost of maintaining existing highways, and the need to build expensive new ones. Sustaining a viable railroad system in New England requires that infrastructure be maintained through capital investments to upgrade, improve, or replace facilities. Unfortunately, many of the region's rail bridges are old and exhibit unusual characteristics due to wear and tear. This report presents the health monitoring methodologies for structural safety and integrity of old railroad bridges, using material study, field-testing and computational modeling.

The report starts with a description of the dynamic structural theory of railroad bridges due to moving vehicles. Then, the tensile tests performed on original materials from the bridge replaced during maintenance are discussed, including the analysis of test results in accordance with ASTM specifications. Subsequently, the time- and frequency-domain analyses of the bridge response data recorded during the field tests on the selected bridges to extract the dynamic structural response characteristics of the bridge structure are described. Finally, detailed descriptions of Finite Element (FE) models of the respective bridges are given, and the results of FE simulations are compared against those obtained from the field data. The outcome is a correlation between the field test data and the predictions of the dynamic theory bridge spans under moving vehicle loads. Interpretations of the field test observations using theoretical results are provided.

The material tensile test results have shown consistency with values recommended by the design codes. Similarly, the results presented here have shown a reasonable agreement between the theoretical values, field test data, and computational models. The methodology presented in this report can be applied to better understand and help mitigate dynamic structural problems encountered in typical railroad bridges.

Chapter 1: Introduction and Background

Long-haul passenger, commuter, and freight railroads are essential to maintaining a thriving economy, especially in New England, with its many urban areas, industries, and significant national defense activities (Malla, Baniya, and Jacobs, 2016). Amtrak's Northeast Corridor (NEC) is the busiest passenger rail corridor in the United States (US). In addition, state-owned rail commuter operations provide trains along the entire southern coastline of Connecticut and serve major urban areas such as Hartford and New Haven in Connecticut, Springfield and Boston in Massachusetts, and Providence, Rhode Island. The US Department of Transportation and the Federal Railroad Administration have designated the railroad line from Washington, District of Columbia., to Boston, Massachusetts (Northeast Corridor) as the highest priority area for upgrading railroad infrastructure for high-speed trains. In addition, freight service is a vital economic driver; a single train can carry the freight of several hundred trucks, reducing highway gridlock, the cost of maintaining existing highways, and the need to build expensive new ones (Malla et al., 2017).

Since most New England long-span railroad bridges are old, they often show unusual behavior under typical service loads (Jacobs, Dhakal, and Malla, 2021). This report presents a basic methodology to understand and evaluate the dynamic behavior of century-old railroad bridges using twenty-first century technology such as detailed laboratory material testing, field test measurement devices, and computation modeling. Figure 1 shows different types of long-span open-deck railroad bridges.

The secondary goal of this research is to understand the effectiveness of different types of sensors in measuring the railroad bridge's structural response. In the design of passenger railway bridges, for instance, serviceability often governs the design, which is vital to maintain restrict the displacements and accelerations of the bridges and track to small values under typical vehicle loads (AREMA, 2017; CRF, 2022). Therefore, a measurement sensor that provides acceptable accuracy at lower cost is essential.

(a) (b)

Figure 1: Old railroad bridges: (a) Devon Bridge, Milford/Stratford, CT, (b) Frankenstein Trestle, White Mountains, NH.

1.1 Project Motivation

Many of New England's highly active railroad bridges were built over 100 years ago. Countless variables affect the current dynamic response of those bridges, for example, the bridge structure type, corrosion condition, and loading history. Therefore, there is a critical need for an easy-to-use, efficient, and accurate structural health monitoring system (SHMS). Current SHMS approaches involve the application of many sensors and require extensive analytical post-processing to obtain the bridge's dynamic responses and characteristics (Wenzel, 2009). Accurate results would require days of testing, as well as analysis of all types of loadings the bridge may experience. Ideally, the bridge's displacements and stresses should be evaluated continuously to improve the structural health results. The changes in displacement, stress or natural frequencies for the same loading patterns may indicate a global or localized issue. In addition, the current SHMS requires recording data from different points on the bridge using different sensor types, which entails collecting large amounts of data and increases the time required to process the data. Therefore, there is a critical need to develop and investigate an alternative approach to evaluating the overall condition of the bridge (AAR, 1968) using a limited number of sensors. This report presents a methodology for evaluating the bridge's response and characteristics using field test data collected by means of different sensors under service conditions and laboratory material testing.

1.2 Project Goal, Objectives, and Tasks

The primary goal of this research project is to develop and implement an efficient and effective methodology for short- and long-term continuous condition monitoring and detection of railroad bridges, using analytical and computational (finite element) modeling/analysis and field-testing of bridges under moving train loads, enhanced with material testing. Primary specific objectives include:

1. Evaluate the current stress-strain condition of the material from the old existing New England railroad bridges.
2. Develop the Finite Element (FE) models of old railroad bridges and validate the model using the field-obtained data using different commercially available sensors.
3. Understand the effects of vehicle type and bridge interaction on the structural response and characteristics for safety and durability, especially the effects of different train compositions on the response of older bridges.

The following Tasks have been conducted to achieve the overall project objectives:

Task 1: Collect and analyze existing railroad bridge structure data, including an inventory of bridge numbers, types, ages, locations, and inspection frequency in the New England region from state Departments of Transportation (DOTs) and railroad companies. Select potential bridges for a detailed dynamic field study.

Task 2: Collect sample material specimens from select railroad bridges and conduct laboratory tests per ASTM standards to determine stress-strain behavior. Analyze the effect of aging on stress-strain behavior.

Task 3: Develop a FE model of selected bridges to determine their response accurately and compare the frequency, mode shapes, and deformation results with experimental field data.

Task 4: From the analytical and FE model analysis, number/types and locations of sensor for effective bridge condition monitoring. Develop a suitable methodology for railroad bridge monitoring and postprocessing technique.

Task 5: Determine from the analytical and FE analysis effects of different axle configurations of typical service trains on the resulting bridge response.

1.3 Report Overview

This report is aligned with TIDC Project # 1.2: "Condition/Health Monitoring of Railroad Bridges for Structural Safety, Integrity, and Durability," where material testing, numerical modeling, and field testing were employed to characterize the dynamic response of old railroad bridges.

This report focuses on the dynamic study and structural integrity of steel truss railroad bridges using field test data, a computational model, and material testing. First, the report presents basic concepts from the theory of structural response under dynamic/ moving loads, as well as the elements of field-testing equipment theory, in order to familiarize the reader with the fundamentals of Structural Health Monitoring (SHM). Second, the field test procedures and methodology, data processing techniques, and material testing protocols are presented. Finally, computational modeling of the selected bridges is discussed in detail, and the results of the finite element (FE) simulations are compared with the theoretical predictions and field test data.

Chapter 2: Methodology

In terms of structural dynamic behavior, railroad bridges differ significantly from highway bridges. A train is usually a sequence of identical vehicles in connection, plus one or two locomotives, and usually generates a repetitive response over a railroad bridge (Yang, Yau, and Wu, 2004). On the other hand, the vehicles moving over a highway bridge are random; they may vary in axle weight, axle interval, and speed of movement.

This report is centered on the dynamic responses of old railroad bridges under a typical service train, although some of the methods discussed in this report can also be applied to highway bridges, for example the field test and data processing methodology.

The interaction between a bridge and the vehicles moving over it is most accurately modeled as a coupled, nonlinear dynamic problem (Chopra, 2017). However, structural engineers are often interested only in the bridge response; therefore, the moving vehicles, ideally represented as a sprung mass model, have frequently been approximated as a sequence of moving forces traveling at constant speed. The interaction vehicle-bridge system is determined primarily by the structures' natural frequencies and the operation frequency of the moving vehicles due to the velocity and axle composition (Yang et al., 2019).

In design practice, the dynamic response of bridges is evaluated by multiplying the forces and stresses caused by the static live loads and by use of the impact factor, defined as the ratio of the maximum dynamic to the complete static response of the bridge under the same load minus one (Yoon et al., 2013). For example, the current design practice (AREMA, 2022) considers the variation of the impact load directly related to the span length of the bridge, ignoring the stiffness and mass. This approach, although proven valid, under-estimates the bridge conditions and is not suitable for moderate- and high-speed trains, typified by passenger trains.

It is believed that the methodologies presented herein can be applied to better understand the bridge-related dynamic structural problems encountered in traditional railroads and mass rapid transit systems. For example, the design of high-speed railway bridges is generally governed by serviceability conditions rather than strength and yielding. As a result, the resonance phenomenon will occur on the bridge if the moving train axle frequency coincides with the bridge's natural frequency; in this case, the response will be continuously magnified as more railroad cars pass the bridge (Hilal and Zibdeh, 1999).

2.1 Basic Theory on Dynamic Response of Bridges due to Moving Vehicles

Research on the dynamic response of bridges caused by vehicular movement dates back to the mid-nineteenth century, following the collapse of the Chaster Rail Bridge in England in 1847 (Bajer and Djniewicz, 2012). This section starts with a description of the concept and effect of a single axle load under different parameters, such as traveling speed, bridge stiffness, and vehicle axle characteristics. Finally, the concept of multi-axle typical of train composition is discussed.

The moving constant force model (Figure 2-a) is the simplest model that can be created, and structural engineers have frequently adopted this model in studying vehicle-induced bridge

vibrations. The effect of two-way interaction between the bridge and the moving vehicle is ignored. For this reason, the moving load model is suitable for the case where the vehicle's mass is small relative to the bridge and only when the vehicle response is not of interest (Biggs, 1964).

A rolling mass model should be adopted for cases where the vehicle's inertia cannot be considered negligible (Figure 2-b). One drawback of the moving mass model is that it excludes consideration of the bouncing action of the moving mass relative to the bridge. Such an effect is expected to be significant when there are rail irregularities, pavement roughness, or when vehicles are moving at relatively high speeds (Frýba, 2000).

The vehicle model can be further enhanced through consideration of the elastic and damping effects of the suspension systems. The simplest model, in this case, is a moving mass supported by a spring-damped unit, the so-called sprung mass model (Figure 2-c). Biggs (1964) presented a semi-analytical solution to the problem of a simple beam traversed by a sprung mass, and this solution has been by the researchers to generate an in-house FE model code that meet the research goal.

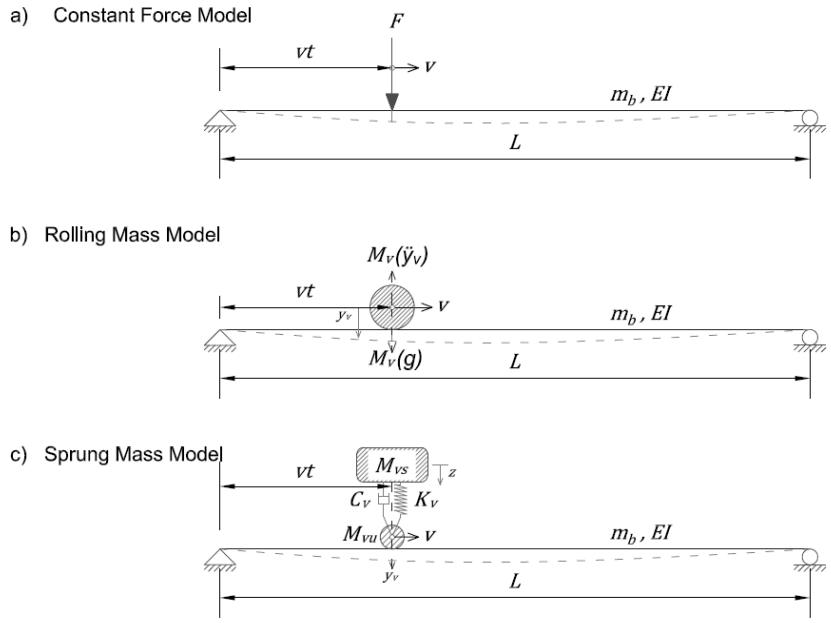

Figure 2: Simply supported beam under moving vehicle models

Biggs (1964) has developed a method to determine the simply supported beam response under the effect of a moving vehicle. It was found that the operation frequency (Ω_n) is the critical factor in analyzing the bridge resonance and can be found using the equation below in rad/sec (Biggs, 1964):

$$\boldsymbol{\Omega_n} = \frac{\boldsymbol{n\pi v}}{\boldsymbol{L}} \quad (1)$$

Where:

Ω_n is the operation frequency in rad/sec

v is the vehicle traveling speed in ft/sec

L is the span length in feet

n is the frequency integer multiplicator of the frequency

Similarly, the beam natural frequency (ω_n) can be determined using the equation below in rad/sec:

$$\boldsymbol{\omega_n = n^2 \frac{\pi^2}{L^2} \sqrt{\frac{EI}{m_b}}} \quad (2)$$

Where:
ω_n is the beam natural frequency in rad/sec
E is the modulus of Elasticity in ksi
I is the beam moment of inertia in in.^{4}
m_b is the beam linear mass in lb-sec^2/in.^{2}

Resonance occurs when the forcing frequency equals the system's natural circular frequency (Tedesco, McDougal, and Ross, 1999). The resonance at first mode can be found by combining Equations 1 and 2 ($\omega_1 = \Omega_1$), and the critical traveling velocity (v_{cr}) for the bridge can be found using Equation 3. This critical velocity often governs resonance for bridges with span lengths less than the typical car length, usually found on the short-span bridges (Yang, Yau, and Wu, 2004).

$$\boldsymbol{v_{cr} = \frac{\pi}{L} \sqrt{\frac{EI}{m_b}}} \quad (3)$$

Bridge design codes, such as AREMA, account for the Dynamic Magnification Factor (DMF) and other factors such as impact loads and is only account for the bridge type the span length (AREMA, 2022). The DMF is the ratio of dynamic displacement, $Y_c(t)$, to the static displacement, Y_{static}. The static mid-span displacement can be found using the equation below.

$$\boldsymbol{Y_{static} = \frac{P}{K} = \frac{2P}{m_b L \omega_1{}^2} \approx \frac{PL^3}{48EI}} \quad (4)$$

Where:
P is the mid-span point load in lb
K is the beam mid-span equivalent stiffness ksi
ω_1 is the beam first bending natural frequency in rad/sec.

The bridge's dynamic response can be affected by different factors such as the axle load to bridge weight ratio, and ratio of vehicle stiffness to beam stiffness at mid-span. The axle load and the vehicle stiffness are directly related to vehicle characteristics, and the approximated bridge weight is given by multiplying the line mass (m_b) with the span length and the gravity, as shown in the equation below.

$$\boldsymbol{W_b = m_b L g} \quad (5)$$

Where:
g is the acceleration due to gravity (32.17 ft/s^2)

The research team have used the in-house FE code using the central difference method (Tedesco, McDougal, and Ross, 1999) to solve Bigg's simplified sprung mass model under a single load over

a supported span. The result is better represented in dimensionless units and ratios. Therefore, the approximated bridge weight, axle ratio, and ratio of vehicle stiffness to beam stiffness at mid-span were used to generate theoretical bridge midspan vertical displacement response and were compared with available references (Bajer and Dyniewicz, 2012).

The bridge stiffness with the load at the mid-point (K_b) is given by the equation below:

$$K_b = \frac{m_b L \omega_1{}^2}{2} \tag{6}$$

Figure 3 shows the DMF at the bridge mid-point under the different rates of critical velocity, weight ratio, and stiffness ratio. The models use 75% of the total axle load as the sprung mass and the remaining 25% as the unsprung mass. The plotted result has shown an agreement with the Bajer-Dyniewicz models (Bajer and Dyniewicz, 2012) and has shown that velocity ratio is the main factor influencing the DMF.

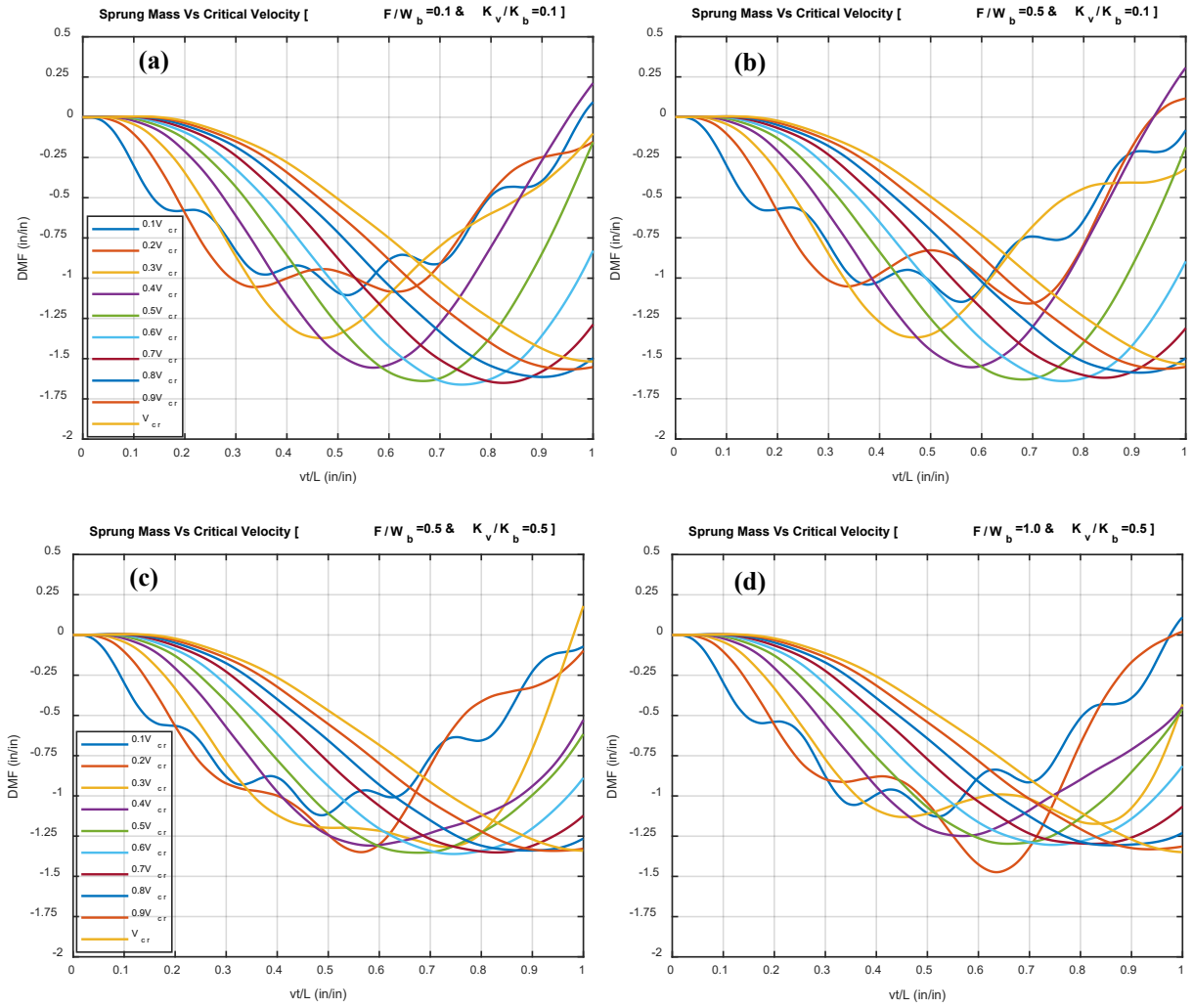

Figure 3: Dynamic Magnification Factor from the beam mid-point under different rate of critical velocity, ratio of axle load to beam weight, and vehicle stiffness over bridge stiffness

From the plots in Figure 3, it is possible to see that the maximum DMF will occur when the train travels at 50-60% of the critical velocity for the bridge. For example, Figure 3 (a) shows an effect of the critical vehicle traveling speed: the axle load is ten percent of the total bridge weight, and the vehicle stiffness is ten percent of the bridge mid-span stiffness. In reality, the typical train axle load-to-bridge weight ratio is less than five percent, and the vehicle stiffness-to-bridge mid-span stiffness ratio can vary with the type of equipment used on the bridge. Therefore, as shown in Figure 3, the DMF can be affected by different factors and must be evaluated for different equipment and bridge types.

On the other hand, the resonance for bridges with span lengths higher than the car length, i.e., long-span bridges, is governed by the axle frequency (f_{An}) (Yang, Yau, and Wu, 2004; Frýba, 2000); this frequency is due to the axle spacing and the vehicle traveling speed. The type of equipment and the velocity will dictate the response. Any vehicle acceleration or deceleration can cause resonance for a few seconds and usually does not significantly affect the structural dynamic response of the bridge (Yang, Yau, and Wu, 2004).

A train system can be represented as a finite sequence of equal loads with uniform intervals (d), at constant traveling speed (v). Bolotin (1964) has studied train system problems and has identified the period (d/v) as a main essential parameter (Bolotin, 1964) for the forcing frequency of long span beams. Furthermore, Frýba (2000) concluded that the steady state forced vibration response would attain its maximum when the time intervals between two successive moving loads are equal to some natural periods of vibration of the beam or to an integer multiple thereof (Frýba, 2000), indicating the occurrence of resonance. Equation 7 and Figure 4 can be used to calculate axle period (T_d) knowing the typical car length (d) and the average vehicle traveling speed (v); the frequency can be found by inverting axle period.

$$\boldsymbol{nT_d = \frac{d}{v} = \frac{1}{nf_d}} \tag{7}$$

Where:

f_d is the axle frequency

n is the integer multiplicator of the frequency.

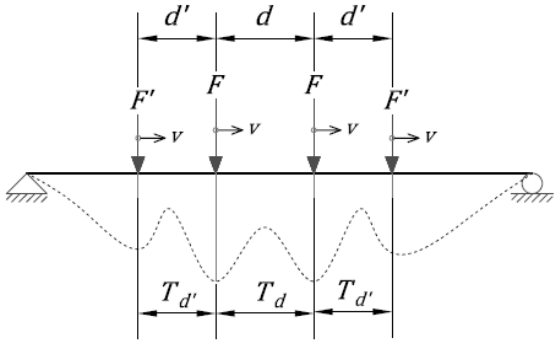

Figure 4: Typical axle period model

2.2 Bridge Structures Investigated

Two railroad bridges were selected for the study. The first is the Devon bridge, located over the lower Housatonic River between Milford and Stratford, Connecticut. The second is the Cos Cob bridge, located over the Mianus river in Greenwich, Connecticut. The bridge selection was based on the following criteria:

1. Structure type: The steel trusses and open-deck structures were used since they facilitate 3D modeling using homogenous material.
2. Built before the 1930s: The ideal bridge should be at least 90 years old, and the build using ASTM A7 steel was discontinued in 1965 (ASTM, 1939).
3. Long-span bridge: A bridge with a span of at least 70 feet was desired. The long-span bridges experience different types of service frequencies, such as the operation and the axle, and tend to produce higher dynamic responses than short-span bridges.
4. Train type: It is desired to focus the study on the NEC passenger trains.
5. Location: The ideal bridge would not be very far from Storrs, Connecticut, where the equipment would be stored, facilitating commuting.

The picture below shows the two selected bridges and the studied spans under typical service. The left side of the figure shows the Devon bridge south bridge span seven, and the right side shows the Cos Cob bridge with the Metro-North M8 train.

Figure 5: (a) Devon bridge span 7 from the south bridge, (b) Cos Cob bridge span 3 from north bridge

2.2.1 Devon Bridge

Devon bridge is located over the lower Housatonic River between Milford and Stratford, Connecticut. This long-span open-deck bridge was built in 1906 by the American Bridge Company and is owned by the Connecticut Department of Transportation (CONN DOT). It combines a deck girder, Baltimore trusses, and Scherzer rolling lift bascule. It comprises six simply-supported sections resting over six stone abutments and piers. Two sections are deck girder, four spans are in Baltimore trusses, and one is a rolling lift bascule. The Devon bridge uses riveted connected members made of historical bridge structural ASTM A7 steel. This project includes a section spanning 217’-7" (66.32 m) between the center lines of the piers and the east abutment. Figure 6 shows the schematic of the total bridge length.

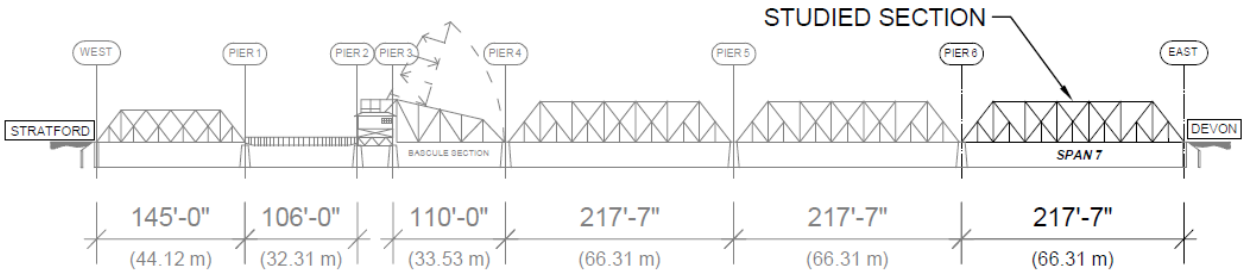

Figure 6: Devon bridge elevation scheme

2.2.2 Cos Cob Bridge

Cos Cob bridge is located over the Mianus river in Greenwich, Connecticut. The long-span open-deck bridge, built in 1904 by the American Bridge Company and owned by CONN DOT, is a combination of deck girder, deck trusses and rolling lift bascule. It is made of eleven simply supported sections resting over eleven stone piers and abutments; three of those sections are deck girder, seven deck trusses and one rolling lift bascule. Like Devon Bridge, the deck girder and trusses are made of ASTM A7 steel and are riveted. The superstructure consists of a built-up section using rivets forming I-shape and C-shape and is found in the trusses and girder sections; the bracing system is made of hot rolled steel angles with gusset plates riveted to the superstructure. For this study, the deck truss between piers 3 and 4 as shown in Figure 7**.** This is because of the following reasons:

1. This span is easily accessible through a small route which helped the research team to carry all the field-testing equipment. The large space on the front view side of the bridge (as shown in Figure 7) helped to set up the LDV while measuring the lateral response.
2. There is a small area of land under the span where the water level goes down in the morning (affected by the tides). This land helped the research team to install the Laser Doppler Vibrometer during vertical reading. Most of the other spans are directly over the water or are not easily accessible or are surrounded by the bushes.

The section has 122’-10” (37.44 m) of length between centerline of piers. There is no previous monitoring experience in the Cos Cob Bridge.

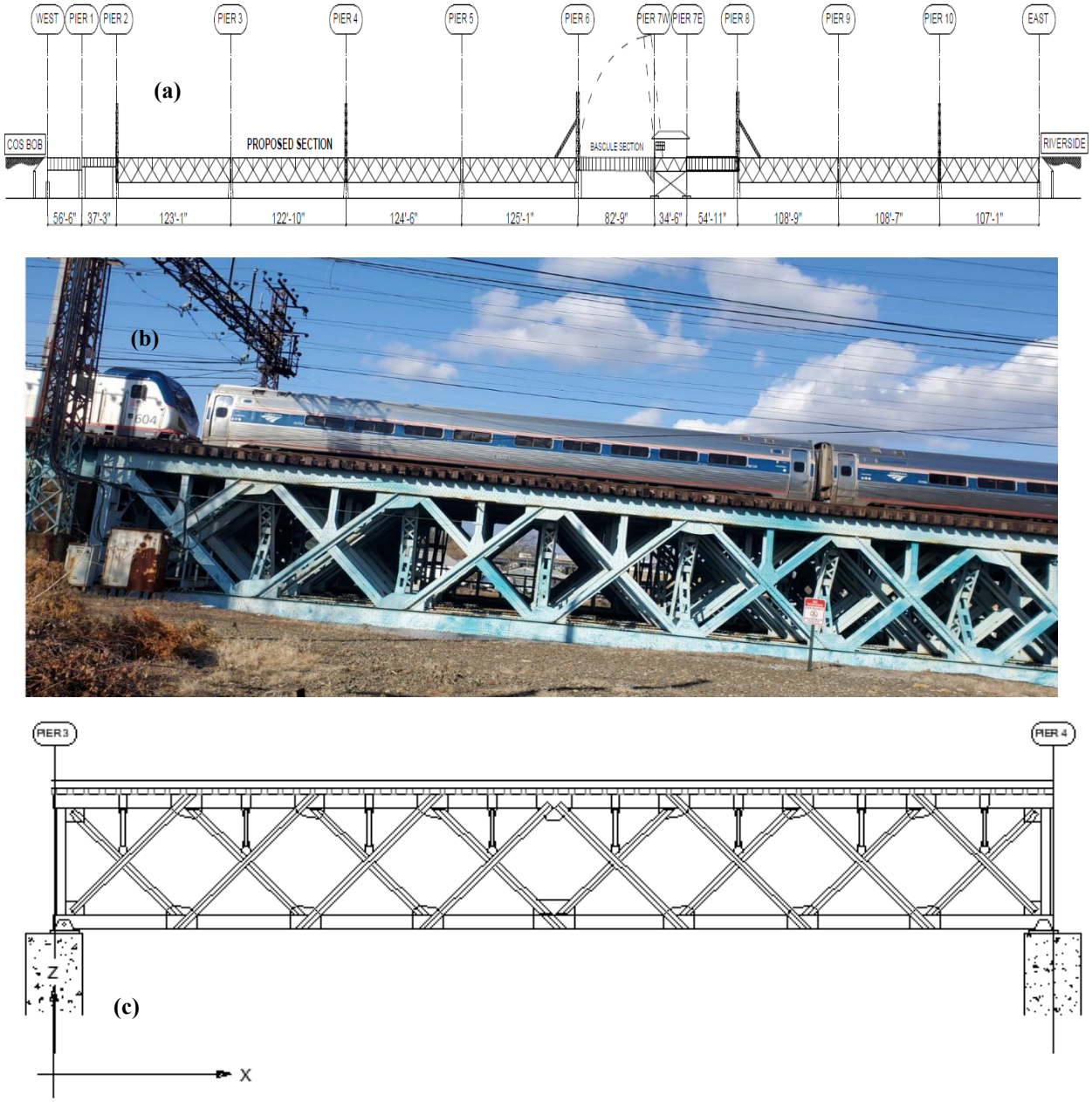

Figure 7: Cos Cob bridge: (a) elevation scheme, (b) picture with Amtrak Regional train, and (c) elevation of the studied span.

2.2.3 Other Bridges

Apart from the Devon and the Cos Cob bridges, the research team collected the material samples from other two bridges: the Atlantic Street Bridge located in Stamford, CT and the Aroostook River Bridge located in Aroostook, Maine for the tensile testing. Aroostook Bridge was built in 1952 and is still in operation while the Atlantic Street Bridge was demolished.

2.3 Laboratory Material Testing

Many of the active railroad bridges in New England were built over 80 years ago and are constructed with A7 steel, which is no longer in use. It is critical to study the mechanical properties of this outdated material for bridge durability and passenger safety. Tensile tests were performed on the bridge material collected from the bridges described in section 2.2. Information regarding material collection, sample preparation, testing methodology and equipment used in testing is presented in the following sub-sections. Results are presented in Chapter 3.

2.3.1 Bridge Material Collection

The materials collected are from footbridge bracing members from the Cos Cob bridge in Greenwich, CT, stringer angles from the Devon bridge in Stratford, CT, web materials from stringers, girders, and floor beams from the Atlantic Street bridge in Stamford, CT, and the bottom cover plates on the deck plate girder approach span on the Aroostook River bridge in Aroostook, ME. These opportunities were provided by Connecticut DOT, Metro-North Railroad Co., the construction company ATANE and Maine DOT, respectively. Highly corroded and damaged members that can be visually observed were discarded during material collection.

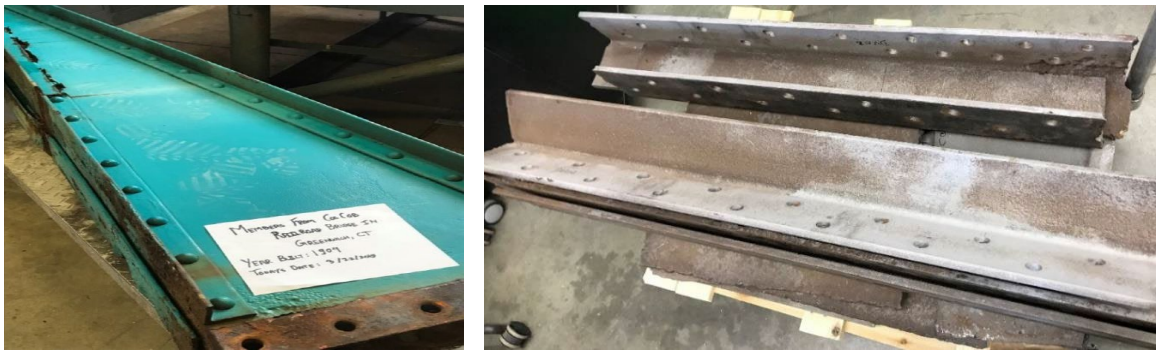

Figure 8: Cos Cob bridge raw material with lead paint (left), Devon bridge sandblasted raw material (right)

Figure 9: Girder material (left) and stringer material obtained from Atlantic Street Bridge, CT.

Figure 10: Fixturing of angle beams for coupon cutting

2.3.2 Specimen Preparation and Testing Methodology

Most of the railroad bridges built before 1980 will have lead paint on them. The lead paint abatement must be performed by Environmental Protection Agency (EPA), Occupational Safety and Health Administration (OSHA), and State Public Health (SPH) certified companies in the case of public university research. The EPA, OSHA, SPS certified, and Husky-Buy approved vendor AAIS Corporation of West Haven, CT performed lead paint abatement of this material. AAIS used a sandblasting process to successfully remove all the paint. The lead painted materials and the sand blasted materials are presented in Figure 8.

Dog-bone shaped specimens were prepared in accordance with the ASTM E8-16 specification. Figure 11 and Table 1 provide the specimen geometry and dimensions. To minimize thermally-induced microstructure changes on the coupons, the cutting process was limited to waterjet and milling using Computer Numerical Control (CNC) machines. Afterwards, the coupons were visually inspected for visible cracks.

Table 1: Sample coupon geometry

	Inches	mm
A	3.230	82.04
B	2.300	58.42
C	0.750	19.05
W	0.500	12.70
T	0.290	7.37
R	0.125	3.18
L	8.100	205.74

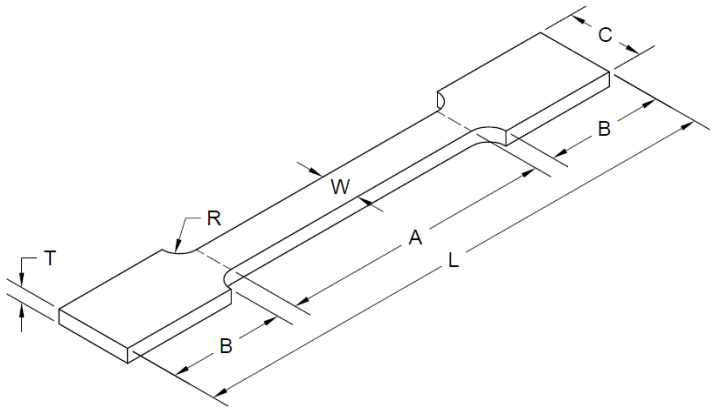

Figure 11: Sample coupon geometry

Coupon procurement and testing has been performed in accordance with ASTM E8 “Standard Test Methods for Tension Testing of Metallic Materials”. Dimensions for the coupons are all per the ASTM requirements. Loading on the specimen is controlled by the cross-head displacement of the machine defined as extension rates in this study. Per ASTM E8, there is a provision for different speeds for determining the yield properties (0.015 +/- 0.003 in./in./min [mm/mm/min] of the reduced parallel section); and the tensile strength (0.05 and 0.5 in./in./min [mm/mm/min] of the reduced parallel section). However, due to machine limitation, the yield strength and the tensile strength are determined at the same extension rate (monotonic loading to failure) for this study. Extension rates of 1 mm/min [0.039 in/min], 4 mm/min [0.157 in/min], 8 mm/min [0.315 in/min], 100 mm/min [3.937 in/min] and 500 mm/min [19.69 in/min]) are used to understand the effect of extension rate on the yield stress, ultimate tensile stress and breaking point stress in the case of the Aroostook Bridge material specimen, but for other bridge material specimens, a extension rate of 4 mm/min [0.157 in/min] is used. These extension rates are equivalent to strain rates of 0.012

mm/mm/min, 0.048 mm/mm/min, 0.097 mm/mm/min, 1.2 mm/mm/min and 6.06 mm/mm/min respectively of the length of the reduced parallel section.

2.3.3 Material Test Equipment

A 50 kN capacity Instron 5900R model tensile testing machine was used with an electronic dial indicator (Logic Illuminate) manufactured by Chicago Dial Indicator and the measurements for the force axis were collected using a Bluehill Universal material testing software and those for the displacement axis were collected using electronic measuring system-an application provided by the Chicago Dial Indicator.

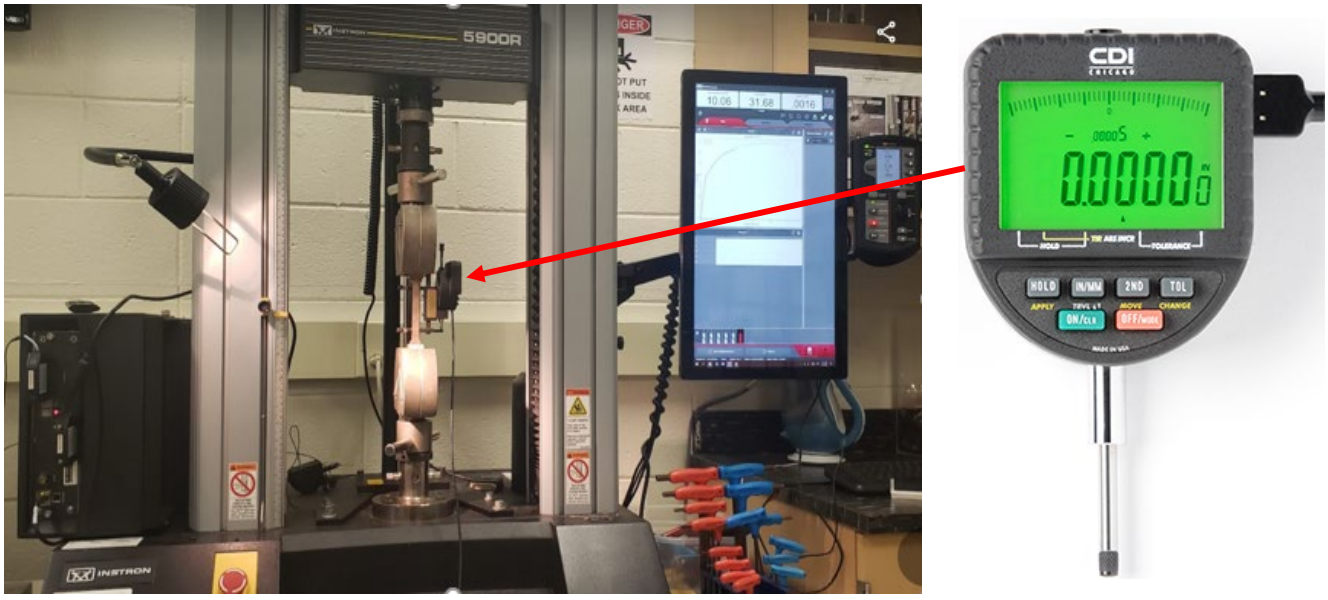

Figure 12: 50 kN rated Instron Test Set with an electronic dial indicator

2.4 Field Testing

Three main sets of field tests have been conducted on the selected bridges. The first field test was conducted on the Devon bridge using a 3D Compact Scanning Vibrometer and a bridge shaker, and limited data were collected and analyzed to obtain results due to the low vibration signal emitted by the shaker. The second set of tests was conducted on both the Devon and Cos Cob bridges using a Micro Electro Machined Sensor to measure the service acceleration during the passage of the trains. However, due to the poor accelerometer resolution, as shown in Figure 13, the results have little applicability for detailed research. The final set of field tests used a Single-point Laser Doppler Vibrometer (LDV) to record the velocity response during the train operation on both selected bridges. The table below shows a summary of the field tests.

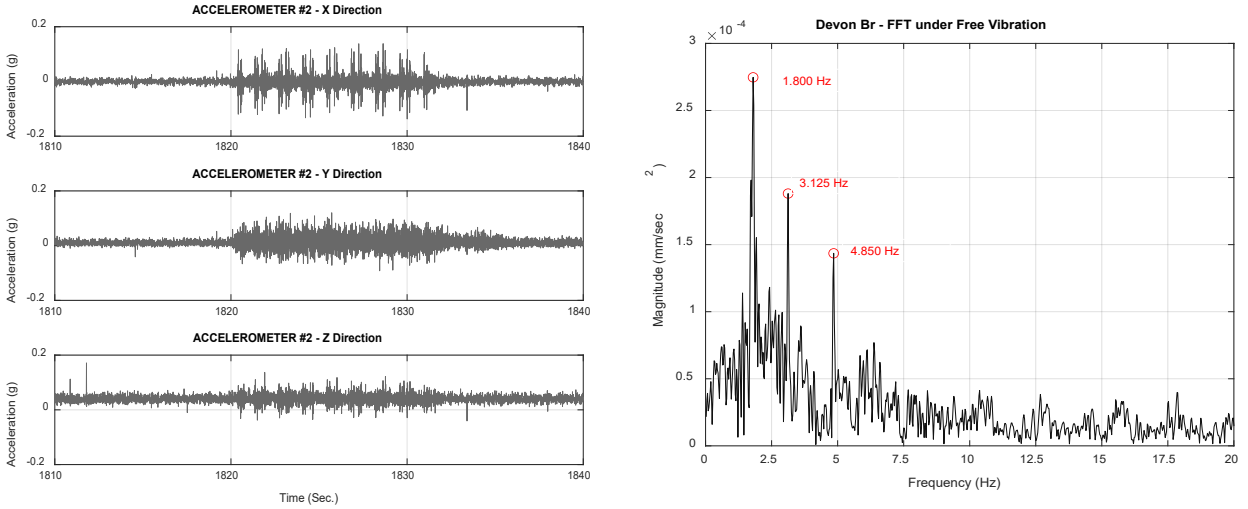

Figure 13: Devon bridge: (a) Acceleration time-domain Accela train heading west-east on track 4 (January 23, 2021), (b) South trusses frequency-domain under ambient vibration (October 28, 2020)

This report only focuses on the third field test set since those results have shown good response quality and consistency.

Table 2: Field Tests conducted on the selected bridges

Test #	Location	Date	Data Collected
1	Devon Bridge	October 28, 2020	Velocity response, Natural Frequency, Freight train, 3D laser scan
2	Cos Cob Bridge	January 20, 2021	Acceleration response, passenger train
3	Devon Bridge	January 23, 2021	Acceleration response, passenger train
4	Cos Cob Bridge	June 6, 2021	Horizontal velocity response, displacement time domain, Single-point laser
5	Cos Cob Bridge	June 7, 2021	Vertical velocity response, displacement time domain, Single-point laser
6	Devon Bridge	June 8, 2021	Vertical velocity response, displacement time domain, Single-point laser

The work procedure was divided into three main phases: preparation, data collection, and data processing. The Preparation phase started with the preliminary study, obtaining the required permits and training, and calibration of the different measurement equipment. The second phase was data collection, which was the most critical. Most of the activities were performed in the field; correct planning and weather monitoring dictated the success of this phase, and the safety requirements were always strictly followed during this phase. The Data processing phase was the

last phase of the work procedure. In this phase, the results were processed and interpreted (Reiterer et al., 2018).

Preparation Phase: During this phase, all technical aspects of the bridges were studied based on the available documents about the selected structures. In addition, safety requirements such as Railway safety training and protective liability insurance policy was finalized during the preparation phase. Initial contact with the CONNDOT and MTNR included the detailed preliminary work procedure.

Data Collection Phase: This phase represented the critical phase of the project. Once the data are collected, a few arrangements or corrections can be made to this data. Since most of the work was performed on the operational bridge with moving trains and other associated hazards, safety procedures were strictly followed. In addition, the work procedure was planned to avoid bad weather and to allow sufficient time to request the railway company personnel, such as flaggers, and safety officers, if required.

Data Processing Phase: This phase represented the last phase of the monitoring campaign. During the data processing phase, raw data were processed and interpreted. This phase was performed in the office using computer software such as Excel and MATLAB, and the results have been presented in this final report.

Due to moving vehicles (train) and associated possible hazardous situations, the safety procedures were strictly followed, particularly in the data collection phase. The safety requirements in Railway bridges are specified primarily by the Federal Railway Administration (FRA) in the document "The Bridge Safety Standards Compliance Manual," which provides technical guidance to Federal bridge specialists (FRA, 2018). The second essential requirement is from the bridge operator, in this case, Metro-North Railroad, for both bridges. Before applying for the entry permit from Metro-North Railroad, all researchers are required to attend and pass an exam regarding the safety requirements and have the Railroad Protective Liability Insurance Policy. In addition, standard Personal Protective equipment, such as steel toe boots, hard hats, reflective vests, safety glasses, and gloves, was required during this phase.

2.4.1 Field Testing Equipment/Devices

Since poor results were obtained from the first two sets of field tests, the report focuses on the results of only the third set of field tests using the non-contact measurement device, the Polytec VibroFlex Qtec® Single-point Laser Doppler Vibrometer (LDV). For reference and validation purposes, two conventional uniaxial quartz sensing element accelerometers (Piezoelectric) PCB 393B04® were placed on the bridge using magnetic bases and a wired connection to the Data Acquisition (DAQ) system.

An LDV is a scientific non-contact measurement device that uses a laser beam to extract the frequency of vibration from the Doppler shift of the reflected laser beam during the vibration of the surface under observation. The output of an LDV is generally a continuous analog voltage directly proportional to the target velocity component along the direction of the laser beam (Petrescu, 2012).

The Doppler Effect represents the frequency variation of the waves, received by an observer which is drawing (coming), respectively it's removing (going), from a wave spring (source). The different energy states of our reference frame led to differences in measured energy in the wave, called the Doppler shift. This phenomenon was first observed in the mid-1800s in sound waves and later in electromagnetic waves (Petrescu, 2012).

An operational schematic of a typical LDV is shown in Figure 14. First, the laser emits an initial beam with a known frequency(f_o). Second, the beam is divided by half into the reference and the test beam using a light beam splitter. The test beam then passes through a Bragg cell, which adds a frequency shift(f_b). Then this shifted beam is directed to the target. Finally, the Doppler shift is added to the beam during the target's vibration, given by the equation below (Nassif, Gindy, and Davis, 2005).

$$\boldsymbol{f_d = \frac{2v(t)\,cos(\alpha)}{\lambda}} \tag{8}$$

Where:

$v(t)$ is the velocity of the target as function of time

α is the angle between the laser beam and the velocity vector

λ is the medium wavelength.

Portions of the beam are reflected in the LDV and transferred by the beam splitter to the photodetector. Depending on the displacement and the target's velocity, the reflected beam is changed in the frequency of $f_o + f_b + f_d$ and phase angle. The characteristics of the vibration are contained in the reflected beam. It is combined with the reference beam by superposition, creating a modulated output signal revealing the Doppler shift in frequency at the photodetector. Since the photodetector output is a modulated standard frequency, it can be demodulated to derive the velocity time response of the vibrating target using a signal processor (Rossi, Gussella, and Gioffré, 2002).

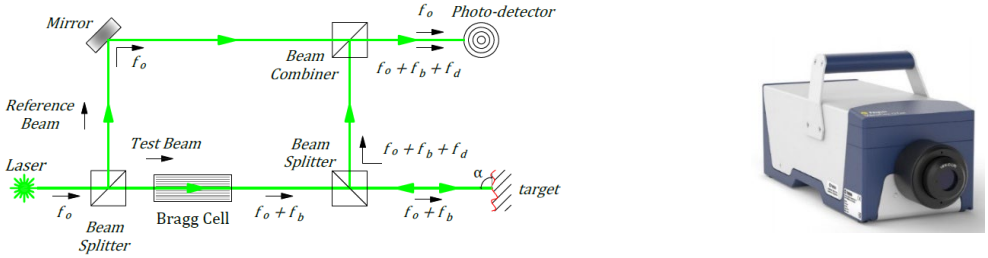

Figure 14: (a) Laser Doppler Vibrometer operation schematic, (b) Polytec single point vibrometer head

This study used the uniaxial quartz sensing element accelerometers manufactured by PCB Piezotronics, model 393B04. These accelerometers use ceramic crystals with a known mass attached to the case as a sensing element. When the measuring system is subjected to vibrations, the accelerometer's internal inertia mass compresses and stretches the piezoelectric crystals. This compression and stretch forces are proportional to the acceleration, following Newton's second law of motion, and produce a small electrical charge, which is demodulated and amplified via a

servo circuit. Finally, the output in Volts is proportional to the acceleration signal (Rossi, Gussella, and Gioffré, 2002; Schiefer, and Dosch, 2012). The figure below shows the principle of the operation of the quartz sensing element accelerometer.

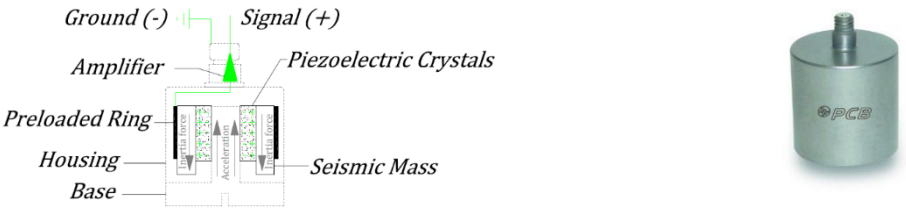

Figure 15: (a) Quartz sensing element accelerometer operation schematic, (b) PCB seismic mass accelerometer

2.4.2 Devon Bridge Field Test

The most crucial field test for the Devon bridge was during the third set of tests. In this field test, bridge responses from service conditions were collected in the time domain, pre-processed, and converted to the frequency domain to extract the dynamic characteristics of the bridge. Vertical velocity and acceleration time variation have been collected from Devon bridge span 7 using LDV and accelerometers, respectively.

Table 3: Recorded data from field tests conducted on Devon bridge (June 8, 2021)

Train #		Direction	Track #	Cars	Train Type	LDV Loc
1		East-West	4	8	MTNR M8	1
2		East-West	1	2	Maintenance	2
3		East-West	4	8	AMTK Regional	2
4		East-West	4	11	MTNR M8	2
5		East-West	4	8	AMTK Acela	3
6		West-East	2	12	Freight	3
7		East-West	3	8	AMTK Regional	3
8		West-East	3	8	AMTK Regional	4
9		West-East	1	8	MTNR M8	4
10		West-East	2	8	MTNR M8	4
11		East-West	4	8	AMTK Regional	5

During a typical day shift, the research team set up the testing equipment, LDV, and accelerometers and collected vertical velocity and acceleration data from 11 trains under typical operation. The most relevant data was the train passing over the south bridge (tracks 2 and 4). Table 3 shows the log of trains crossing the bridge, along with other relevant information. Notice that trains 2, 8, and 9 were recorded when the train passed on the north bridge (tracks 1 and 3); therefore, they will be considered ambient vibrations. The limited data are displayed in Figure 16

the form of a pie chart showing the distribution of various train types. We can conclude that the Metro-North Railroad M8 (MTNR M8) and the Amtrak Regional (AMTK Regional) are typical bridge users. The raw data of velocity, displacement, and acceleration derived from the LDV, and accelerometers are presented in appendix A.

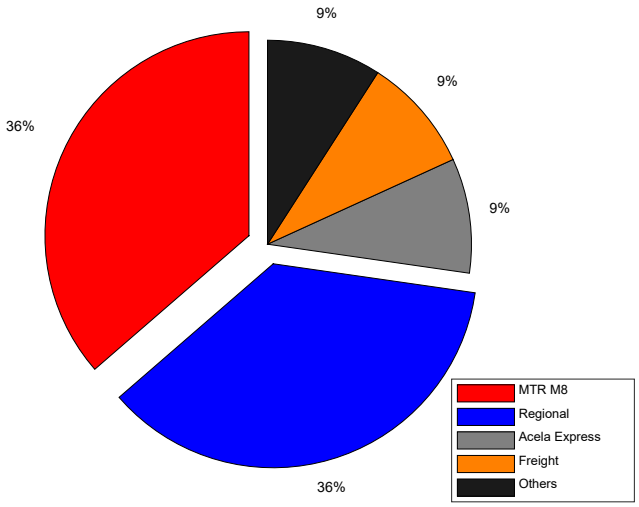

Figure 16: Train type statistics on Devon bridge (June 8, 2021)

The single-point LDV was installed in the vertical position to record the vertical velocity during the service train operations. After successfully recording a train passage over tracks 2 or 4, the LDV was relocated to the next point. Five vibration locations were used to collect the data. LDV 1 and LDV 2 were over the nodes of the south trusses, and LDV 3 to LDV 5 were in the middle of the floor beam.

Uniaxial accelerometers were installed at a fixed point throughout the test. Two accelerometers were used to record the bridge acceleration response. Therefore, ACC 1 was installed to record vertical acceleration, and ACC 2 was installed for horizontal acceleration, which has been used in this report. Figure 17 shows the location of the LDV and accelerometers during the field tests. The plan view is shown in Figure A-1 in appendix A.

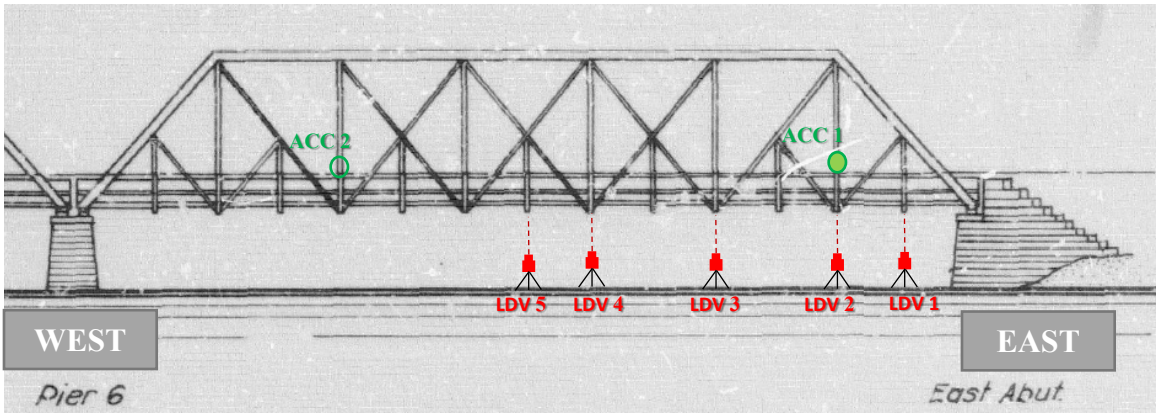

Figure 17: Devon bridge South trusses view with instrumentation location and train number

2.4.3 Cos Cob Bridge Field Test

Field tests were performed under the service loading of Metro North, Amtrak Acela and Amtrak Regional trains passing over the bridge at different speeds using a single-point Laser Doppler Vibrometer (LDV) and accelerometers. Three accelerometers were attached to the bottom chord of the span for the reference as shown in Figures 20 and 22. Reference 2 (Ref 2 in the Figures 20 and 22) was set to collect vertical response and references 1 and 3 (Ref 1 and Ref 3 in the Figures 20 and 22) were set to collect the lateral response of the bridge. The single-point LDV was installed in the vertical and lateral directions to collect the vertical and lateral velocity-time responses respectively during the service train operations. After successfully recording a response from the train passage over the bridge at one node, the position of LDV was switched to record the response from another train on other node. Bridge responses were collected at the nodes presented in Figures 20 and 22 denoted as Vib. Loc 1 – Vib Loc 7 in Figure 20 and Vib. Loc 1 - Vib. Loc 11 in Figure 22. Further details on field testing (train type, direction, number of cars, track number and the nodal position) are tabulated in Tables 4 and 5. Figure 18 shows the experimental setup for the field test of Cos Cob Bridge.

Figure 18: LDV setup to record vertical response, Laser beam pointed to node at the intersection of bottom chord and vertical members (1), Accelerometer attached to bottom chord of Cos Cob Bridge for reference (2)

Table 4: Cos Cob bridge: Field test summary for lateral bridge response (Test Performed: June 6 and 7, 2021)

Train #	Direction	Track #	No. of Cars	Train Type	Vib. Loc
1	E-W	3	-	MTNR M8	5
2	E-W	1	-	MTNR M8	5
3	W-E	4	-	MTNR M8	5
4	W-E	4	-	MTNR M8	5
5	E-W	3	-	MTNR M8	5
6	E-W	3	10	AMTK Regional	7
7	E-W	3	8	MTNR M8	7
8	E-W	1	8	AMTK Regional	7
9	W-E	4	10	AMTK Regional	7
10	E-W	1	8	MTNR M8	6
11	E-W	2	10	MTNR M8	6
12	W-E	4	8	MTNR M8	6
13	W-E	4	10	MTNR M8	4
14	E-W	1	8	MTNR M8	4
15	W-E	4	8	MTNR M8	3
16	W-E	4	8	MTNR M8	2

Note: Number of cars could not be noted for some trains represented as (-)

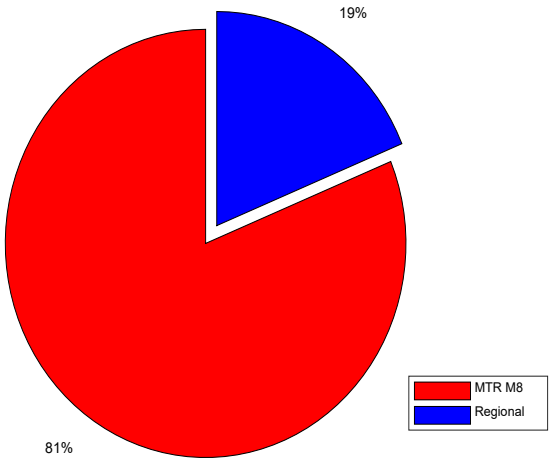

Figure 19: Cos Cob bridge: Distribution of trains for lateral response reading

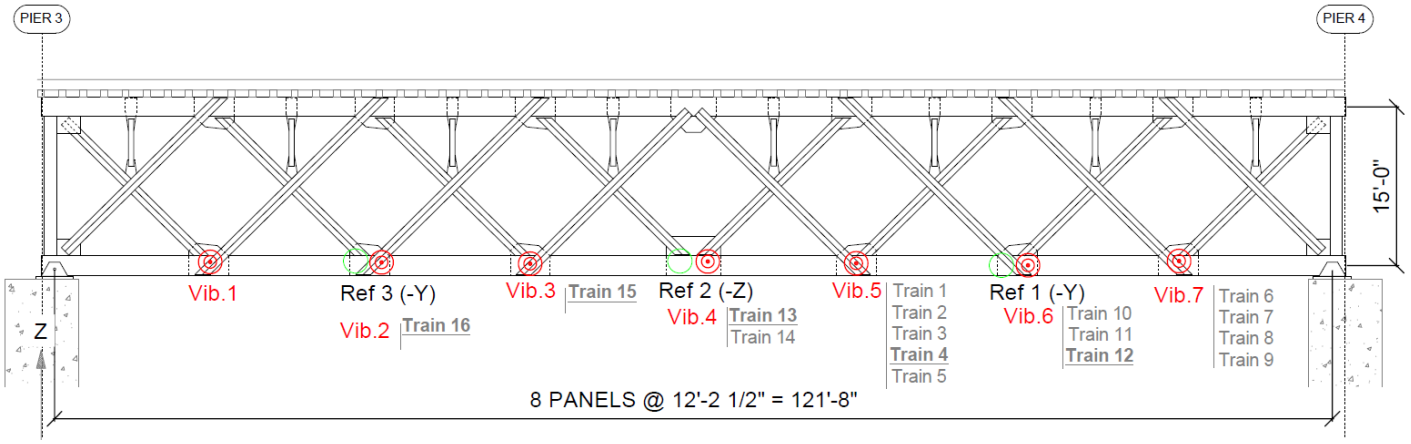

Figure 20: Locations of Sensors for lateral response reading on the Cos Cob bridge, CT

Table 5: Cos Cob: Field test summary for vertical bridge response (Test performed: June 7, 2021)

Train #	Direction	Track #	No. of Cars	Train Type	Vib. Loc
1	W-E	2	-	AMTK Acela	1
2	W-E	4	8	MTNR M8	1
3	W-E	2	-	MTNR M8	2
4	W-E	4	8	MTNR M8	2
5	W-E	4	-	MTNR M8	3
6	W-E	4	-	MTNR M8	3
7	E-W	1	-	MTNR M8	4
8	W-E	4	8	MTNR M8	4
9	W-E	2	8	AMTK Regional	5
10	W-E	4	10	MTNR M8	5
11	E-W	3	8	MTNR M8	6
12	W-E	4	8	MTNR M8	6
13	W-E	4	10	MTNR M8	7
14	W-E	4	8	MTNR M8	8
15	E-W	3	9	MTNR M8	8
16	E-W	3	10	MTNR M8	9
17	-	3	-	AMTK Regional	9
18	-	4	-	MTNR M8	9
19	W-E	2	8	AMTK Regional	10
20	E-W	3	9	MTNR M8	11
21	W-E	4	8	MTNR M8	11
22	W-E	4	10	MTNR M8	12

Note: Number of cars and direction could not be noted for some trains represented as (-)

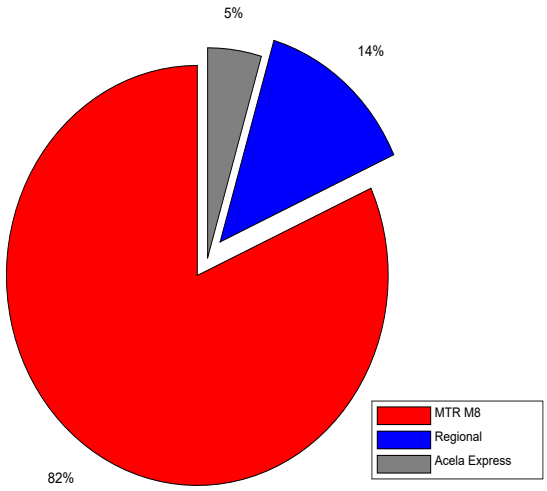

Figure 21: Cos Cob bridge: Distribution of trains for vertical response reading

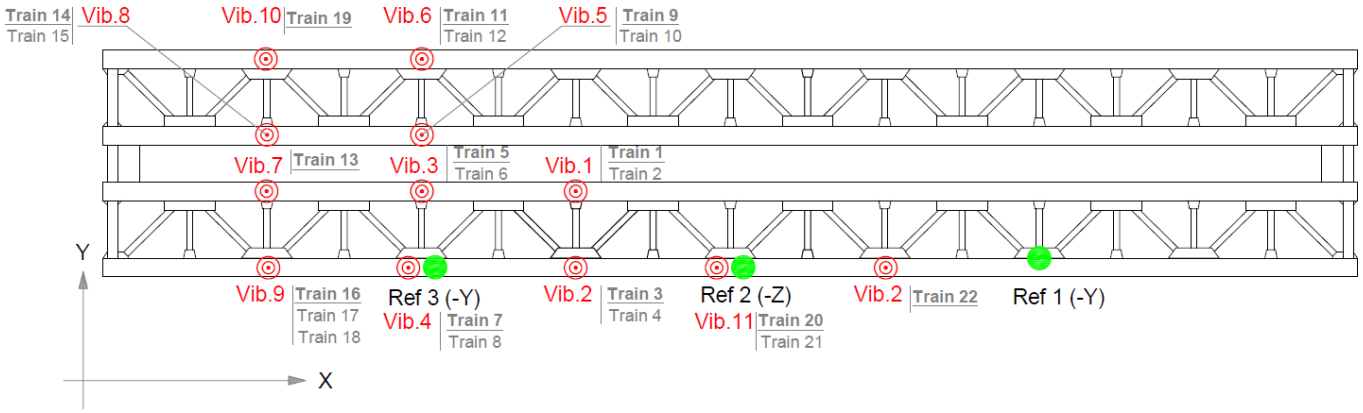

Figure 22: Locations of sensors (Vib. 1 through Vib. 11 for LDV and Ref 1, Ref 2 and Ref 3 for accelerometers) for vertical response reading on the Cos Cob bridge, CT

2.4.4 Representative Field Test Data

The complete filed test data collected from both Devon bridge and Cos Cob bridge using LDV and accelerometers are presented in the Appendix section. The apendix A present the the data coillected from Devon bridge and the apendix B present the data collected from Cos Cob bridge.

For illustration purpose, representative sample field test data from Cos Cob bridge are presented below. Figures 23 and 26 show the typical velocity – time response recorded by the Laser Doppler Vibrometer (LDV) and Figures 24 and 25 show the typical acceleration-time signal recorded by the accelerometer. The data shows both the high-amplitude forced vibration response under the influence of the moving train crossing the bridge and the low-amplitude free vibration response after the train passes over the bridge as shown in Figure 26. The nodes (denoted as Vib. Loc 1 and Vib Loc 4) where data are recorded are presented in Figure 20.

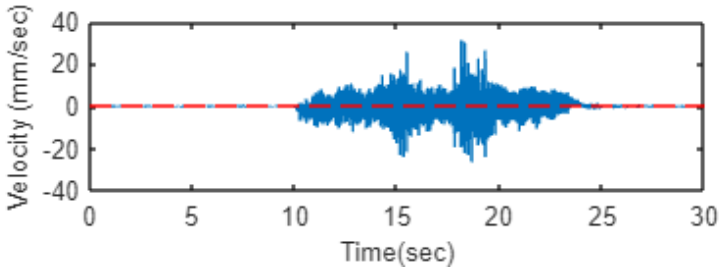

Figure 23: Vertical velocity-time response at Vib. Loc 1 under/subjected to 8-car Metro North train moving at 37.87 mph from New York to New Haven on track 4 of Cos Cob bridge, CT

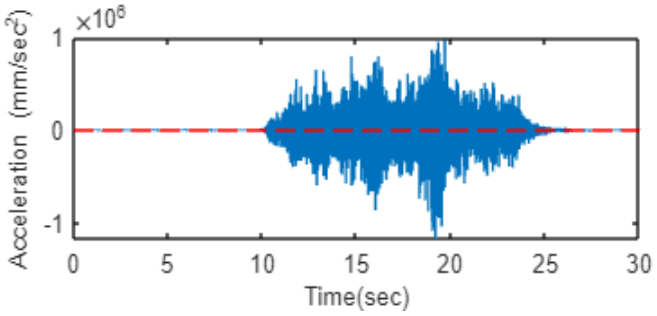

Figure 24: Vertical acceleration-time response at Vib. Loc 1 under/subjected to 8-car Metro North train moving at 37.87 mph from New York to New Haven on track 4 of Cos Cob bridge, CT

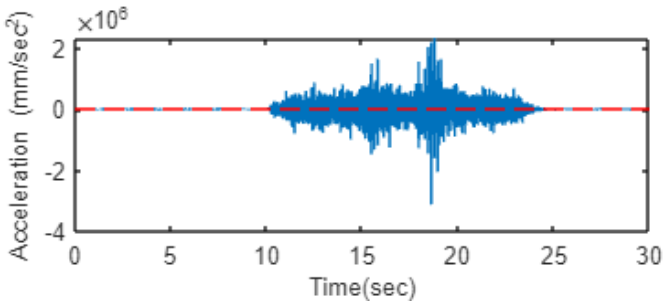

Figure 25: Lateral acceleration-time response at Vib. Loc 1 under/subjected to 8-car Metro North train moving at 37.87 mph from New York to New Haven on track 4 of Cos Cob bridge, CT

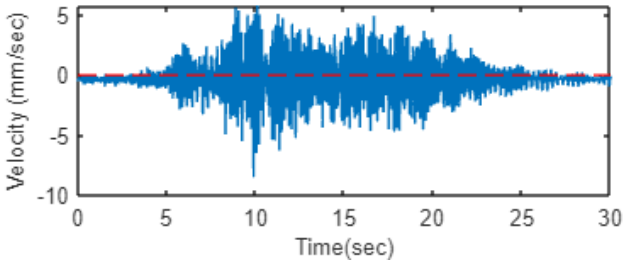

Figure 26: Lateral velocity-time response at Vib. Loc 4 under/subjected to 10-car Metro North train moving at 21 mph from New York to New Haven on track 4 of Cos Cob bridge, CT

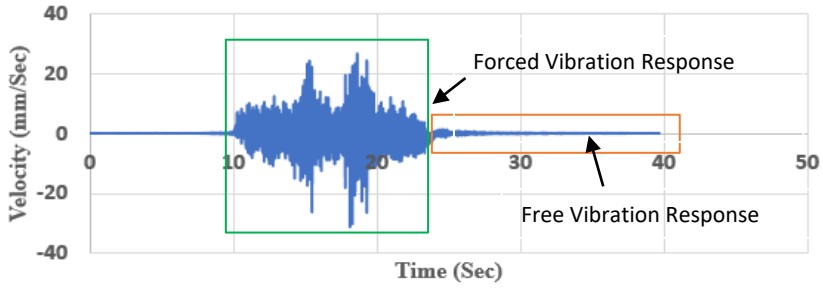

Figure 27: Cos Cob bridge: Typical bridge response showing forced and free vibration

2.4.5 Data Processing in Time-domain

All the data has been collected in the time domain at a sample rate (f_S) of 512 Hz. The output data from the instruments in Volts (V) is assumed to be a linear function of the velocity or acceleration from the LDV and accelerometers, respectively (Schiefer and Dosch, 2012; Polytec,

2015). To obtain the desired values, pre-processing is necessary. Those operations include scaling and centering, to convert the V to desired response and remove the DC bias, respectively (Bro and Age, 2003). The DC bias is undesired offset of the data mean from zero, and is often encountered in LDV data (Polytec, 2015).

Since the service train presents a periodic behavior, the test can be represented and analyzed as harmonic vibration with a sinusoidal shape (Tedesco, McDougal, and Ross, 1999). A harmonic vibration can thus be described as a superposition of a sinusoidal vibration whose amplitudes depend on the zero-phase angle; this process can be better represented in the frequency domain.

Data were collected in the time domain using the Polytec PSV® and software (Polytec, 2015) and processed using MATLAB® (MATLAB, 2022; Hatch,2000), a matrix mathematical software.

Knowing the instrument sensitivity, the data is scaled by multiplying by the voltage magnitude to obtain the desired response in the time domain. This operation is performed in the Data Acquisition System (DAQ).

For time-domain analysis, digital filters are used to condition signals. Without using digital filters, the signal contains frequencies between 0 Hz to$f_S/2$, the Nyquist frequency$\left(f_{Nyquist}\right)$. This is optimal for evaluating spectra (Löwenborg, Gustafsson, and Wanhammar, 1999). As the FFT breaks the signal into individual frequencies, the different frequencies do not disturb each other. However, in the time domain, signal portions of all frequencies are visible simultaneously and overlap. Meaning that the signal to be analyzed is undesired to be covered by other signals. Digital filters are used to suppress these undesired signal parts.

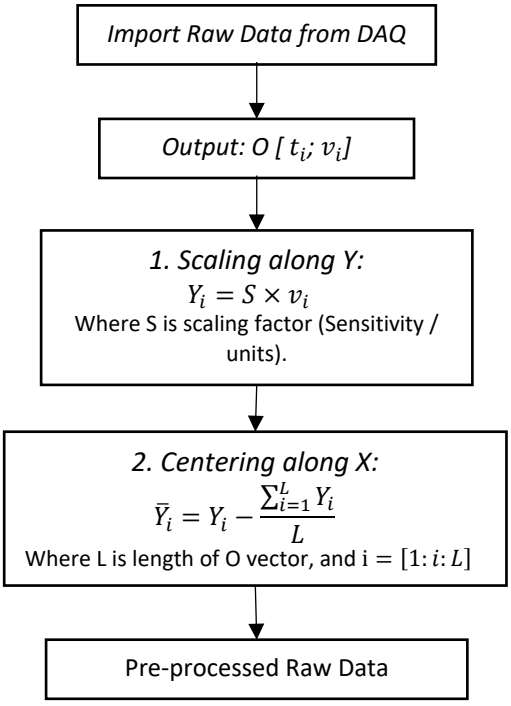

Figure 28: Raw data pre-processing steps

All the filters were designed using MATLAB functions from the Signal Processing Toolbox, with the help of a graphical user interface design program. The filters are finite impulse response (FIR) -based, designed to have a linear phase that introduces a delay in the filtered signal while maintaining the waveform shape (MATLAB, 2022).

Figure 29 shows the typical filter model where the pass band frequency (f_{Pass}) is slightly higher or lower than the first forcing frequency(f_{d1}), for the low pass filter. The Low pass filters allow lower frequencies to pass and attenuate higher frequencies.

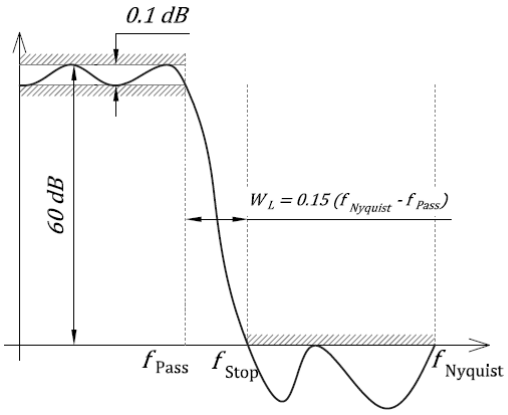

Figure 29: Low pass filters design model

To better enhance the desired response in the time domain, digital filters were used and later integrated and differentiated to obtain displacement, velocity, and acceleration, and vice-versa. Integration in the time domain usually only works satisfactorily if the time signal does not have an offset (Polytec, 2015). An offset causes a ramp in the integrated signal and can be eliminated using a centering along x. The equation below shows the integration of displacement and velocity using velocity and acceleration time-domain data, respectively.

$$\boldsymbol{x_i = x_{i-1} + \dot{x}_i \Delta t} \tag{9}$$

$$\boldsymbol{\dot{x}_i = \dot{x}_{i-1} + \ddot{x}_i \Delta t} \tag{10}$$

Where:
Δt is the time step and is equal to inverse of sampling frequency i.e., $1/f_S$
x_i is the displacement at time t_i
x_{i-1} is the displacement at time t_{i-1}
$\dot{x}_i$ is the velocity at time t_i
$\dot{x}_{i-1}$ is the velocity at time t_{i-1}
$\ddot{x}_i$ is the acceleration at time t_i.

A derivative is used to convert displacement into velocity or velocity into acceleration. By differentiating twice, displacement can be converted into acceleration. Differentiating in the time

domain usually does not present any difficulties (Polytec, 2015). Equations 11 and 12 show the differentiation of the velocity and acceleration using displacement and velocity time-domain data.

$$\dot{x}_i = \frac{x_i - x_{i-1}}{\Delta t} \tag{11}$$

$$\ddot{x}_i = \frac{\dot{x}_i - \dot{x}_{i-1}}{\Delta t} \tag{12}$$

Figure 30 shows data processing steps for trains 6 and 11, where steps 1-2 show the centering or DC bias removal effect, and steps 3-4 show the application of the low pass filter to obtain the displacement (see appendix for raw data).

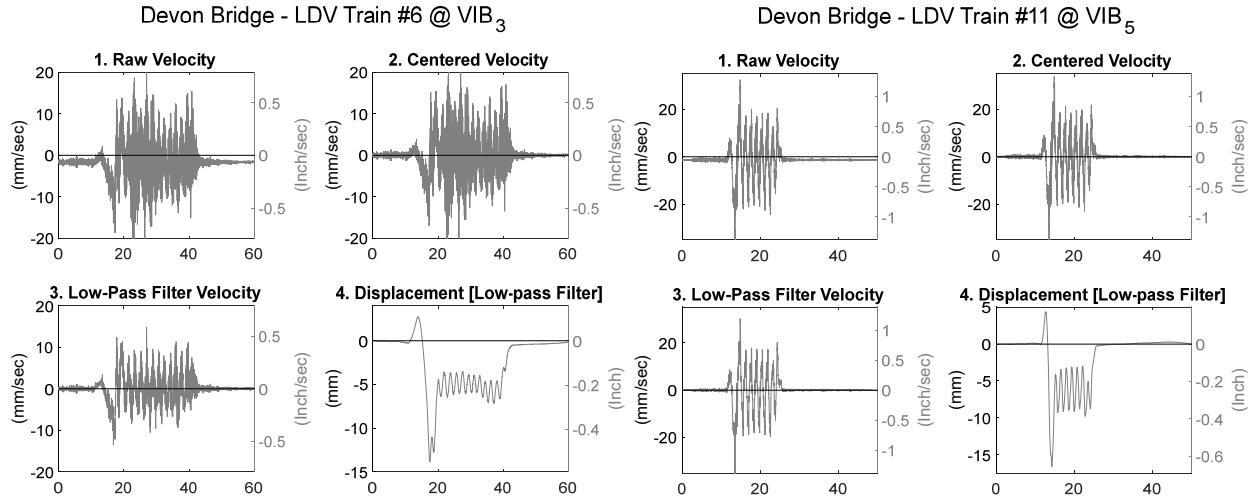

Figure 30: Devon bridge: Time-domain data processing, (a) Train 6, (b) Train 11

The other significant engineering time domain response is acceleration. It can be used to establish passenger level of comfort (AREMA, 2017; CFR, 2022). The FRA has defined the acceleration safety limits for the vehicle/track interaction. For example, the car body and truck lateral accelerations are measured using peak-to-peak and RMS acceleration, respectively. The peak-to-peak acceleration is defined as the maximum peak value at a cut-off frequency of 10Hz and 1-second windows, whereas the RMS is calculated by computing the square root of the mean of the squares value at a cut-off frequency of 10Hz and 2-second windows (CFR, 2022).

$$\boldsymbol{RMS} = \left(\frac{\sum_{n=1}^{n_s} y_n^2}{n_s}\right)^{\frac{1}{2}} \tag{13}$$

Where:

y_n is time domain data at instant *i*.

n_s is number of samples.

For a single unitary sinusoidal wave as shown in figure 31:

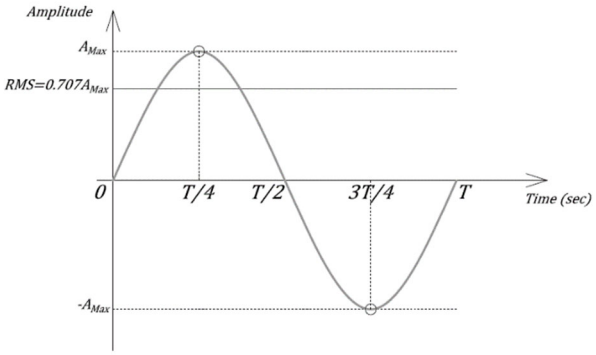

Figure 31: Root Mean Square calculation

Where the $y_n = 1.0$ and $n_s = 2$, the equation becomes:

$$\boldsymbol{RMS = \frac{1}{\sqrt{2}} A_{MAX} \approx 0.707 A_{MAX}} \quad (14)$$

RMS values are calculated for the desired bandwidth and spectrum range defined by the reference code (AREMA, 2017; CFR, 2022).

2.4.6 Data Processing in Frequency-domain

Digital filters change the spectrum response calculated from the time domain data, therefore if spectra are all to be evaluated, then digital filters are not necessary as a general rule (Polytec, 2015).

The repetitive train response represents a harmonic excitation with a sinusoidal shape. A harmonic vibration is described by angular frequency (ω), amplitude (A) and zero phase angle (φ_o) as follows:

$$\boldsymbol{U(t) = ACos(\omega t + \varphi_o)} \quad (15)$$

Using angle sum trigonometric identity, the above equation can be rewritten in terms of equation 16 as:

$$\boldsymbol{U(t) = ACos\varphi_o . Cos\omega t - ASin\varphi_o . Sin\omega t} \quad (16)$$

The harmonic vibration can be described as a superposition of a sinusoidal vibration whose amplitudes depend on the zero-phase angle (Tedesco, McDougal and Ross 1999). The harmonic vibration is better represented for mathematical analysis and data processing using a complex number plane. Therefore, the harmonic vibration $U(t)$ can be rewritten as equation 17.

$$\boldsymbol{\underline{U}(t) = Ae^{i(\omega t + \varphi_o)}} \quad (17)$$

The argument of the exponential function comprises a time-dependent part $i\omega t$ and a constant part $i\varphi_o$. By rearranging the equation as shown below, we obtain the complex amplitude $\left(Ae^{i\varphi_o}\right)$, which contains the information of the amplitude and phase angle of the vibration.

$$\boldsymbol{\underline{U}(t) = Ae^{i\varphi_o} . e^{i\omega t}} \quad (18)$$

Any recorded time signals can be converted to the frequency domain using the Fourier transform, in which convergent infinite series of trigonometric functions are described as periodic functions. Theoretically, the convergence of a Fourier series requires an infinite number of terms. However, a relatively small number of terms will provide a sufficiently accurate approximation of harmonic vibration.

$$\boldsymbol{U(t) = \frac{a_o}{2} + \sum_{n=1}^{\infty} [a_n \cos(n\omega t) + b_n \sin(n\omega t)]} \quad (19)$$

Where the coefficients a_o, a_n and b_n are given by:

$$a_o = \frac{2}{T_o}\int_0^{T_o} U(t)\, dt \tag{20}$$

$$a_n = \frac{2}{T_o}\int_0^{T_o} U(t)\, cos(n\omega t)\, dt \tag{21}$$

$$b_n = \frac{2}{T_o}\int_0^{T_o} U(t)\, sin(n\omega t)\, dt \tag{22}$$

The period (T_o) is given by $2\pi/\omega$ and n is the set of positive integers.

To calculate the transfer function, the equation of motion needs to be transformed using the Fourier transform, and the same can be presented in a complex number plane.

$$F(i\omega) = \int_{-\infty}^{\infty} U(t)e^{-i\omega t}\, dt \tag{23}$$

The Fast Fourier Transform (FFT) algorithm was used to generate the corresponding linear frequency spectrum (Polytec, 2015). Each frequency that appears in the time signal generates a spectral line in the FFT spectrum. The result of the FFT is a discrete spectrum. Only frequencies which fall precisely on an FFT line are shown correctly in the frequency range. If there are frequencies in the time signal that do not fall on an FFT line, the information in the spectrum is distributed over the neighboring FFT lines, known as the leakage effect. The leakage effect can be reduced by applying window functions (Hatch, 2000).

In order to reduce the leakage effect, windowing was applied through the use of the Hanning window. The Hanning window has the shape of an inverse, lifted cosine function. A window function should display even-sized attenuating behavior in the complete window spectrum with noisy measurement signals occurring in a noise excitation.

From the frequency spectra calculated using the FFT, the Auto Power Spectra at any channel (AP_{ss}) are calculated in the system using the spectrum at any channel (S).

$$AP_{ss} = S^*.S = |S|^2 \tag{24}$$

Power Spectrum Density (PSD) is used to measure random signals, the amplitude level of the FFT depends on the set resolution bandwidth (RBW) which is dependent on the bandwidth (BW), the number of FFT lines (N_{FFT}), and the window factor for the resolution bandwidth (W_{RBW}).

$$RBW = \frac{BW}{N_{FFT}}\, W_{RBW} \tag{25}$$

The PSD spectrum is calculated by dividing the Auto Power (AP) values by twice the resolution bandwidth.

$$PSD = \frac{AP}{2\, RBW} \tag{26}$$

Singular Value Decomposition (SVD) is used in the identification of natural frequencies of the Cos Cob Bridges from the collected field test data using Frequency Domain Decomposition (FDD). Further information on FDD can be found in (Kaium et al., 2020). SVD is a technique of handling a square matrix that does not have an inverse. The SVD of the PSD matrix, containing the PSD values computed from a set of velocity data, will help to identify the natural frequencies, which appear as a distinct peak of an SV matrix. A more detailed discussion on SVD can be found

in (Golub and Kahan, 1965). The SVD of an m-by-n matrix B containing the PSD values for a set of velocity data from a LDV, is given as:

$$[\boldsymbol{B}] = [\boldsymbol{U}][\boldsymbol{W}][\boldsymbol{V}]^{\boldsymbol{T}} \quad (27)$$

Where, [U] = m-by-n matrix of the orthonormal eigenvectors of $[\mathbf{B}][\mathbf{B}]^{\mathbf{T}}$; $[\mathbf{V}]^{\boldsymbol{T}}$= transpose of an n-by-n matrix containing the orthonormal eigenvectors of $[\mathbf{B}][\mathbf{B}]^{\mathbf{T}}$; and [W] = n-by-n diagonal matrix of the singular values which are the square roots of eigenvalues of $[\mathbf{A}]^{\boldsymbol{T}}[\mathbf{A}]$.

2.5 Finite Element Model

Finite element (FE) models of the Devon and Cos Cob bridges have been developed to simulate the current bridge conditions under static and dynamic loads. This study has used technical references, such as inspection reports and as-built drawings, to model the existing bridges (Stantec, 2011; TransSystem and Lochner, 2021; American Bridge Company, 1905). In addition, the bridge's dynamic response data, collected during the field test, was used to estimate the vehicle traveling speed and the bridge's dynamic characteristics and response.

A few assumptions have been made in the modeling process:

1. Track irregularities are not included in the model.
2. The models have not considered the vehicle-bridge interaction for the transient analysis, and the axle loads were approximated as triangular loads with time variation.
3. The self-weight is only due to the bridge members, wood ties, and rails. Self-weight from other components is neglected.
4. External loads, such as live and environmental loads, are not considered during the FE analysis, except self-weight for static analysis and trains for transient analysis.
5. The train crosses the bridge span at a constant speed.
6. The laced cross-section has been approximated to a uniformly increased gross cross-section.

The bridge three-dimensional (3D) model has been created using ANSYS modeling software SpaceClaim. The model was developed using wire elements and the boundary conditions were manually defined to represent the bridge behavior. The original drawings and field inspection reports (dating from the 1900s) were used to generate the gross cross-section and equivalent cross-section, respectively.

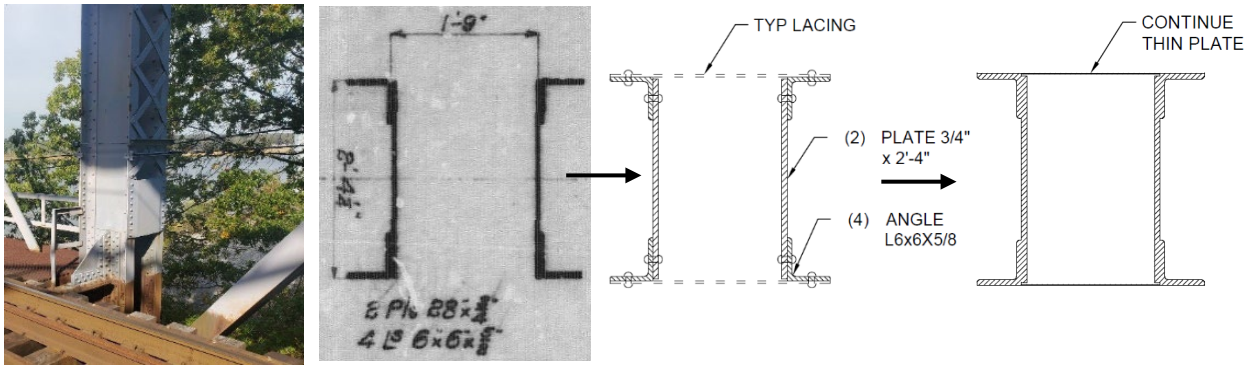

Figure 32: Devon bridge: Vertical post picture, original drawings, gross cross-section, and equivalent cross-section (left to right)

Old steel bridges are typically made of built-up members with laces connected with hot rivets. The model was simplified using Computer-Aided Design (CAD) software as solid members ignoring the rivets and using a thin plate to replace the lacing members. Figure 32 shows the CAD model development process for the vertical hanger on the Devon bridge.

The floor system, including tracks, ties, floor beam, and stringer, was designed on the same vertical plane to simplify the model. Therefore, the members were adjusted using the software's centroid offset command to represent the bridges better. For example, Figure 33 shows the Devon bridge floor system of the vertical post section with a cross-section variation and the respective offset dimensions from the centroid of the members to the projected plane. The red area represents all the members required to offset from the projected plane and the respective offset values.

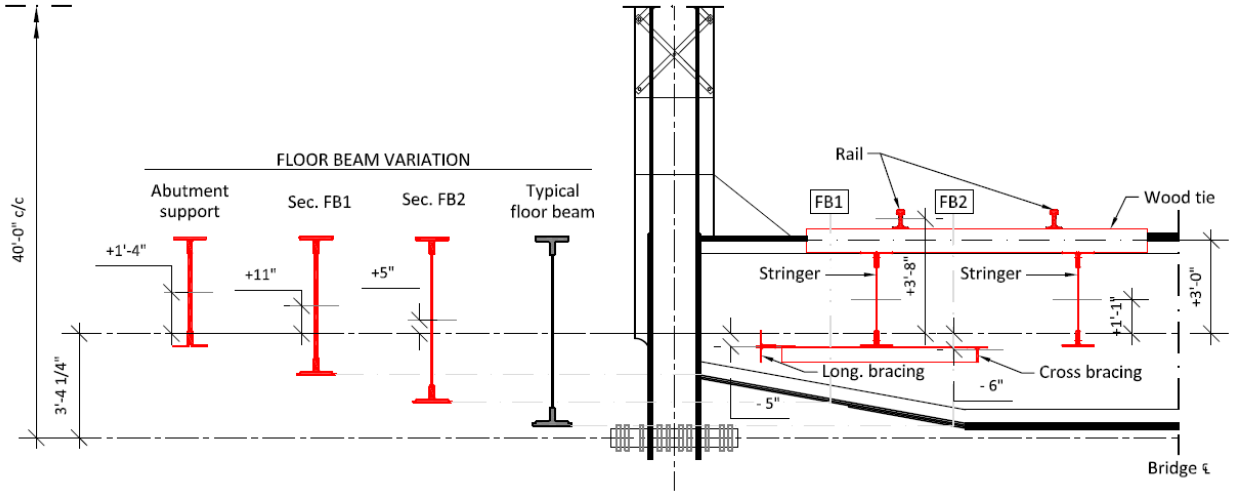

Figure 33: Devon bridge: Floor system and cross-section variation

The model used two types of material: structural steel and oak wood. This report used the default structural steel from the software. Therefore, the wood ties are the only members with the different assigned materials. In this case, this report used software default oak wood. The table below shows the mechanical properties of the material used in the FE model.

Table 6: Bridge material properties used in the FE model

Material Structural Parameters	Structural Steel		Oak Wood	
Young's Modulus	29,008 ksi	200 GPa	3,304 ksi	23 GPa
Poisson's Ratio	0.3	0.3	0.3742	0.3742
Tensile Ultimate Strength	66,717 psi	460 MPa	21,277	146 MPa
Tensile Yield Strength	36,259 psi	250 MPa	6,927	48 MPa
Density	0.28 lbm/in^3	4.54 kg/m^3	0.03 lbm/in^3	0.54 kg/m^3

The transient structural analysis represents and analyses the bridge's dynamic response and characteristics using the most common train compositions, the Metro-North Railroad M8, the Amtrak Regional, and the Amtrak Acela.

For example, the Devon bridge was divided into 144 equal parts to represent the axle step load locations. The distance of the step load can be converted to time using the vehicle's traveling speed. Figure 34 shows the model of the train entering the bridge span at step 1, representing the typical traveling direction recorded from the field test data, from east to west.

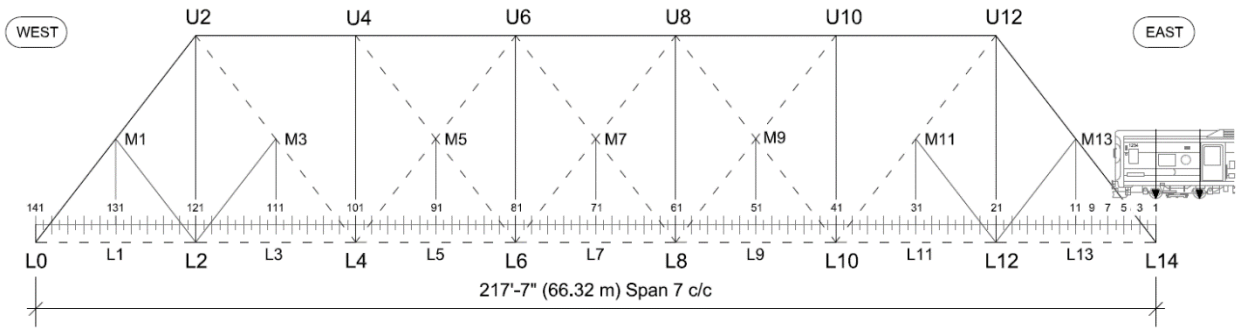

Figure 34: Devon bridge South trusses view with instrumentation location and train number

This study uses a series of triangular step loads to represent the moving axles of the vehicles. The load time is defined by dividing the axle load (Δs) by the desired vehicle traveling speed (v). The integration time was defined in the software using the sub-steps of the step load.

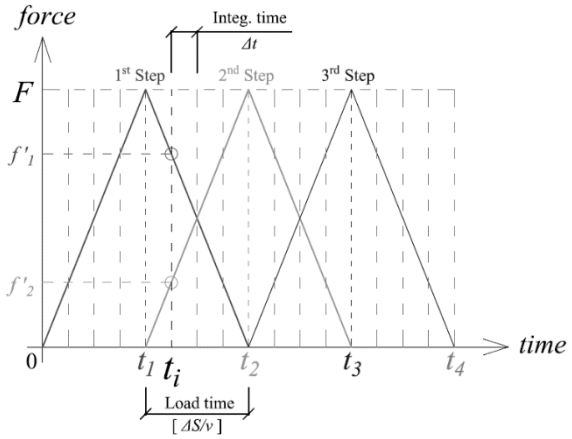

Figure 35: Step load model of constant force

Figure 35 shows an example of one constant moving load at three different steps. At the instantt_i, step loads 1 and 2 are active with the corresponding force of f'_1 and f'_2, respectively. However, step load 3 is not active now and is only activated after timet_2.

2.5.1 Typical Vehicles (Trains) Loading on the Bridges

Both the Devon and Cos Cob bridges are used by Amtrak (Acela and Regional) and Metro–North passenger trains for crossing the Housatonic River between Milford and Stratford, and

Mianus River in Greenwich, Connecticut, respectively. The axle arrangements and axle load of the passenger trains considered for this study are shown in Figure 36, which was developed by a previous research team (Jacobs, 2021) and updated to meet current conditions.

The MTNR M8 is an electric multiple-unit railroad car built by Kawasaki Rail Car, Inc., for exclusive use on the Metro-North Railroad New Haven Line and the CT*rail* Shore line east. The train can reach a maximum speed of 100 mph (161 km/h) and an operation speed of 80 mph (129 km/h). The typical composition is four to five married (double) cars with the same axle load (Lochner, 2011).

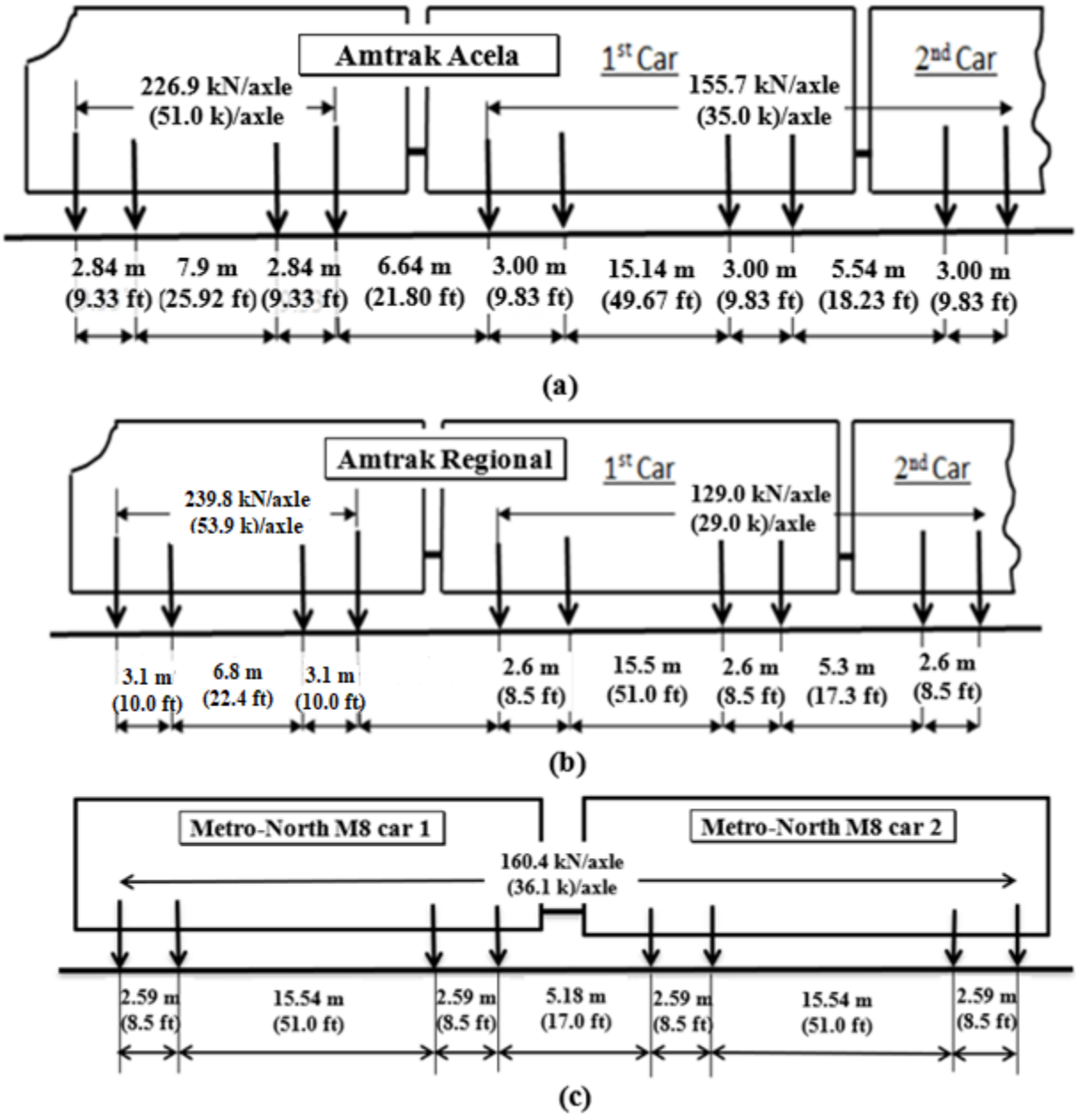

Figure 36: Typical vehicles, (a) Amtrak Acela, (b) Amtrak Regional and (c) Metro-North M8

The Amtrak Regional is an intercity rail service that connects major cities along the Northeast Corridor (NEC). Train composition consists of seven to nine passenger cars hauled by a power car. For the New Haven line, the coaches are Amfleet and can be of different types, including long- and short-distance coaches, cafes, club cars, and lounges. The power car is usually an electric locomotive designed by Siemens Mobility, the ACS-64. The Siemens ACS-64 can reach a maximum speed of 135 mph (217 km/h) and an operation speed of 125 mph (201 km/h) (AREMA, 2017; Siemens, 2019).

The Amtrak Acela was built to specification by the consortium of Bombardier Transportation and Alstom and is currently the fastest and busiest passenger train in North America, reaching a maximum speed of 150 mph (240 km/h). Unfortunately, due to the old infrastructure on the NEC, the train only reaches the maximum speed at 10% of the section of the 457 miles corridor from Boston to Washington DC (Burns, 2022). The fixed composition comprises two end power engines with heavier axle loads and six couches with lighter axle loads.

The approximated axle load and spacing used for the FE model are shown on Figure 37. This study has used a constant triangular step load to represent the train movement.

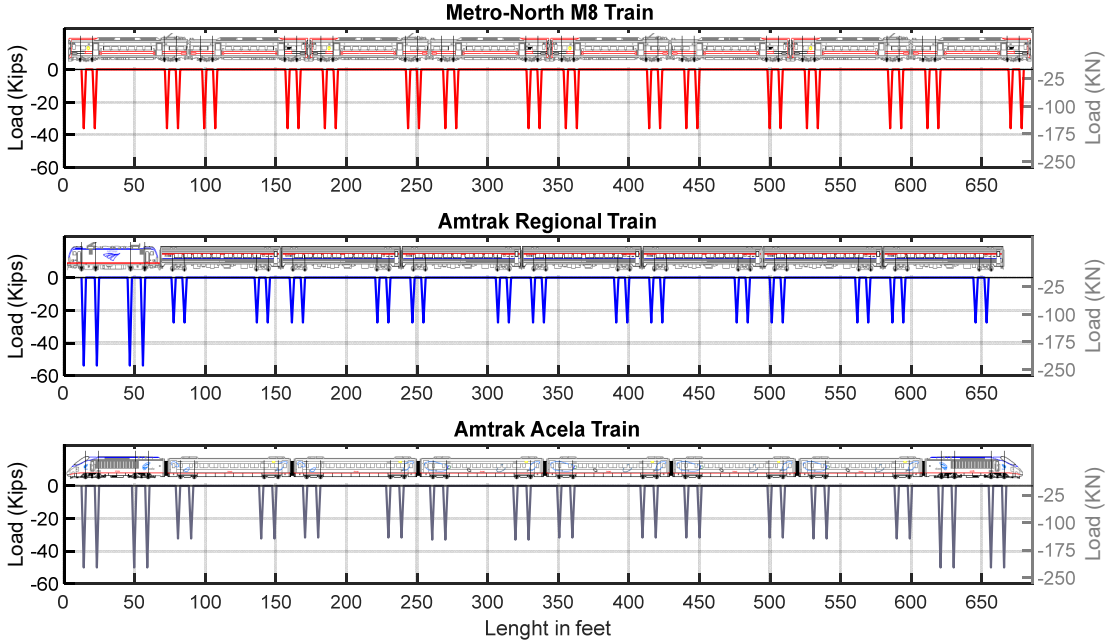

Figure 37: FE Model Axle load in triangle step load: (a) MTNR M8 specifications, (b) AMTK Regional specifications, and (c) AMTK Acela

2.5.2 Structural Dynamic Theory used in the FE Analysis

All the structural simulations were performed using the commercial FE software, ANSYS Workbench®, a Computer Aided Engineering software. Three types of global structural analysis were performed on the selected bridges: static, transient, and modal (ANSYS, 2009).

Static Analysis: The static analysis ignores the inertia and damping effects, except for static acceleration fields. The equilibrium equation for a linear static analysis is given below:

$$[\boldsymbol{K}]\{\boldsymbol{u}\} = \{\boldsymbol{F}\} \quad (28)$$

Where:
$[K]$ is the structural stiffness matrix
$\{u\}$ is the nodal displacement vector
$\{F\}$ is the total load vector.

Transient Analysis: For the transient analysis solution, assuming that the initial conditions are known, the software uses the second-order system, and the equilibrium equation is defined as:

$$[\boldsymbol{M}]\{\ddot{\boldsymbol{u}}\} + [\boldsymbol{C}]\{\dot{\boldsymbol{u}}\} + [\boldsymbol{K}]\{\boldsymbol{u}\} = \{\boldsymbol{F}\} \quad (29)$$

Where:
$[C]$ is the structural damping matrix
$\{\dot{u}\}$ is the nodal velocity vector
$[M]$ is the structural mass matrix
$\{\ddot{u}\}$ is the nodal acceleration vector.

The software employs the Newmark time integration method for solving the implicit transient analysis problem. The Newmark method uses the finite difference expansion in the intervalΔt, in which it is assumed that:

$$\{\dot{\boldsymbol{u}}_{\boldsymbol{i+1}}\} = \{\dot{\boldsymbol{u}}_{\boldsymbol{i}}\} + [(\mathbf{1}-\boldsymbol{\delta})\{\ddot{\boldsymbol{u}}_{\boldsymbol{i}}\} + \boldsymbol{\delta}\{\ddot{\boldsymbol{u}}_{\boldsymbol{i+1}}\}]\Delta\boldsymbol{t} \quad (30)$$

$$\{\boldsymbol{u}_{\boldsymbol{i+1}}\} = \{\boldsymbol{u}_{\boldsymbol{i}}\} + \{\dot{\boldsymbol{u}}_{\boldsymbol{i}}\}\Delta\boldsymbol{t} + \left[\left(\frac{\mathbf{1}}{\mathbf{2}}-\boldsymbol{\alpha}\right)\{\ddot{\boldsymbol{u}}_{\boldsymbol{i}}\} + \boldsymbol{\alpha}\{\ddot{\boldsymbol{u}}_{\boldsymbol{i+1}}\}\right]\Delta\boldsymbol{t}^{\mathbf{2}} \quad (31)$$

Where:
α , δ are the Newmark integration parameters
$\Delta t = t_{i+1} - t_i$
$\{u_i\}$ is the nodal displacement vector at time t_i
$\{u_{i+1}\}$ is the nodal displacement vector at time t_{i+1}
$\{\dot{u}_i\}$ is the nodal velocity vector at time t_i
$\{\dot{u}_{i+1}\}$ is the nodal velocity vector at time t_{i+1}
$\{\ddot{u}_i\}$ is the nodal acceleration vector at time t_i
$\{\ddot{u}_{i+1}\}$ is the nodal acceleration vector at time t_{i+1}.

Once the full solution is obtained for$\{u_{i+1}\}$, velocity and acceleration are updated using the equations (33) and (33), respectively.

$$\{\ddot{\boldsymbol{u}}_{\boldsymbol{i+1}}\} = \frac{[\{\boldsymbol{u}_{\boldsymbol{i+1}}\}-\{\boldsymbol{u}_{\boldsymbol{i}}\}]}{\boldsymbol{\alpha}\Delta\boldsymbol{t}^{\mathbf{2}}} - \frac{\{\dot{\boldsymbol{u}}_{\boldsymbol{i}}\}}{\boldsymbol{\alpha}\Delta\boldsymbol{t}} - [\,\boldsymbol{\delta}\Delta\boldsymbol{t}\{\ddot{\boldsymbol{u}}_{\boldsymbol{i}}\}\,] \quad (32)$$

$$\{\dot{\boldsymbol{u}}_{\boldsymbol{i+1}}\} = \{\boldsymbol{u}_{\boldsymbol{i}}\} + [\,(\mathbf{1}-\boldsymbol{\delta})\Delta\boldsymbol{t}\{\ddot{\boldsymbol{u}}_{\boldsymbol{i}}\}\,] + [\,\boldsymbol{\delta}\Delta\boldsymbol{t}\{\boldsymbol{u}_{\boldsymbol{i+1}}\}\,] \quad (33)$$

Modal Analysis: The modal analysis, used to determine natural frequencies and mode shapes, is restricted to a free vibration, without prestressing and damping acting on the structure, using a constant mass and stiffness matrix. The structure has no time-varying forces or displacements. Using the above assumptions, the equation of motion for an undamped system is expressed in matrix form as given below:

$$[\boldsymbol{M}]\{\ddot{\boldsymbol{u}}\} + [\boldsymbol{K}]\{\boldsymbol{u}\} = \{\mathbf{0}\} \quad (34)$$

For a linear system, free vibration will be harmonic of the form:

$$\{\boldsymbol{u}\} = \{\boldsymbol{\phi_n}\} \cos \boldsymbol{\omega_n t} \quad (35)$$

Where:
$\{\phi_n\}$ is the eigenvector representing the mode shape of the nth natural frequency
ω_n is the nth natural circular frequency (rad/sec)
t is the time.

Thus, by combining Equations 34 and 35, we obtain:

$$(-\boldsymbol{\omega_n}^2[\boldsymbol{M}] + [\boldsymbol{K}])\{\boldsymbol{\phi_n}\} = \{\boldsymbol{0}\} \quad (36)$$

By rearranging and equating the determinant to zero, a solution is obtained, as given below:

$$\left|[\boldsymbol{K}] - \boldsymbol{\omega_n}^2[\boldsymbol{M}]\right| = \boldsymbol{0} \quad (37)$$

This is a typical eigenvalue problem which may be solved for up to n values of $\omega_n{}^2$ and n eigenvectors$\{\phi_n\}$.

The software outputs the natural frequency (f_n) instead of the circular frequency (ω_n); therefore, an internal conversion is performed below:

$$\boldsymbol{f_n} = \frac{\boldsymbol{\omega_n}}{\boldsymbol{2\pi}} \quad (38)$$

Where:
f_n is the nth natural frequency in Hz.

2.5.3 Devon Bridge Finite Element Model

The FE model of the Devon bridge (Figure 17) was created using wire and shell elements, in which 33 different cross-sections were assigned to the 483 members, e.g., eyebars, stringers, floor beams, and diagonals. The approximate total weight of the bridge is 1060 kips (5160 KN), calculated from the three-dimensional model. The software, ANSYS, uses the assigned member's volume and the corresponding material density, shown in Table 6. The mesh was generated with 19527 nodes and 10740 elements and an average mesh element size of 4.64 inches (113.68 mm).

The span under study is span seven (Figure 6) and is considered under simply supported conditions. The support bearings were modeled using a shell element, with the geometry and thickness assigned per as-built conditions (Stantec, 2011; TransSystem and Lochner, 2021). The support bearings connect the End post with the bottom Chord using a pin, allowing rotation in the bridge's longitudinal direction only. Lastly, the support bearings are fixed in node L0 (pier 6) and the roller in node L14 (abutment). The bridge has a complex eye bars system for the bottom Chord and diagonals, using a bundle of rectangular bars connected using a pin. Although the FE model bridge was modeled to account for individual eye bars and pin connectors, special attention has been given to the assembly so that the bars do not overlap. Figure 38-a shows the schematic arrangements of the members and the general nomenclature and code used throughout the document. Figure 38-b to 38-e shows a representative geometry and section properties used for the FE model of the Devon bridge.

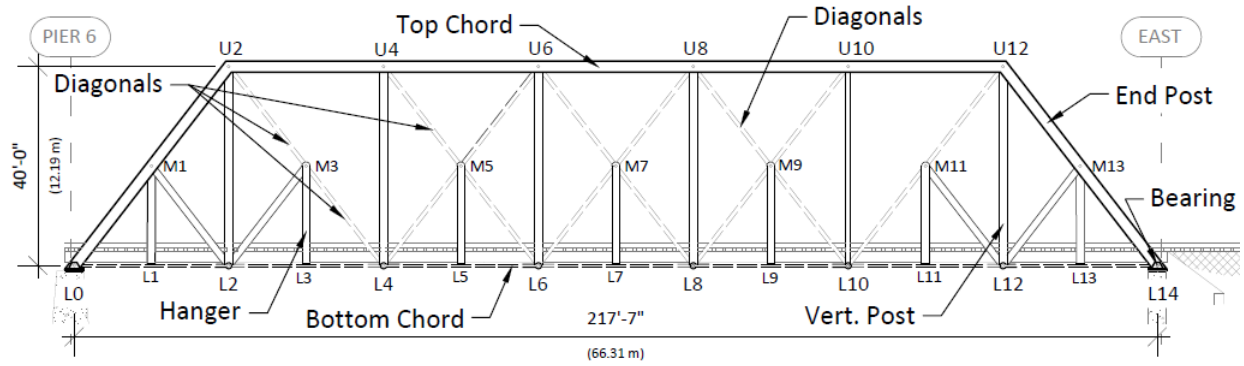

(a) Schematic arrangements of the members of Devon bridge

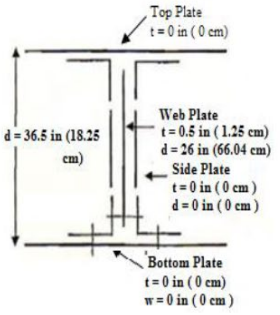

(b) Typical section of stringer.

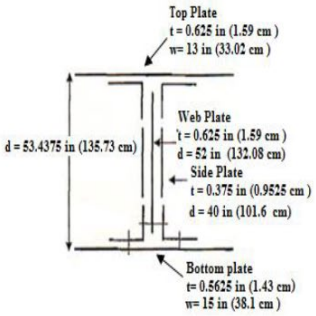

(c) Typical section of intermediate floor beam.

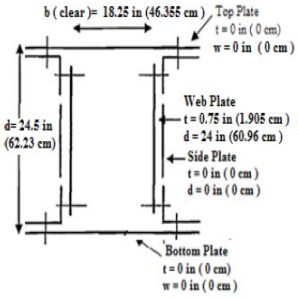

(d) Typical section of vertical L2-U2.

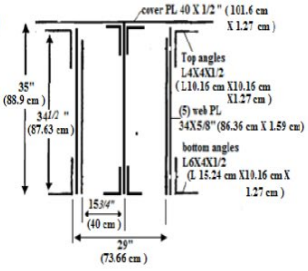

(e) Section view of top chord U2-U4.

Figure 38: Devon bridge: Schematic arrangement of principal members used for FE model, span 7.

The figure below shows the 3D model of the Devon bridge. While the wire model along with proper boundary conditions is shown on the left, the rendered view (displaying the assigned materials and cross-sections) is shown on the right in Figure 39.

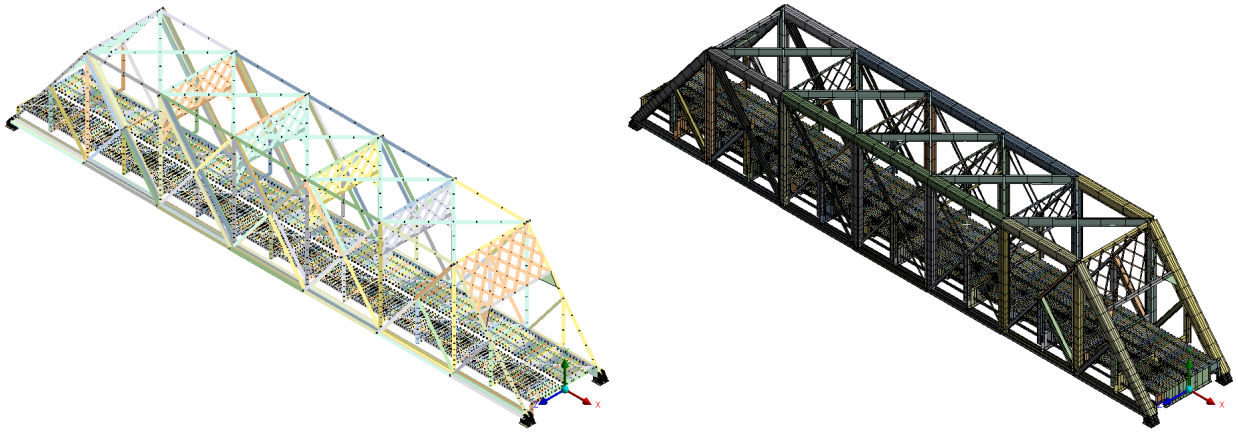

Figure 39: Devon bridge: FE model meshed with (a) wire elements, (b) render view of the model

This model does not account for any load or stress in the modal analysis. The static structural analysis with the permanent load includes only the self-weight of the structure and the permanent weight of the fixtures (tracks and ties). The vehicle influence line used for static and transient

structural analysis was typical MTNR M8, AMTK Regional, and AMTK Acela train compositions shown in Figure 37.

The selection of the appropriate integration time (Δt) is one of the most critical aspects of a dynamic transient analysis for multi-degree-of-freedom systems. The integration time affects the accuracy and the computational effort required.

ANSYS Workbench® uses the Newmark time integration method to calculate the transient dynamic structural response and is characterized as an implicit direct integration method (ANSYS, 2009). This method, in which the solution is from the equilibrium equation at time (t+Δt), is considered unconditionally stable, and accuracy rather than stability governs the selection of the time-step Δt (Tedesco, McDougal, and Ross, 1999). The figure below shows the accuracy and computational effort study to select the ideal integration time (Δt) for the Devon bridge. This study uses a fixed-point result from a constant model and computer to analyze the model with different integration time (Δt/i) and sub-steps. The figure below shows the accuracy and computational effort study for the Devon bridge transient analysis model. It can be concluded that integration time should be between 0.01 and 0.015 seconds to maximize accuracy and minimize computational effort.

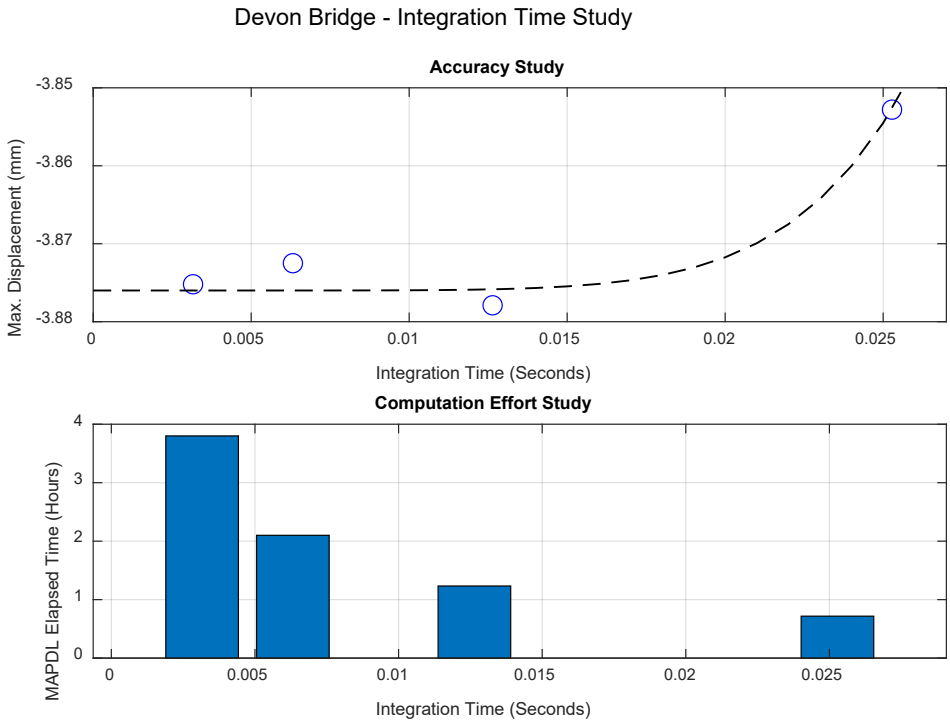

Figure 40: Devon bridge: accuracy and computational effort study

2.5.4 Cos Cob Bridge Finite Element Model

The three-dimensional Finite Element Model (FE model) of the span 3 (Figures 43 and 44) was developed using FE software-ANSYS. The geometry of the cross section of the members and the boundary conditions for the FE model are based on 'As Built' Drawing (Underwater Construction, 1990), Repair Plan Drawing (A.G. Lichtenstein & Associates, 1989) and Load Rating Report (Clough, Harbour and Associates, 2010). The length, width and height of the bridge are 122.08 ft., 7.5 ft., and 14.75 ft., respectively. The various members of the Cos Cob Bridge: top-chord, bottom-chord, floor beam, end post, upper lateral bracing, lower lateral bracing, diagonal members, vertical members, rails, and ties were modeled using beam element (Beam 188). Structural steel properties are assigned to all the members except ties, for which properties of Oak wood are assigned. Material properties used in the FE model are presented in Table 6. The actual end bearings of the span were modelled as roller supports for the expansion end, and as a hinge support for the fixed end of the span. Roller support of FE model has the released translation in longitudinal direction of the bridge but the translations in the other two directions were restrained, whereas the hinge support of FE model has translation in all three- directions restrained. The model has a total of 714 elements and 1346 nodes.

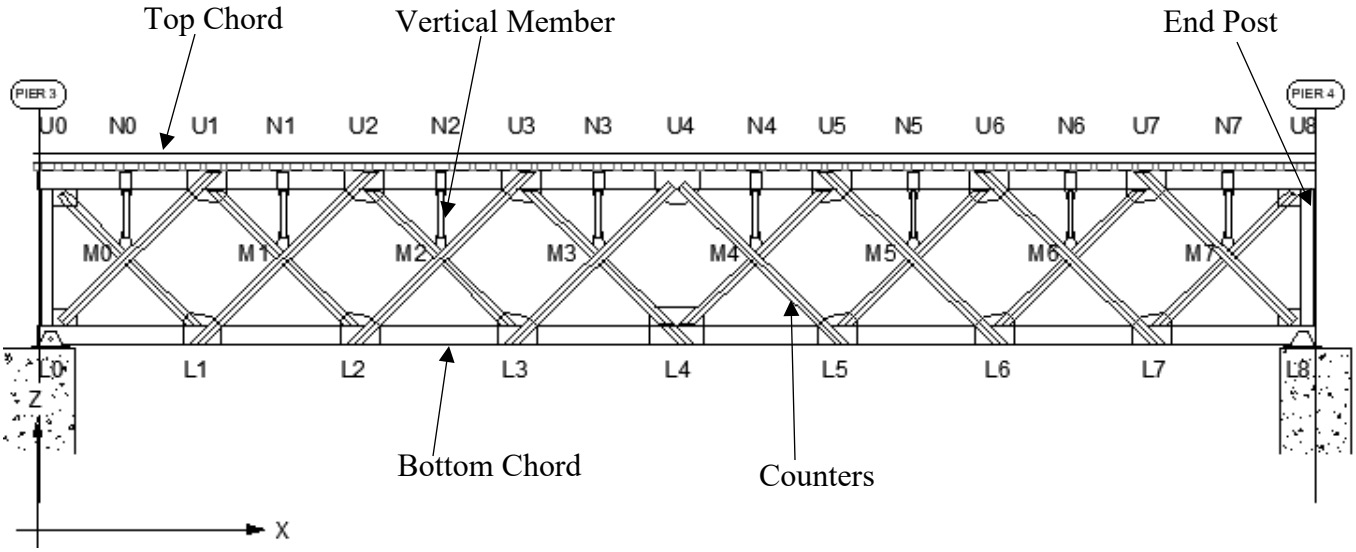

Figure 41: Schematic arrangement of the members in Cos Cob bridge

Cross section schematics and section properties for the principal members used in FE modeling are presented in Figure 42.

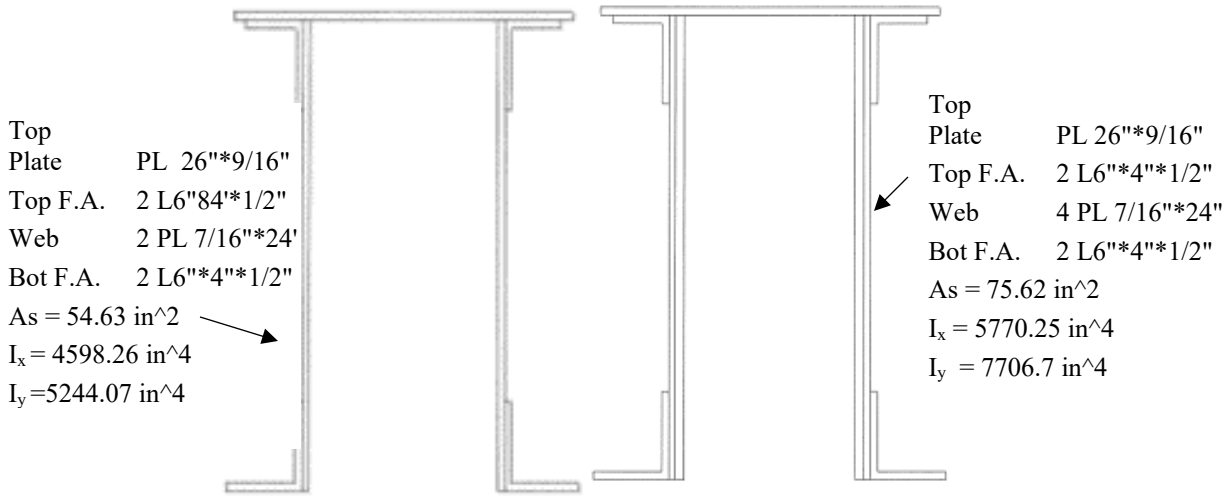

(a). Typical section; Node U0-U1, U7-U8 (Top Chord)

(b). Typical section; Node U1-U2, U6-U7 (Top Chord)

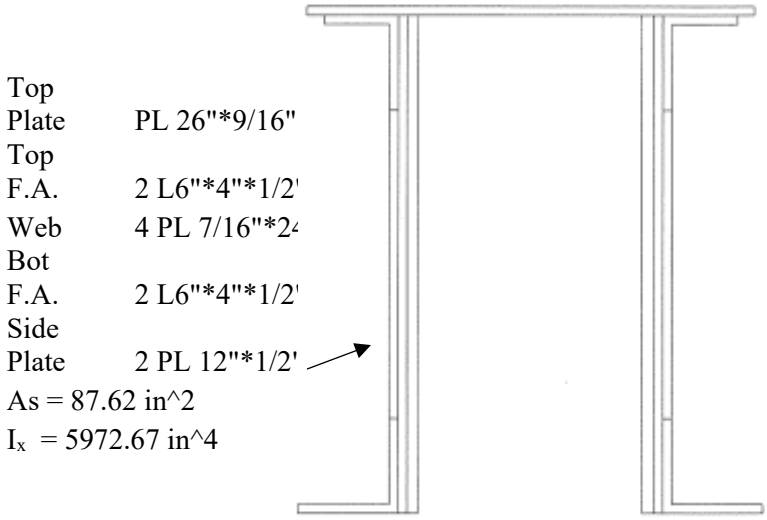

(c). Typical section; Node U2-U3, U5-U6 (Top Chord)

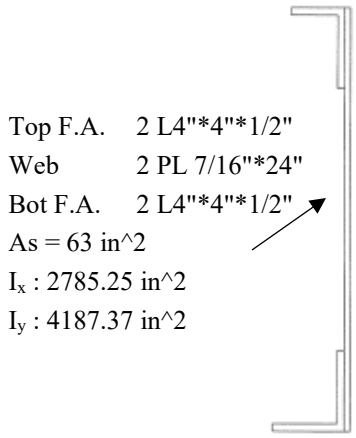

(d). Typical section; Node L0-L1, L7-L8 (Bottom Chord)

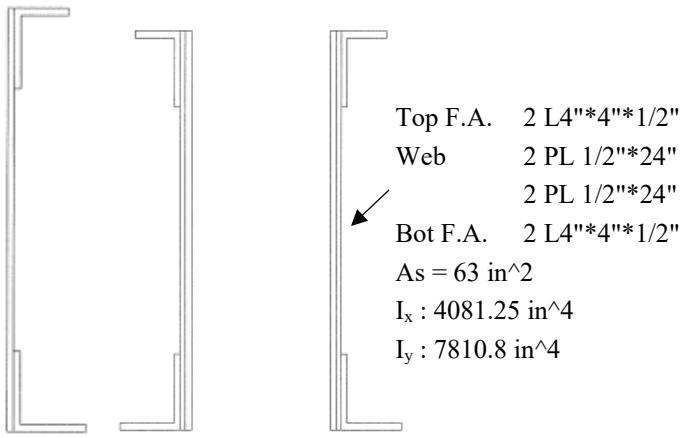

(e). Typical section; Node L1-L2, L6-L7 (Bottom Chord)

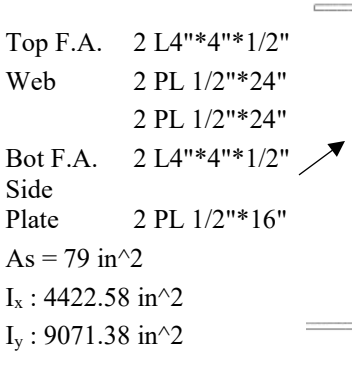

(f). Typical section; Node L2-L3, L5-L6 (Bottom Chord)

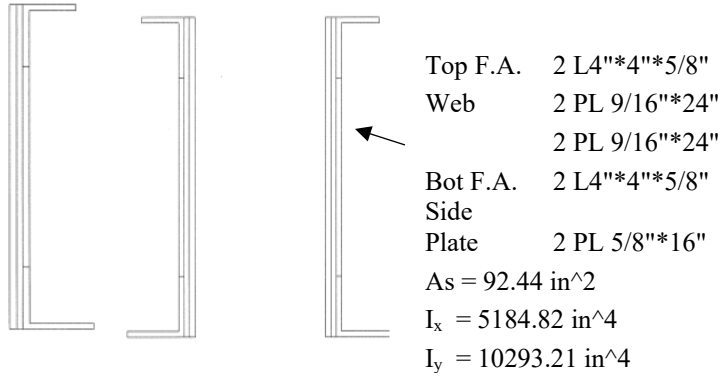

(g). Typical section; Node L3-L4, L4-L5 (Bottom Chord)

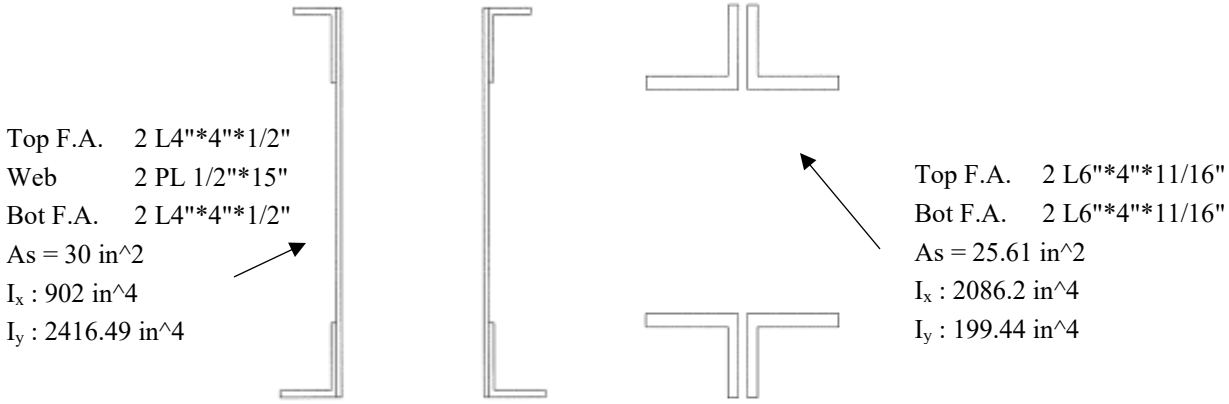

(h). Typical section; Node U0-L0, U8-L8 (End Post)

(i). Typical section; Node U2-L1 (Counters)

Figure 42: Schematic arrangement of the principal members of the Cos Cob bridge, span 3, and typical sections; (a-c) top chord, (d-g) bottom chord, (h) end post, (i) counters

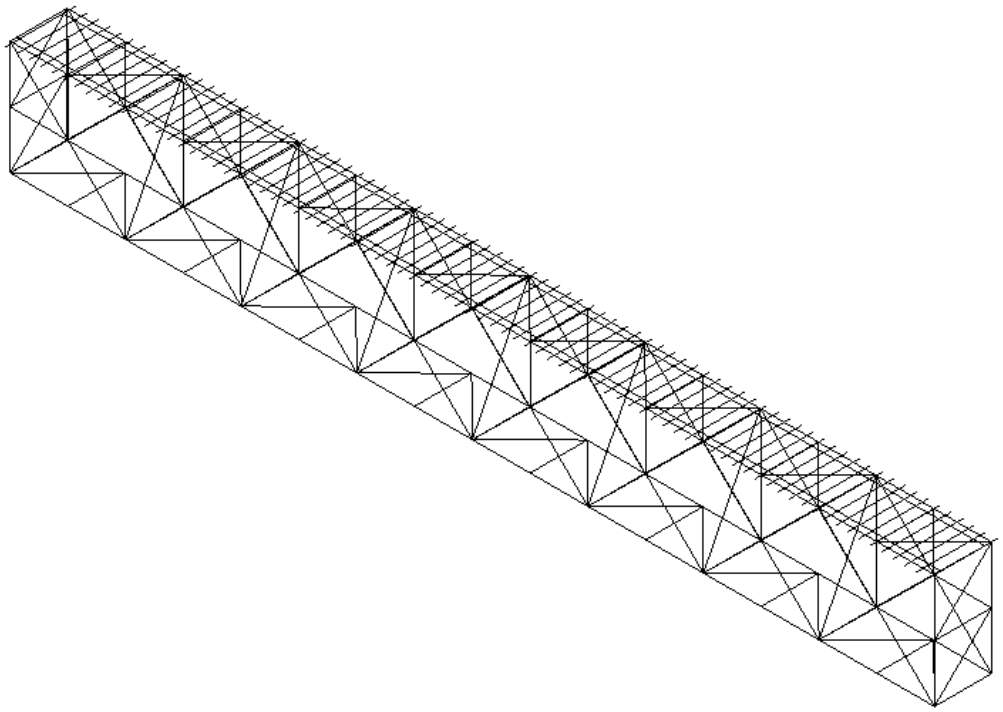

Figure 43: Cos Cob bridge 3D FE model (wire elements view)

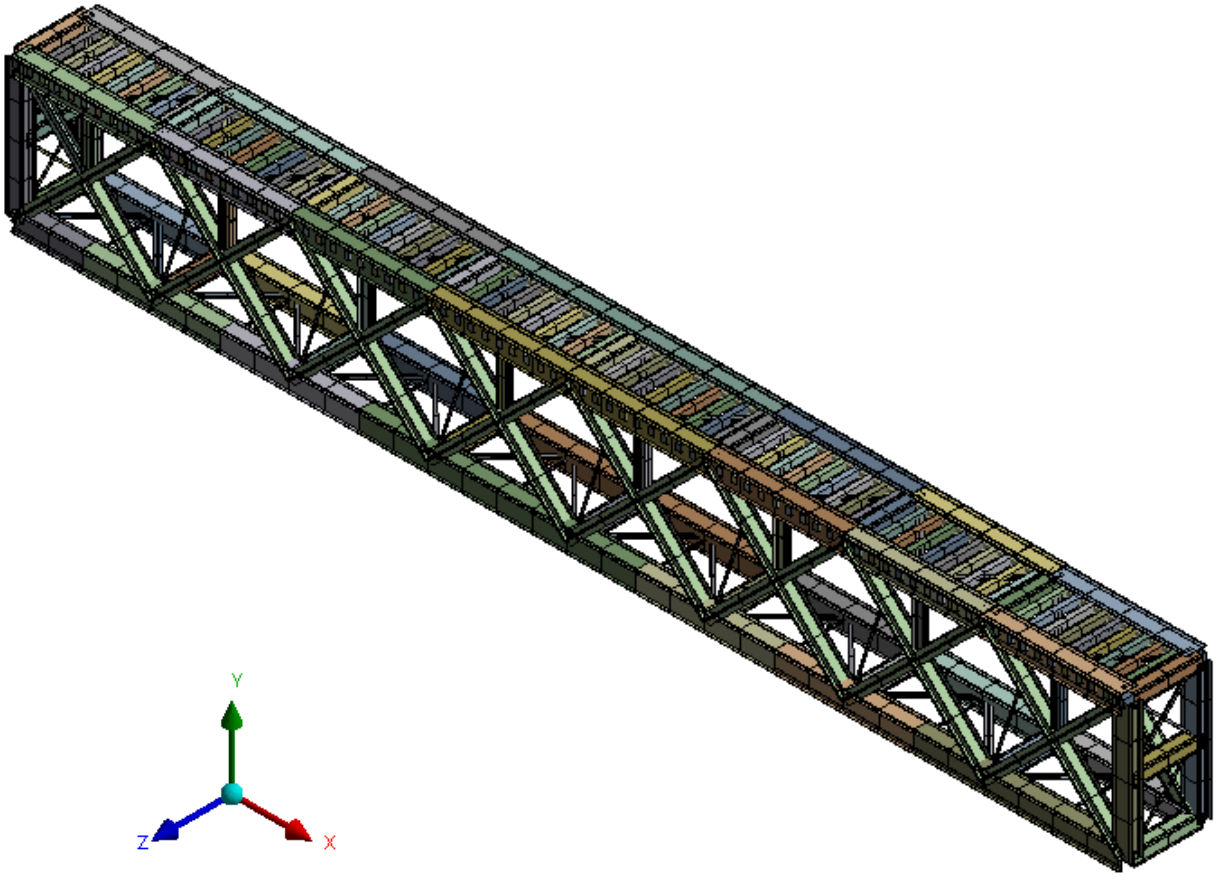

Figure 44: **Cos Cob bridge 3D FE model (render view)**

Chapter 3: Results and Discussion

In this chapter, we discuss the results of the various material tests, field tests, and simulations described in the preceding chapter. First, the material testing results from the Devon, Cos Cob, and other bridges are discussed. Second, the field test data from LDV is presented and interpreted in time and frequency domains. Finally, the field test data from LDV is compared with the FE model in the time and frequency domains.

3.1 Railroad Bridge Material Testing Results

Tensile tests were performed on the bridge materials collected from the Aroostook bridge (ME), Atlantic Street bridge (CT), Cos Cob bridge (CT) and Devon bridge (CT). While the materials from the later three bridges were tested at the extension rate of 4 mm/min, the materials from the Aroostook Bridge were tested at various extension rates (1 mm/min, 4mm/min, 8 mm/min, 100 mm/min and 500 mm/min) to understand the effect of extension rate on the tensile properties. Results obtained from the tensile tests performed on the studied bridge materials are presented in the following sub-section.

3.1.1 Devon Bridge

Three specimens from the Devon bridge material were tested at the extension rate of 4 mm/min. Extensions and the corresponding forces required to cause the extensions were recorded at the frequency of 2 Hz. Engineering stress- strain diagrams are plotted as shown in Figures 45 and 46. Dev_Sp1, Dev_Sp2 and Dev_Sp3 represent specimens 1, 2, and 3, respectively, fabricated from the collected Devon Bridge materials. The results are presented in terms of yield strength, yield strain, ultimate tensile strength, ultimate tensile strain, breaking point strength, and breaking point strain. Result statistics from the tested specimens are presented in terms of mean, standard deviation and the 95% confidence interval. The result shows a mean yield stress of 245 MPa with Standard Deviation (SD) of 2.6 MPa at 95% Confidence Interval (CI) of 6.56 MPa. Similarly, an ultimate tensile strength of 394 MPa was obtained, with SD of 0.26 MPa at 95% CI of 0.65 MPa. Further information on breaking stress, yield strain, ultimate tensile strain, and breaking strain can be found in Table 7.

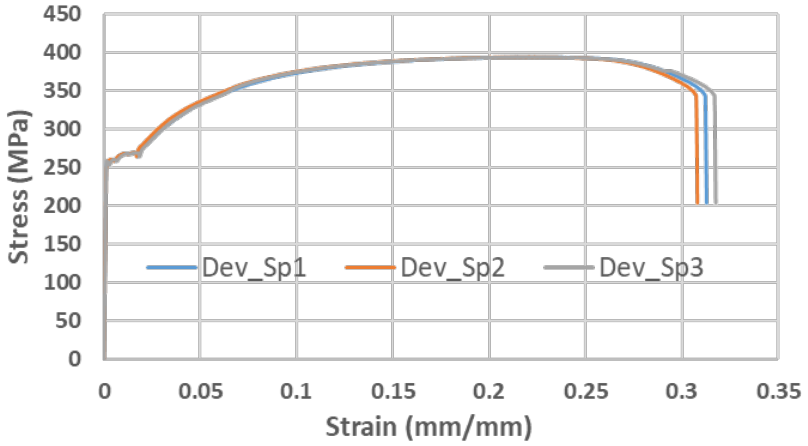

Figure 45: Tensile Stress-strain diagram, Devon bridge, CT; monotonic loading to failure; extension rate: 4mm/min. (Unit Conversion: 1 ksi = 6.9 MPa; 36 ksi = 248.2 MPa; 1 in = 25.4 mm)

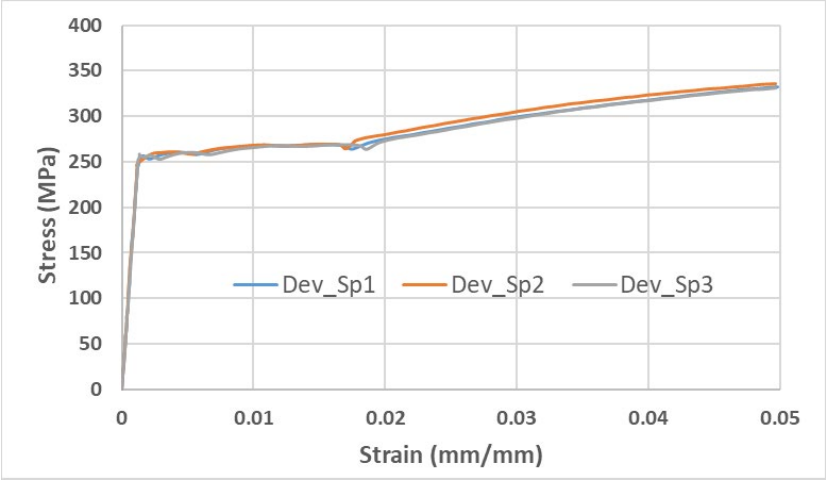

Figure 46: Tensile Stress-strain diagram, Devon bridge, CT; enlarged scale up to strain 0.05 mm/mm; extension rate: 4mm/min, (Unit Conversion: 1 ksi = 6.9 MPa; 36 ksi = 248.2 MPa; 1 in = 25.4 mm)

Table 7: Devon bridge (CT) Tensile Test Results

	Yield Stress (MPa)	Yield Strain (mm/mm)	Ultimate Tensile Stress (MPa)	Ultimate Tensile Strain (mm/mm)	Break Point Stress (MPa)	Break Point Strain (mm/mm)	Young's Modulus (GPa)
Extension rate: 4mm/min							
Specimen 1	242.7	0.00118	393.6	0.214	203.59	0.313	205.6
Specimen 2	247.5	0.00119	393.7	0.211	203.61	0.308	207.9
Specimen 3	243.2	0.00117	394.1	0.209	202.21	0.317	207.8
Mean	244.4[a]± 6.56[b]	0.00118[a]± 0.0000248[b]	393.8[a]± 0.65[b]	0.211[a]± 0.0062[b]	203.1[a]± 0.1.99[b]	0.312[a]± 0.011[b]	207.1[a]± 3.22[b]
Standard Deviation (SD)	2.6	0.00001	0.26	0.0025	0.801	0.0045	1.3

[a]Mean from 3 samples; [b] 95% Confidence interval (CI)

3.1.2 Cos Cob Bridge

Three specimens from the Cos Cob bridge material were tested at the extension rate of 4 mm/min. Extensions and the corresponding forces required to cause the extensions were recorded at the frequency of 2 Hz. Engineering stress-strain diagram are plotted as shown in Figures 47 and 48. CC_Sp1, CC_Sp2 and CC_Sp3 represent specimens 1, 2, and 3, respectively, fabricated from the collected Cos Cob Bridge materials. The results are presented in terms of yield strength, yield strain, ultimate tensile strength, ultimate tensile strain, breaking point strength, and breaking point strain. Result statistics from the tested specimens are presented in terms of mean, standard deviation and the 95% confidence interval. The result shows a mean yield stress of 232 MPa with Standard Deviation (SD) of 3.7 MPa at 95% Confidence Interval (CI) of 9.3 MPa. Similarly, an ultimate tensile strength of 360 MPa was obtained, with SD of 9.82 MPa at 95% CI of 24.4 MPa. Further information on breaking stress, yield strain, ultimate tensile strain, and breaking strain can be found in Table 8.

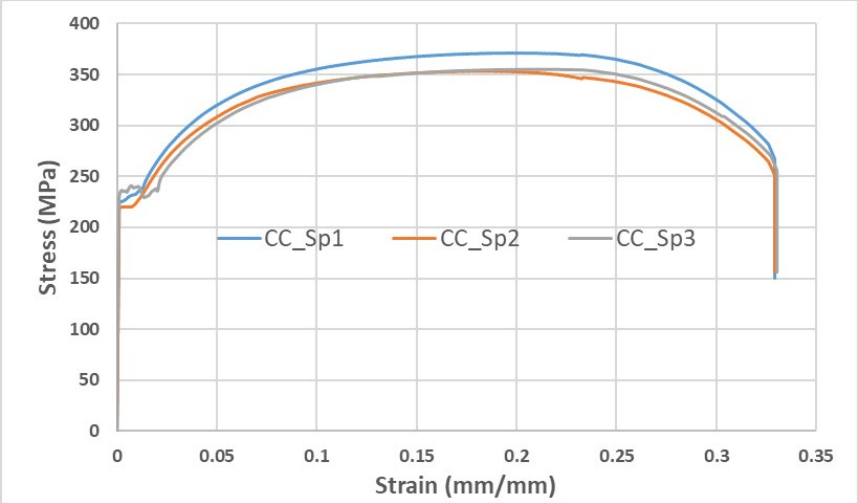

Figure 47: Tensile Stress-strain diagram, Cos Cob bridge, CT; monotonic loading to failure; extension rate: 4mm/min. (Unit Conversion: 1 ksi = 6.9 MPa; 36 ksi = 248.2 MPa; 1 in = 25.4 mm)

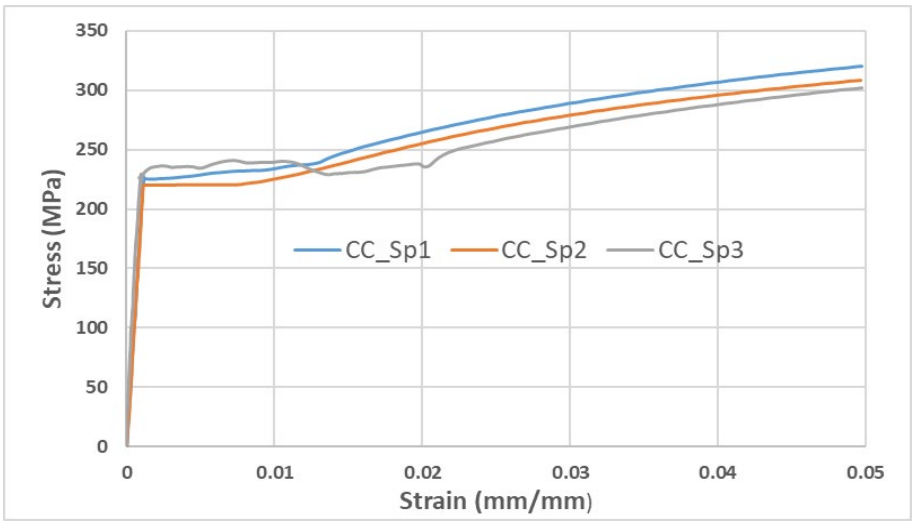

Figure 48: Tensile Stress-strain diagram, Cos Cob bridge, CT; enlarged scale up to strain 0.05 mm/mm; extension rate: 4mm/min, (Unit Conversion: 1 ksi = 6.9 MPa; 36 ksi = 248.2 MPa; 1 in = 25.4 mm)

Table 8: Cos Cob bridge (CT) Tensile Test Results

	Yield Stress (MPa)	Yield Strain (mm/mm)	Ultimate Tensile Stress (MPa)	Ultimate Tensile Strain (mm/mm)	Break Point Stress (MPa)	Break Point Strain (mm/mm)	Young's Modulus (GPa)
Extension rate: 4mm/min							
Specimen 1	236.1	0.00117	371.31	0.2067	150.1	0.3293	201.8
Specimen 2	228.9	0.00115	353.46	0.2093	156.5	0.3201	199.1
Specimen 3	230.4	0.00116	355.29	0.2102	156.1	0.3304	198.6
Mean	231.7[a]± 9.3[b]	0.00117[a] ± 0.0000799[b]	360.1[a] ± 24.4[b]	0.209[a] ± 0.0045[b]	154.2[a] ± 8.9[b]	0.326[a] ± 0.014[b]	197.7[a] ± 3.79[b]
Standard Deviation (SD)	3.74	0.0000321	9.82	0.0018	3.6	0.0057	1.53

[a] Mean from 3 samples; [b] 95% Confidence interval (CI)

3.1.3 Atlantic Street Bridge

Three specimens from the Atlantic Street bridge material were tested at the extension rate of 4 mm/min. Extensions and the corresponding forces required to cause the extensions were recorded at the frequency of 2 Hz. Engineering stress-strain diagram are plotted as shown in Figures 49 and 50. At_Sp1, At_Sp2 and At_Sp3 represent specimens 1, 2, and 3, respectively, fabricated from the collected Atlantic Street Bridge materials. The results are presented in terms of yield strength, yield strain, ultimate tensile strength, ultimate tensile strain, breaking point strength, and breaking point strain. Result statistics from the tested specimens are presented in terms of mean, standard deviation and the 95% confidence interval. The result shows a mean yield strength of 249 MPa with Standard Deviation (SD) of 3.76 MPa at 95% Confidence Interval (CI) of 9.35 MPa. Similarly, an ultimate tensile strength of 436 MPa was obtained with SD of 2.31 MPa at 95% CI of 5.74 MPa. Further information on breaking strength, yield strain, ultimate tensile strain, and breaking strain can be found in Table 9.

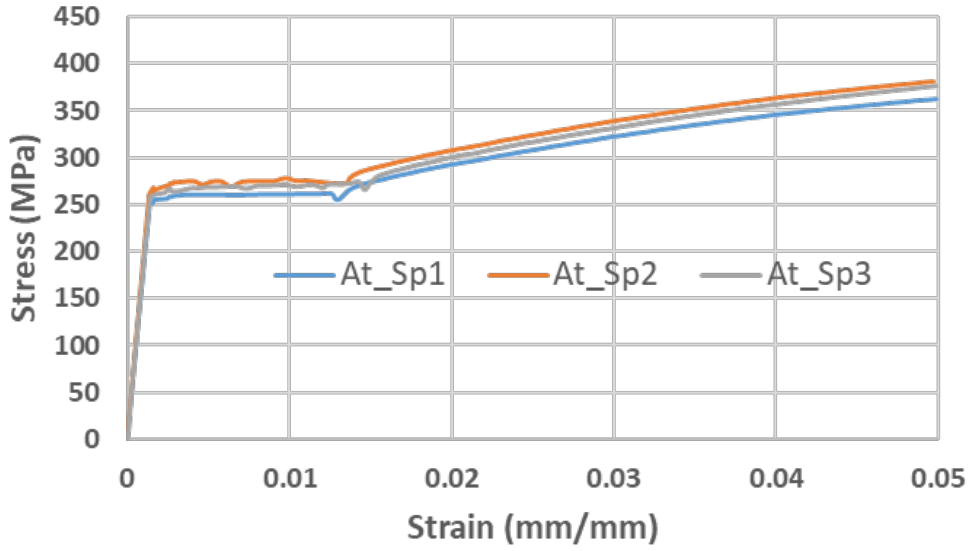

Figure 49: Tensile Stress-strain diagram, Atlantic Street bridge, CT; monotonic loading to failure; extension rate: 4 mm/min. (Unit Conversion: 1 ksi = 6.9 MPa; 36 ksi = 248.2 MPa; 1 in = 25.4 mm)

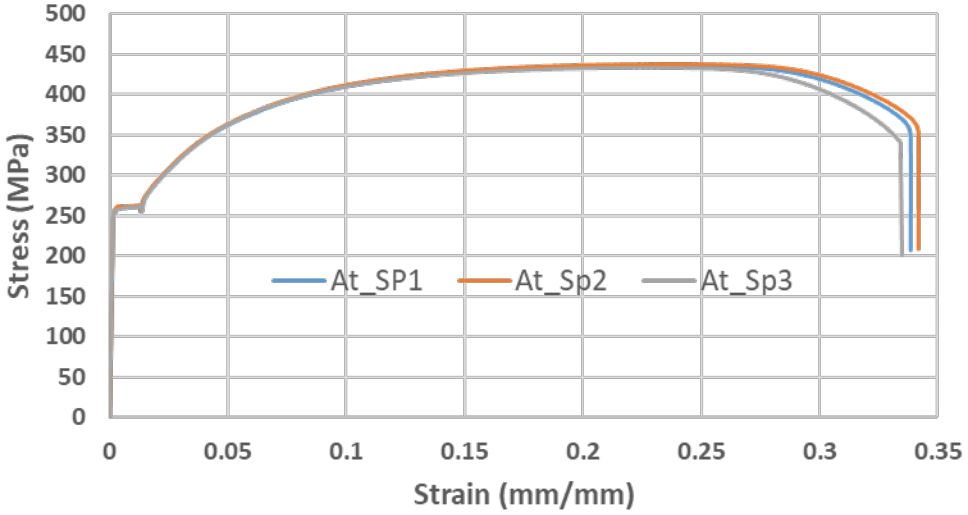

Figure 50: Tensile Stress-strain diagram (Atlantic Street bridge, CT); Enlarged scale up to strain 0.05 mm/mm; extension rate: 4 mm/min, (Unit Conversion: 1 ksi = 6.9 MPa; 36 ksi = 248.2 MPa; 1 in = 25.4 mm)

Table 9: Tensile Test Results- Atlantic Street bridge (CT)

	Yield Stress (MPa)	Yield Strain (mm/mm)	Ultimate Tensile Stress (MPa)	Ultimate Tensile Strain (mm/mm)	Break Point Stress (MPa)	Break Point Strain (mm/mm)	Young Modulus (GPa)
Extension rate: 4 mm/min							
Specimen 1	249.8	0.00139	435.4	0.219	347.5	0.339	179.7
Specimen 2	244.9	0.00134	438.1	0.221	349.6	0.341	182.7
Specimen 3	252.3	0.00137	433.5	0.209	339.9	0.334	184.2
Mean	$249^a \pm 9.35^b$	0.001367 ± 0.0000621^b	$435.6^a \pm 5.74^b$	$0.216^a \pm 0.016^b$	$345.6^a \pm 12.6^b$	$0.338^a \pm 0.0089^b$	$182.2^a \pm 5.69^b$
Standard Deviation (SD)	3.76	0.0000252	2.31	0.0064	5.1	0.0037	2.91

[a]Mean from 3 samples; [b] 95% Confidence interval (CI)

3.1.4 Aroostook Bridge

Specimen from the Aroostook bridge were tested at different extension rates (1 mm/min, 4 mm/min, 8 mm/min, 10 mm/min, and 500 mm/min) to understand the effect of loading rate on tensile properties (yield strength, ultimate tensile strength, and breaking point strength).

3.1.4.1 *Extension Rate: 1 mm/min*

Three specimens from the Aroostook bridge material were tested at the extension rate of 1 mm/min. Extensions and the corresponding forces required to cause the extensions were recorded at the frequency of 2 Hz. Engineering stress-strain diagram are plotted as shown in Figures 51 and 52. Arr_Sp1, Arr_Sp2 and Arr_Sp3 represent specimens 1, 2, and 3, respectively, fabricated from the collected Aroostook Bridge materials. The results are presented in terms of yield strength, yield strain, ultimate tensile strength, ultimate tensile strain, breaking point strength, and breaking point strain. Result statistics from the tested specimens are presented in terms of mean, standard deviation, and the 95% confidence interval. The result shows a mean yield strength of 245 MPa with Standard Deviation (SD) of 2.64 MPa at 95% Confidence Interval (CI) of 6.55 MPa. Similarly, an ultimate tensile strength of 395 MPa was obtained with SD of 6.35 MPa at 95% CI of 15.78 Mpa. Further information on breaking strength, yield strain, ultimate tensile strain, and breaking strain can be found in Table 10.

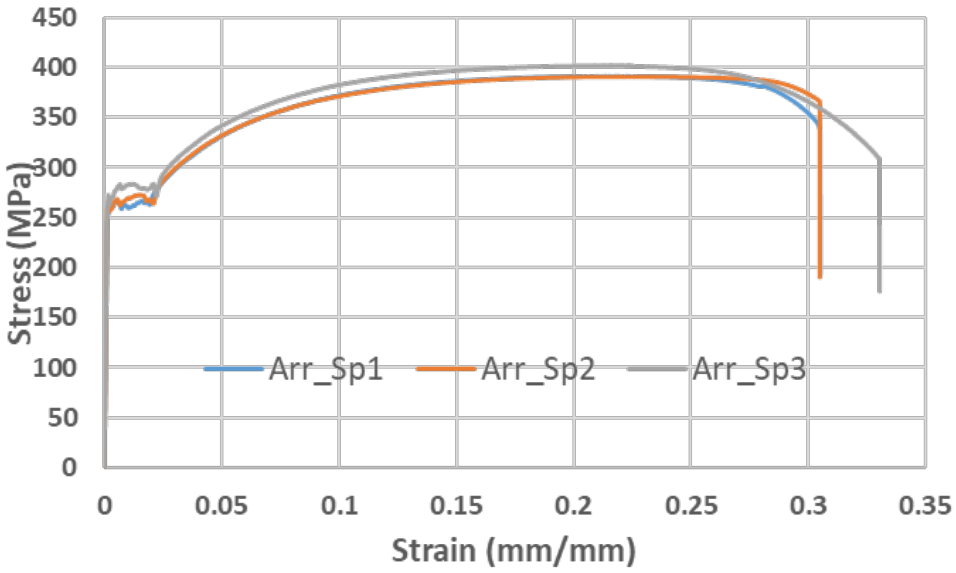

Figure 51: Tensile Stress-strain diagram, Aroostook bridge, Maine; monotonic loading to failure; extension rate: 1mm/min. (Unit Conversion: 1 ksi = 6.9 MPa; 36 ksi = 248.2 MPa; 1 in = 25.4 mm)

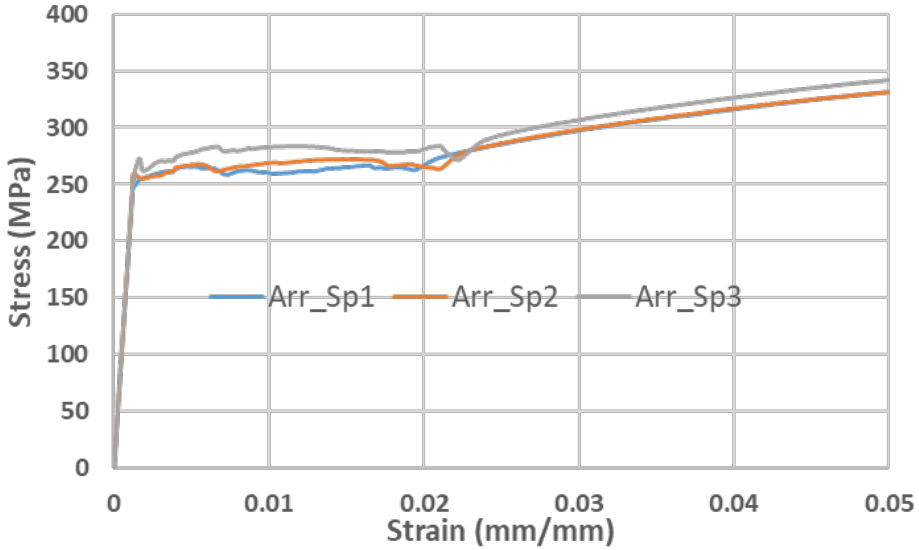

Figure 52: Tensile Stress-strain diagram, Aroostook bridge, enlarged scale up to strain 0.05 mm/mm; extension rate: 1mm/min, (Unit Conversion: 1 ksi = 6.9 MPa; 36 ksi = 248.2 MPa; 1 in = 25.4 mm)

Table 10: Aroostook bridge (ME) Tensile Test Results

	Yield Stress (MPa)	Yield Strain (mm/mm)	Ultimate Tensile Stress (MPa)	Ultimate Tensile Strain (mm/mm)	Break Point Stress (MPa)	Break Point Strain (mm/mm)	Young Modulus (GPa)
Extension rate: 1mm/min							
Specimen 1	244.7	0.00119	391.3	0.2105	335.2	0.3051	205.6
Specimen 2	248.1	0.0012	390.9	0.2097	326.5	0.3049	206.7
Specimen 2	242.9	0.00118	402.1	0.2215	299.3	0.3304	205.8
Mean	245.2[a] ± 6.55[b]	0.00119[a] ± 0.0000248[b]	394.7[a] ± 15.78[b]	0.2139[a] ± 0.0163[b]	320.3[a] ± 46.5[b]	0.313[a] ± 0.0364[b]	206.1[a] ± 1.456[b]
Standard Deviation (SD)	2.64	1E-05	6.35	0.00659	18.7	0.015	0.59

[a]Mean from 3 samples; [b] 95% Confidence interval (CI)

3.1.4.2 *Extension Rate: 4 mm/min*

Three specimens from the Aroostook bridge were tested at the extension rate of 4mm/min. Extensions and the corresponding forces required to cause the extensions were recorded at the frequency of 2 Hz. Engineering stress-strain diagram are plotted as shown in Figure 52 and 53. Arr_Sp4, Arr_Sp5 and Arr_Sp6 represent specimens 4, 5, and 6, respectively, fabricated from the collected Aroostook Bridge materials. The results are presented in terms of yield strength, yield strain, ultimate tensile strength, ultimate tensile strain, breaking point strength, and breaking point strain. Result statistics from the tested specimens are presented in terms of mean, standard deviation and the 95% confidence interval out of two samples since the failure point for specimen 1 lies outside the gauge length. The result shows a mean yield strength of 245 MPa with Standard Deviation (SD) of 1.15 MPa at 95% Confidence Interval (CI) of 2.86 MPa. Similarly, an ultimate tensile strength of 388 MPa was obtained, with SD of 4.87 MPa at 95% CI of 12.1 MPa. Further information on breaking strength, yield strain, ultimate tensile strain, and breaking strain can be found in Table 11.

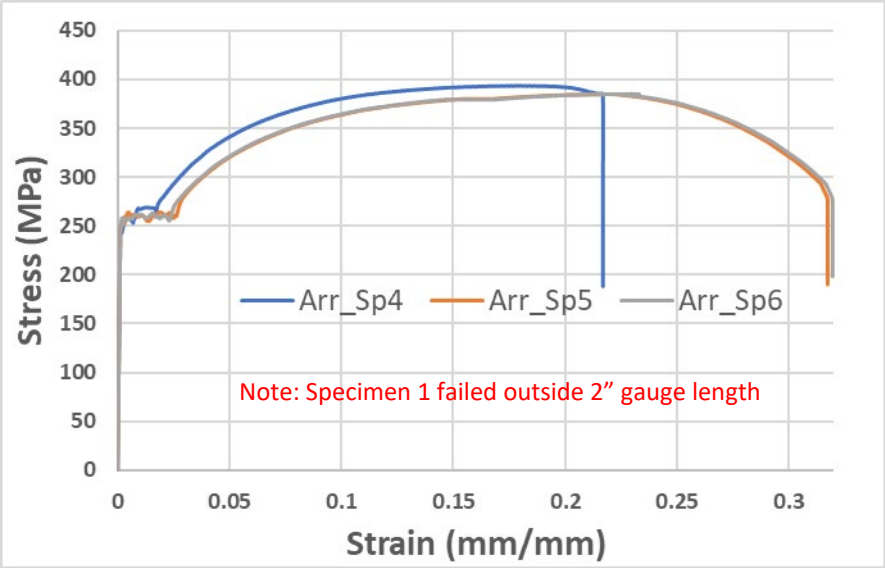

Figure 53: Tensile Stress-strain diagram, Aroostook bridge, Maine; monotonic loading to failure; extension rate: 4mm/min. (Unit Conversion: 1 ksi = 6.9 MPa; 36 ksi = 248.2 MPa; 1 in = 25.4 mm)

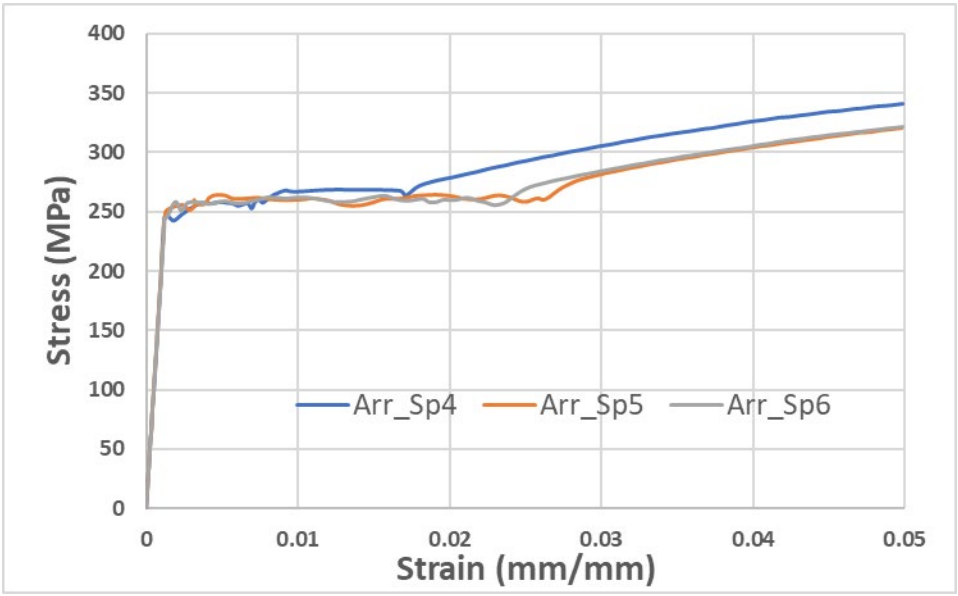

Figure 54: Tensile Stress-strain diagram, Aroostook bridge, Maine enlarged scale up to strain 0.05 mm/mm; extension rate: 4mm/min, (Unit Conversion: 1 ksi = 6.9 MPa; 36 ksi = 248.2 MPa; 1 in = 25.4 mm)

Table 11: Aroostook bridge (ME) Tensile Test Results

	Yield Stress (MPa)	Yield Strain (mm/mm)	Ultimate Tensile Stress (MPa)	Ultimate Tensile Strain (mm/mm)	Break Point Stress (MPa)	Break Point Strain (mm/mm)	Young Modulus (GPa)
Extension rate: 4 mm/min							
Specimen 1	246.06	0.00121	393.6	0.196	343.2	0.264	203.4
Specimen 2	244.94	0.00119	385.2	0.205	334.9	0.317	205.8
Specimen 3	243.76	0.00120	385.2	0.209	329.1	0.319	203
Mean	$244.9^{a} \pm 2.86^{b}$	$0.00121^{a} \pm 0.0000379^{b}$	$388^{a} \pm 12.1^{b}$	$0.203^{a} \pm 0.0165^{b}$	$335.7^{a} \pm 17.6^{b}$	$0.3^{a} \pm 0.077^{b}$	$201.6^{a} \pm 3.79^{b}$
Standard Deviation (SD)	1.15	0.0000153	4.87	0.0066	7.1	0.031	1.53

[a]Mean from 3 samples; [b] 95% Confidence interval (CI)

3.1.4.3 *Extension Rate 100 mm/min*

Three specimens from the Aroostook bridge were tested at the extension rate of 100 mm/min. Extensions and the corresponding forces required to cause the extensions were recorded at the frequency of 2 Hz. Engineering stress-strain diagram are plotted shown in Figures 55 and 56. Arr_Sp7, Arr_Sp8 and Arr_Sp9 represent specimens 7, 8, and 9, respectively, fabricated from the collected Aroostook Bridge materials. The results are presented in terms of yield strength, yield strain, ultimate tensile strength, ultimate tensile strain, breaking point strength, and breaking point strain. Result statistics from the tested specimens are presented in terms of mean, standard deviation and the 95% confidence interval out of two samples since the failure point for specimen 1 lies outside the gauge length. The result shows a mean yield strength of 275 MPa with Standard Deviation (SD) of 5.9 MPa at 95% Confidence Interval (CI) of 14.7 MPa. Similarly, an ultimate tensile strength of 410 MPa was obtained with SD of 4.39 MPa at 95% CI of 10.89 MPa. Further information on breaking strength, yield strain, ultimate tensile strain, and breaking strain can be found in Table 12.

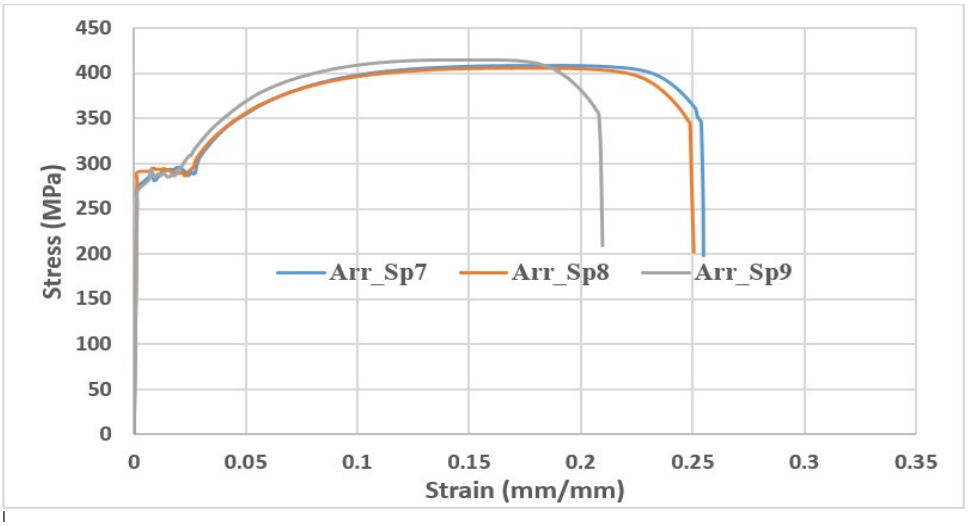

Figure 55: Tensile Stress-strain diagram, Aroostook bridge, Maine; monotonic loading to failure; extension rate: 100 mm/min. (Unit Conversion: 1 ksi = 6.9 MPa; 36 ksi = 248.2 MPa; 1 in = 25.4 mm)

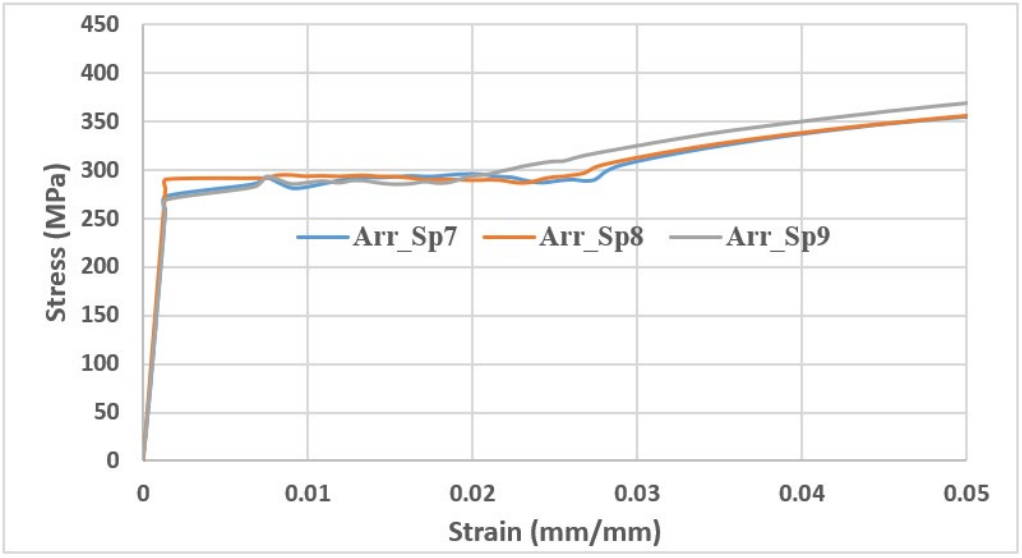

Figure 56: Tensile Stress-strain diagram, Aroostook bridge, Maine enlarged scale up to strain 0.05 mm/mm; extension rate: 100mm/min, (Unit Conversion: 1 ksi = 6.9 MPa; 36 ksi = 248.2 MPa; 1 in = 25.4 mm)

Table 12: Aroostook bridge (ME) Tensile Test Results

	Yield Stress (MPa)	Yield Strain (mm/mm)	Ultimate Tensile Stress (MPa)	Ultimate Tensile Strain (mm/mm)	Break Point Stress (MPa)	Break Point Strain (mm/mm)	Young Modulus (GPa)
Extension rate: 100 mm/min							
Specimen 7	273.11	0.001299	408.6	0.191	198.36	0.255	210.3
Specimen 8	280.89	0.001323	405.8	0.201	201.99	0.251	212.4
Specimen 9	269.31	0.001301	414.4	0.172	209.11	0.201	207.1
Mean	274.4[a] ± 14.7[b]	0.00131[a] ± 0.0000331[b]	409.6[a] ± 10.89[b]	0.188[a] ± 0.037[b]	347.7[a] ± 14.47[b]	0.236[a] ± 0.074[b]	209.9[a] ± 6.63[b]
Standard Deviation (SD)	5.9	0.0000133	4.39	0.015	5.82	0.03	2.66

[a]Mean from 3 samples; [b] 95% Confidence interval (CI)

3.1.4.4 *Extension Rate: 500 mm/min*

Three specimens from the Aroostook Bridge were tested at the extension rate of 500 mm/min. Extensions and the corresponding forces required to cause the extensions were recorded at the frequency of 2 Hz. Due to the limitation of dial indicator, the extension data could not be collected accurately. This extension rate is high such that the specimen breaks at the very short time, so it is necessary to collect data at higher sampling frequency in order to get accurate stress-strain curve. However, we found that data collected at higher sampling frequency using dial indicator are not precise enough to get accurate stress strain curve. So, we use the extension data recorded by the machine itself. Stress-extension diagram are plotted as shown in Figures 57 and 58. Arr_Sp10, Arr_Sp11 and Arr_Sp12 represent specimens 10, 11, and 12, respectively, fabricated from the collected Aroostook Bridge materials. The results are presented in terms of yield strength, ultimate tensile strength, and breaking point strength. Result statistics from the tested specimens are presented in terms of mean, standard deviation and the 95% confidence interval. The result shows a mean yield strength of 307 MPa with Standard Deviation (SD) of 5.7 MPa at 95% Confidence Interval (CI) of 14.3 MPa. Similarly, an ultimate tensile strength of 417 MPa was obtained, with SD of 6.74 MPa at 95% CI of 16.74 MPa. This information is presented in Table 13.

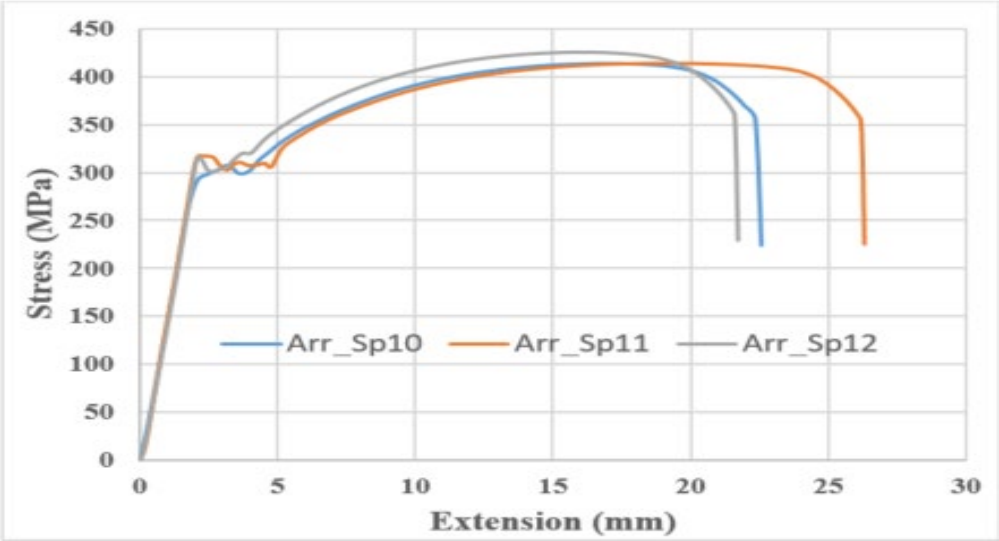

Figure 57: Tensile Stress-strain diagram, Aroostook bridge, Maine; monotonic loading to failure; extension rate: 500 mm/min. Note: Horizontal axis is extension as opposed to strain (Unit Conversion: 1 ksi = 6.9 MPa; 36 ksi = 248.2 MPa; 1 in = 25.4 mm)

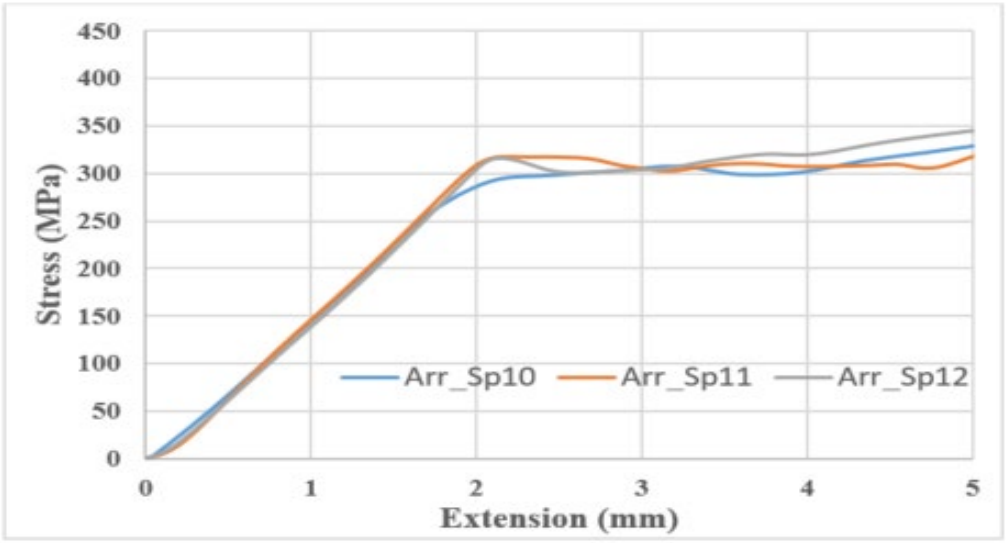

Figure 58: Tensile Stress-strain diagram, Aroostook bridge, enlarged scale up to strain 0.05 mm/mm; extension rate: 500mm/min. Note: Horizontal axis is extension as opposed to strain (Unit Conversion: 1 ksi = 6.9 MPa; 36 ksi = 248.2 MPa; 1 in = 25.4 mm)

Table 13: Aroostook Bridge (ME) Tensile Test Results

	Yield Stress (MPa)	Ultimate Tensile Stress (MPa)	Break Point Stress (MPa)
Extension rate: 500 mm/min			
Specimen 10	301.1	413.2	224.5
Specimen 11	311.8	414.1	229.3
Specimen 12	310.2	425.3	225.1
Mean	307.7[a] ± 14.33[b]	417.53[a] ± 16.74[b]	354.53[a] ± 10.28[b]
Standard Deviation (SD)	5.77	6.74	4.14

[a]Mean from 3 samples; [b] 95% Confidence interval (CI)

Note: Corresponding strains are not available for this extension rate because the dial indicator used to record the extension is not capable of capturing the data accurately at such high rate.

3.1.4.5 *Extension Rate Effect on Tensile Properties*

From the experiments, it is observed that the yield strength increases slightly with increase in extension rate, but this is more significant in the higher extension rates (8 mm/min, 100 mm/min and 500 mm/min) since the yield strength remains almost unaltered at low extension rates (1mm/min and 4 mm/min) as presented in Figure 59. The ultimate tensile strength also increases with increases in extension rate, but this effect also is more significant when the extension rates are higher. It is observed that the ultimate tensile strength value decreases slightly for 4 mm/min as presented in Figure 60. The breaking point strength remains almost the same for all extension rates except for 8 mm/min (decreases slightly in this case) as presented in Figure 61.

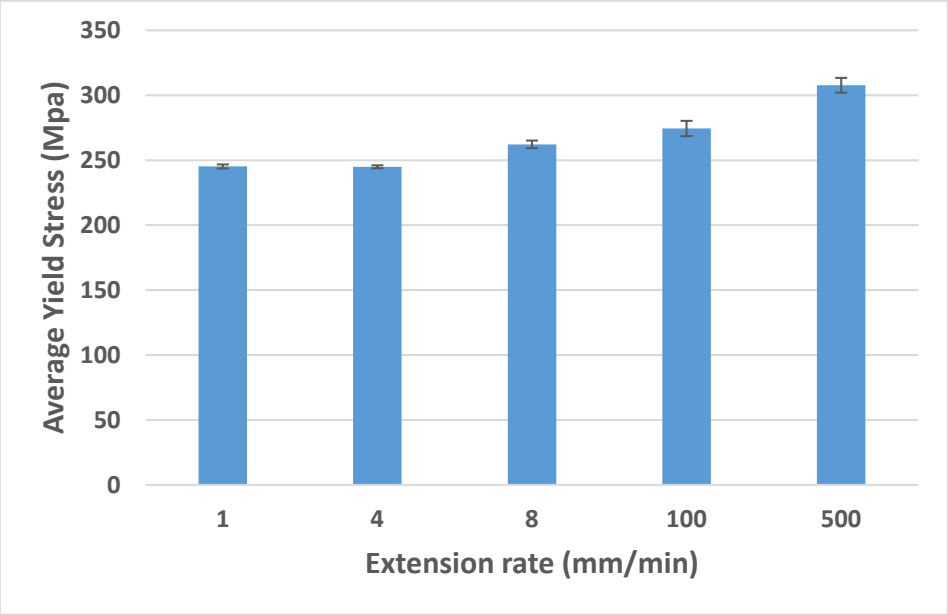

Figure 59: Effect of extension rate on Yield Strength

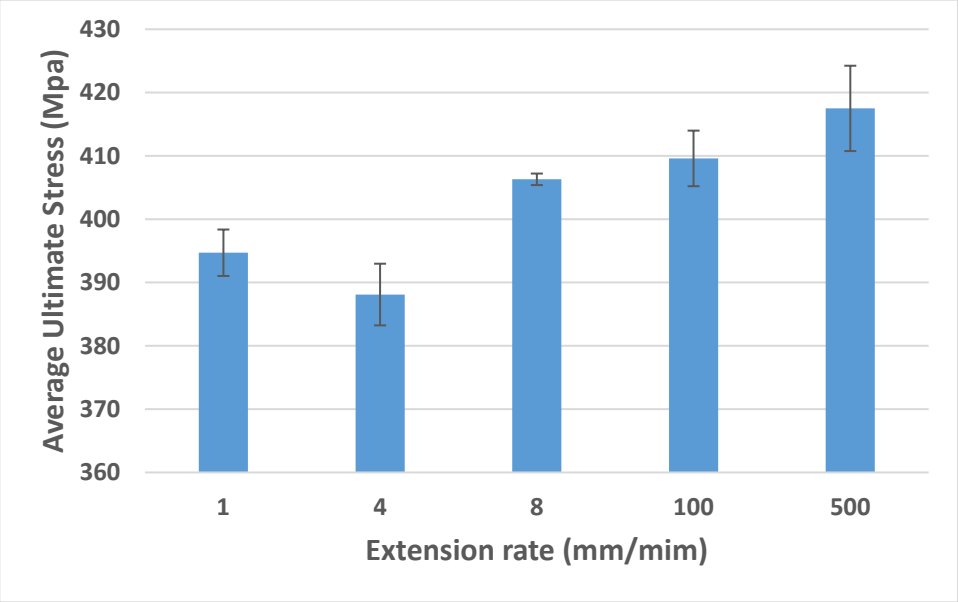

Figure 60: Effect of extension rate on Ultimate Tensile Strength

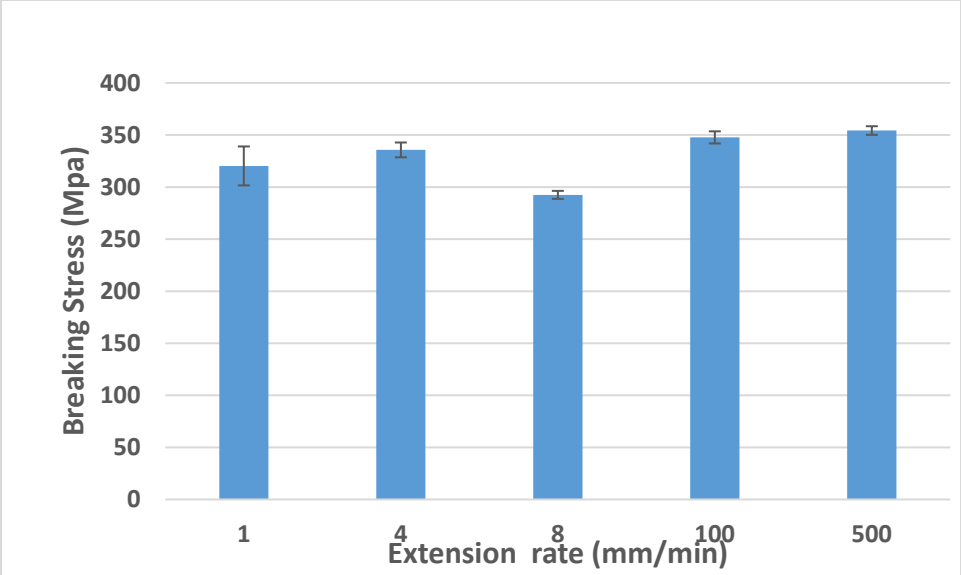

Figure 61: Effect of extension rate on Breaking Strength

3.2 Field Test Results

Data were collected using the LDV in conjunction with the Polytec PSV software and scaled using the instrument sensitivity factor. Then, data were processed using an in-house code written in MATLAB, which is based on the concepts of structural dynamics presented in this report. Velocity and acceleration time variation has been obtained from the field tests using LDV and accelerometers, respectively. Furthermore, the raw data from the field test has been processed and converted to relevant structural dynamic responses, such as displacement time variation and response spectrum.

3.2.1 Devon Bridge

The Devon bridge field test data, shown in appendix A, were first processed and analyzed in the time domain to extract the dynamic response of the bridge, and then analyzed in the frequency domain to update and validate the computational model.

Displacement and acceleration results obtained from the FE model for different members of the bridge due to traversing of the train load were compared against those obtained in the field test using reference accelerometers. The forcing frequency was compared with the theoretical axle frequency in the frequency domain. Finally, the natural bridge frequency was estimated using FFTs under free vibration and compared with the FE model.

3.2.1.1 *Bridge Structural Responses*

The first step in processing LDV field test data is to estimate the vehicle traveling speed. Based on the Metro-North specifications, the passenger train traveling speed on the Devon bridge is limited to 45 mph (72.42 km/h). The period of the typical car can be estimated using a pick-and-choose method by selecting a constant location of the wave crest or valley and finding the difference. For example, Figure 60 show the displacement. Knowing a typical car's dimensions, for example, 85 feet (25.90 m) for the MTNR M8, the traveling speed can be found by dividing by the axle period of the typical car length. The axle period can be estimated using the pick-and-choose method from the displacement-time variation plots. For example, the estimated average vehicle traveling speed for Train 7 in the westward direction is around 42 mph (67.60 km/h), as shown in the Figure 62. Similarly, the only recorded train traveling eastward is Train 10, which was estimated to be traveling at approximately 18 mph (28.97 km/h) as shown in the figure below.

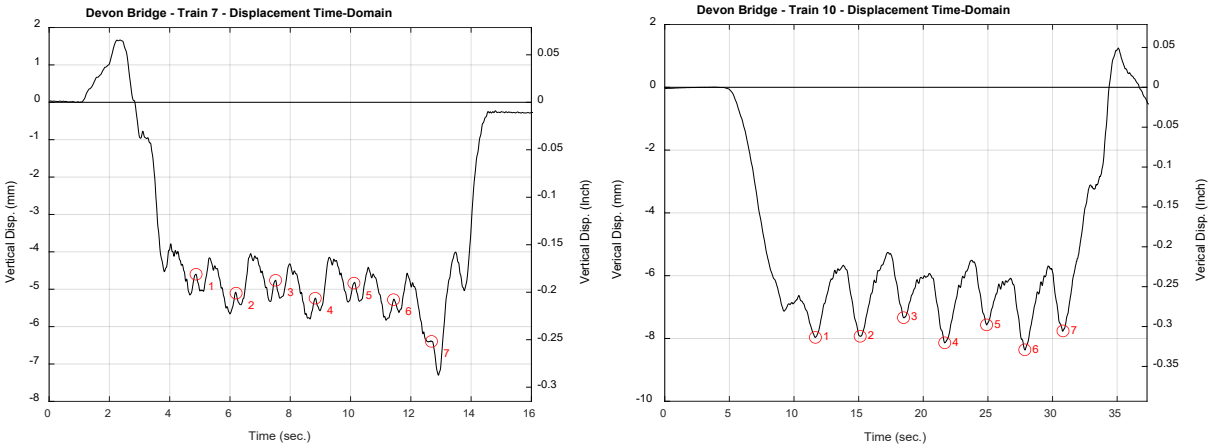

Figure 62: Devon bridge: Displacement-time variation used to estimate traveling speed, (a) Train 7 and (b) Train 10

Using the displacement-time plots recorded from different locations on the bridge during the field test, we can identify the maximum and minimum vertical displacement. Similarly, the load behavior and axle configuration can be visualized. Figure 63 shows the displacement-time plots of Train 3 at the node L13, and Train 5 at the middle of the floor beam L6 location (see Figure 34 for node number reference). All trains travel in the westward (east to west) direction. The Train 3 is a typical AMTK Regional with seven coaches with a power engine, traveling at 43.13 mph (69.41 km/h). Train 5 is a typical AMTK Acela composition, traveling at 42.57 mph (68.50 km/h). Uplift was observed in all readings at the abutment side of span 7. The observed uplift is a sign of the abnormal condition that the bridge might have been experiencing. Therefore, future studies should explore this phenomenon in greater detail.

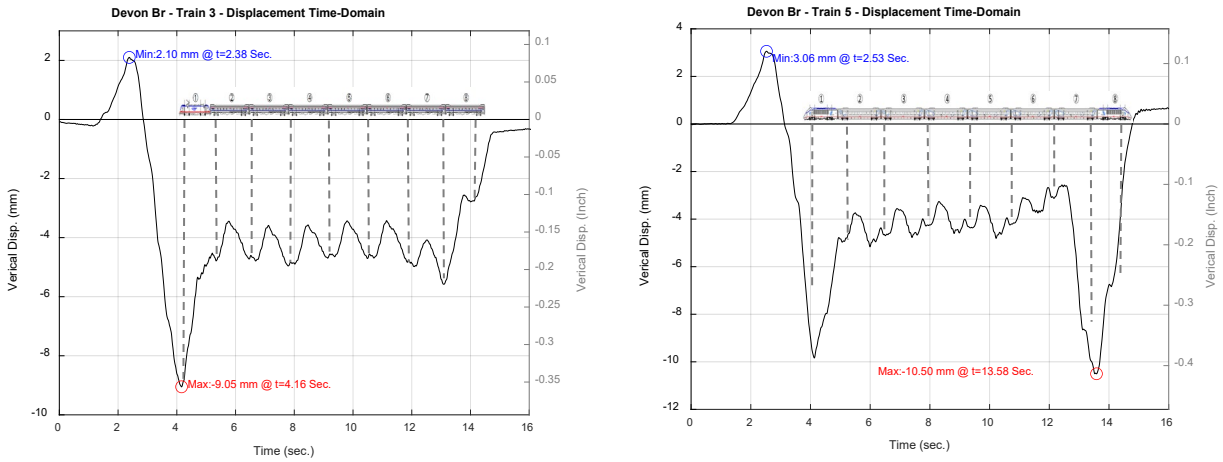

Figure 63: Vertical displacement-time plots on Devon bridge: (a) Train 3, and (b) Train 5

The table below shows the vertical displacement time variation of the LDV recorded from seven trains that passed through the Devon bridge span 7 of the south bridge, either on track no. 2 or 4.

Table 14: Devon bridge: Summary results of time domain parameters of relevant trains using LDV

Train	Travel Direction	Track	Car	Train Type	LDV Loc	Travel Speed	Max. Vertical Displacement	Uplift
1	East-West	4	9	MTNR M8	1 (Node)	42.38 mph (68.20 km/h)	-0.30 in (-7.67 mm)	0.03 in (0.84 mm)
3	East-West	4	8	AMTK Regional	2 (Node)	43.13 mph (69.41 km/h)	-0.35 in (-9.05 mm)	0.08 in (2.10 mm)
4	East-West	4	11	MTNR M8	2 (Node)	41.90 mph (67.43 km/h)	-0.26 in (-6.70 mm)	0.04 in (1.24 mm)
5	East-West	2	8	AMTK Acela	3 (Floor beam)	42.57 mph (68.50 km/h)	-0.41 in (-10.5 mm)	0.12 in (3.06 mm)
7	East-West	4	8	AMTK Regional	3 (Floor beam)	41.93 mph (67.48 km/h)	-0.28 in (-7.27 mm)	0.06 in (1.70 mm)
10	West-East	2	8	MTNR M8	4 (Floor beam)	17.89 mph (28.79 km/h)	-0.30 in (-7.83 mm)	0.07 in (1.78 mm)
11	East-West	4	8	AMTK Regional	5 (Floor beam)	41.28 mph (66.43 km/h)	-0.65 in (-16.6 mm)	0.17 in (4.37 mm)

Figure 64 shows an acceleration comparison between the derived vertical velocity from LDV and the vertical and horizontal acceleration readings from ACC 1 and ACC 2, respectively. Again, since the ACC 1 and LDV 2 readings are from the same node, the node L12, the results show good agreement.

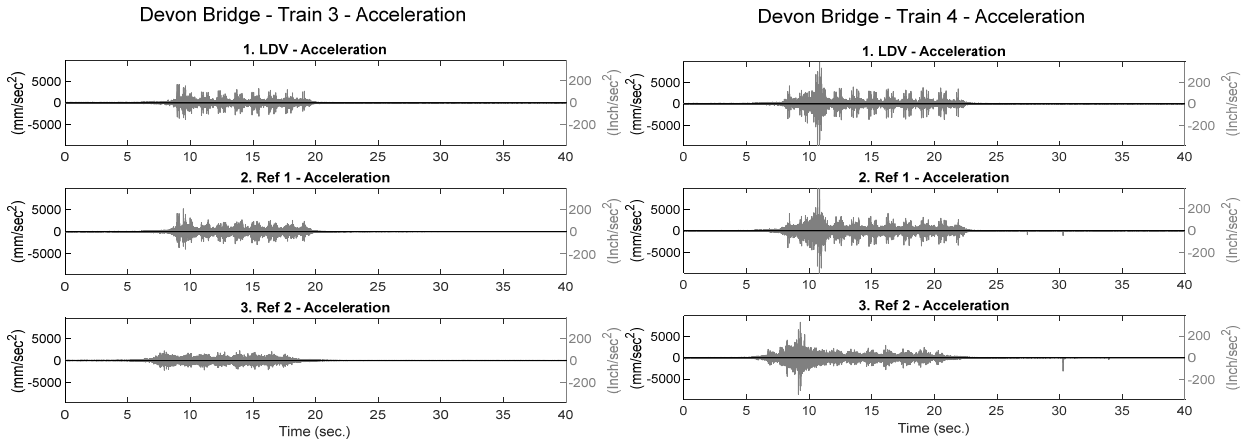

Figure 64: Devon bridge: Acceleration comparison between LDV and accelerometers, (a) Train 3, (b) Train 4

The AREMA high-speed rail Structures task force and other international high-speed design codes have recommended maximum bridge acceleration limits based on the type of the bridge (AREMA, 2017). Therefore, the acceleration can be compared using a maximum peak value or the RMS value, using bandwidth and filter specifications defined in different design codes. However, the filtering and cut-off frequency can severely affect the maximum peak value obtained from the accelerometers. Therefore, often the RMS offers a better parameter for comparing acceleration values. For example, in the current 49 CFR Part 213 Subpart G, the Federal Rail Administration recommends the maximum RMS vertical and lateral acceleration value for passenger comfort measured at the train body and truck (CFR, 2022).

Table 15 shows the summary comparison of the acceleration RMS from the LDV and accelerometer references of Train 3 and Train 4. Since Train 3 and Train 4 were recorded directly above ACC 1, a vertical accelerometer, they can be correlated in magnitude using an RMS.

Table 15: Devon bridge: RMS of acceleration comparison from LDV and accelerometers

Instrument	Direction	RMS Acceleration – Train 3			RMS Acceleration – Train 4		
		mm/sec²	in/sec²	g's	mm/sec²	in/sec²	g's
LDV 2	Vertical	504.0	19.8	0.05	722.1	28.4	0.07
ACC 1	Vertical	520.3	20.4	0.05	720.3	28.3	0.07
ACC 2	Horizontal	406.2	15.9	0.04	637.1	25.0	0.06

3.2.1.2 *Structural Frequency Responses*

Any data collected in the time domain can be converted to the frequency domain to extract spectrum parameters. Since the frequency in Hertz (Hz) is the inverse of the period, we can calculate the frequency (f_a) using the period to estimate the train traveling speed in time-domain analysis and frequency *n* integers, as presented in the methodology section (section 2.1). On the other hand, the only requirements for calculating the operation frequency (f_a) are the bridge span length of 217'-4" (66.24 m) and the traveling speed of the respective trains.

Figure 65 shows the spectral response of the LDV data from 0 to 10 Hz; the operation and the axle frequencies were identified and marked accordingly.

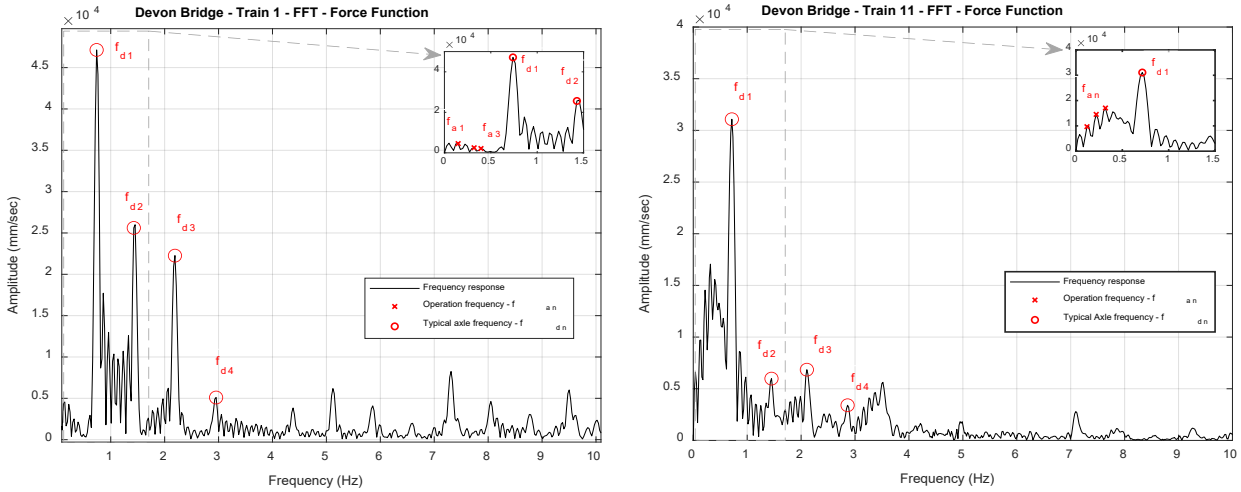

Figure 65: Devon bridge: FFT of the forced vibration part, (a) Train 1, (b) Train 11

The data exhibit a slight divergence from the analytical values, mainly due to the model assumptions such as constant traveling speed, axle centroids, and spectrum leakage. Table 16 shows a comparison between the recorded values and the theoretical values. The summary table below shows that the predominant forcing function frequency of the typical passenger train under service is 0 to 0.8 Hz if the maximum allowable traveling speed on the bridge is 45 mph (72.42 km/h).

Table 16: Devon bridge: Summary of the axle and operation frequency from the field test

Train	Travel Direc.	Train Type	LDV Loc.	Axle Frequency		Operation Frequency	
				LDV (Hz)	Theoretical (Hz)	LDV (Hz)	Theoretical (Hz)
1	East-West	MTNR M8	1	0.738 n^a	0.731 n^a	0.145 n^a	0.148 n^a
3	East-West	AMTK Regional	2	0.788 n^a	0.744 n^a	0.145 n^a	0.145 n^a
4	East-West	MTNR M8	2	0.741 n^a	0.723 n^a	0.109 n^a	0.141 n^a
5	East-West	AMTK Acela	3	0.328 n^a	0.357 n^a	0.141 n^a	0.144 n^a
7	East-West	AMTK Regional	3	0.767 n^a	0.724 n^a	0.139 n^a	0.141 n^a
10	West-East	MTNR M8	4	0.313 n^a	0.309 n^a	0.063 n^a	0.060 n^a
11	East-West	AMTK Regional	5	0.742 n^a	0.710 n^a	0.119 n^a	0.139 n^a

[a] The *n*-value is the integer from the frequencies defined in the Methodology section.

The natural frequencies of the bridge were estimated using the free vibration part of the data (Norén-Cosgriff and Kaynia, 2021), in this case, after the last car leaves the bridge span. For this study, the data collected after the train passed the opposite bridge i.e., the north bridge, was used in conjunction with the other data recorded when the train passed the bridge under study i.e., south bridge.

The time-domain data were converted into frequency-domain data using the FFT and PSD methods described in the preceding chapter. The FFT and PSD plots of the bridge response due to traversing of trains under free vibration are presented in figure 66. These plots can be used to estimate the bridge span natural frequencies.

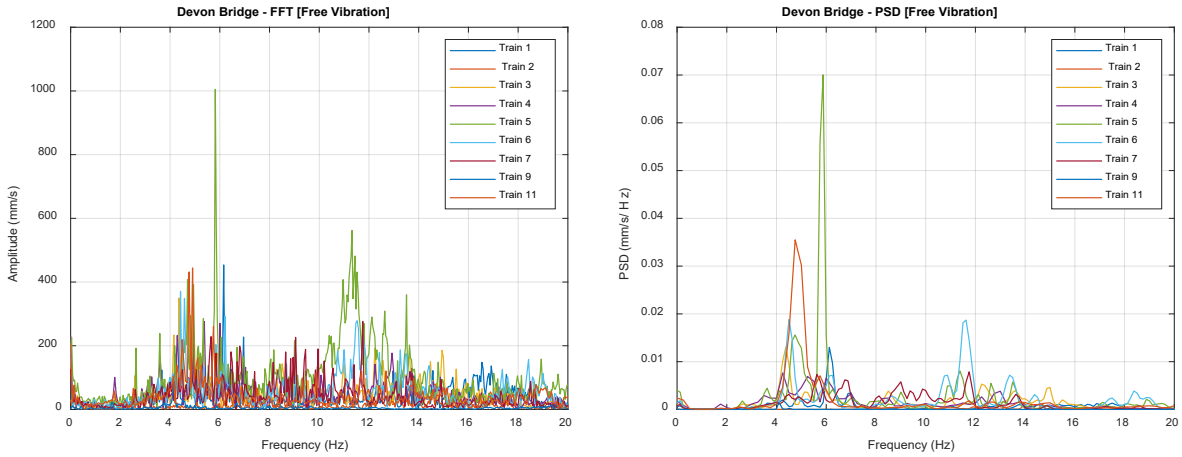

Figure 66: Devon bridge: Frequency study under free vibration, (a) FFT, (b) PSD

Table 17 summarizes the identified peaks (natural frequencies) obtained from the field test of Devon bridge.

Table 17: Devon bridge: Summary of the estimated bridge span natural frequencies

ID	Natural frequency using free vibration part of the data (Hz)									Mean Freq. (Hz)
	Train 1	Train 2	Train 3	Train 4	Train 5	Train 6	Train 7	Train 9	Train 11	
1	1.786	1.916	1.812	1.773	*	*	1.769	1.672	1.752	1.783
2	*	2.540	2.594	*	2.663	*	2.560	2.453	2.523	2.556
3	3.666	*	*	3.604	3.587	3.526	*	*	*	3.596
4	*	*	4.150	[a]	4.185	4.105	4.097	4.078	4.134	4.125
5	4.230	4.277	4.357	4.291	4.703	4.578	4.516	4.547	4.765	4.474
6	4.935	5.079	5.136	4.920	4.942	5.210	4.842	*	4.905	4.996
7	6.157	6.193	*	6.007	5.819	*	5.586	5.875	*	5.940

* Bridge's natural frequency was not identified.

Also, the accelerometers results were compared against the LDV results in the frequency domain. Since the accelerometers were attached in fixed locations described in the field test methodology section, the estimated vibration modes do not change significantly. Figure 67 shows the frequency domain analysis of the accelerometer's references from Train 11. The accelerometers were designated as ACC 1 and ACC 2, per the schematic drawing presented in Figure 17 and Figure A-1, and installed in vertical and horizontal positions, respectively.

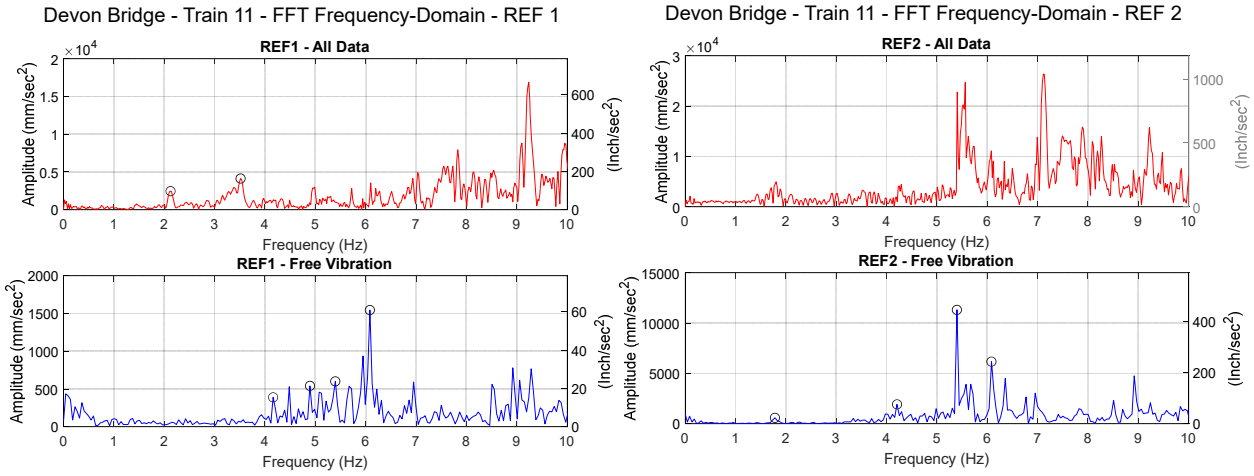

Figure 67: Devon bridge: Accelerometers in FFT frequency analysis Train 11: (a) ACC 1, and (b) ACC 2

Tables 18 and 19 show the identified frequencies using the peak-picking method from FFT plots from figure 67 (Norén-Cosgriff and Kaynia, 2021)
. From the FFT plot (Figure 67) and the tables below (Tables 18 and 19), it is possible to determine the first few natural frequencies of the bridge in horizontal and vertical directions. In addition, the accelerometers show a poor resolution for lower frequencies, below 1 Hz, as observed on all data where the primary vibration frequency is around 0.7 Hz and has not been shown in the FFT plots.

Table 18: Devon bridge: Accelerometers FFT under Free vibration

FFT Peak	Description	ACC 1	ACC 2
		Free Vibration (Hz)	
1	1st Lateral	*	1.784
2	2nd Lateral	4.162	4.208
3	1st Vertical	4.894	*
4	2nd Torsion	5.398	5.398
5	1st Twist	6.084	6.084

* Bridge's natural frequency was not identified.

Table 19: Devon bridge: Accelerometers FFT under all vibration data

FFT Peak	Description	ACC 1	ACC 2
		All Data (Hz)	
1	3rd Axle frequency (*n=3*) [a]	2.126	[b]
2	5th Axle frequency (*n=5*) [a]	3.517	[b]

[a] the *n*-value is the integer from the frequencies defined in the Methodology section.
[b] Forced frequency was not identified.

Table 19 was compiled using the FFT data from Figure 67, upper plot (all data). The axle frequency is defined on the methodology section (section 2.1).

3.2.2 Cos Cob Bridge

The velocity-time signals collected using Laser Doppler Vibrometer (LDV) under the service loading of trains used in this study as described in section 2.4.3 contains both the forced vibration response and the free vibration response (as shown in the Figure B-1 to B-9 in Appendix). The force vibration responses were processed and analyzed to determine the nodal displacement of the bridge span under the service loading. The free vibration responses were processed and analyzed to determine the natural frequency of the bridge. Free vibration responses are commonly used to estimate the dynamic properties of railroad bridges since they provide sufficiently energetic and pure responses while the bridge responses under forced vibration contain combined interaction between vehicle and bridge. Thus, the bridge responses are non-stationary and difficult to analyze (Cantero et al., 2016). The acceleration-time signals collected using accelerometers were also processed and analyzed in the frequency domain to determine the natural frequencies of the bridge span using the free vibration response. Thus, obtained natural frequencies from the LDV and accelerometers are compared. The theory involved in this analysis are explained in chapter 2 of this report.

3.2.2.1 *Bridge Structural Response from LDV data*

The velocity-time signals collected at several nodes on the bridge were processed to determine the displacement-time histories at those nodes (represented by Vib. 1 to Vib. 11 in Figure 68, previously Figure 20, repeated here for readers convenience) using a trapezoidal numerical integration rule in MATLAB. The procedure involved in this process is presented in the methodology section. The nodal displacement-time histories due to bridge traversal by Metro North and Amtrak Regional trains are presented in the Figure 68-77 and summarized in the Table 20 below.

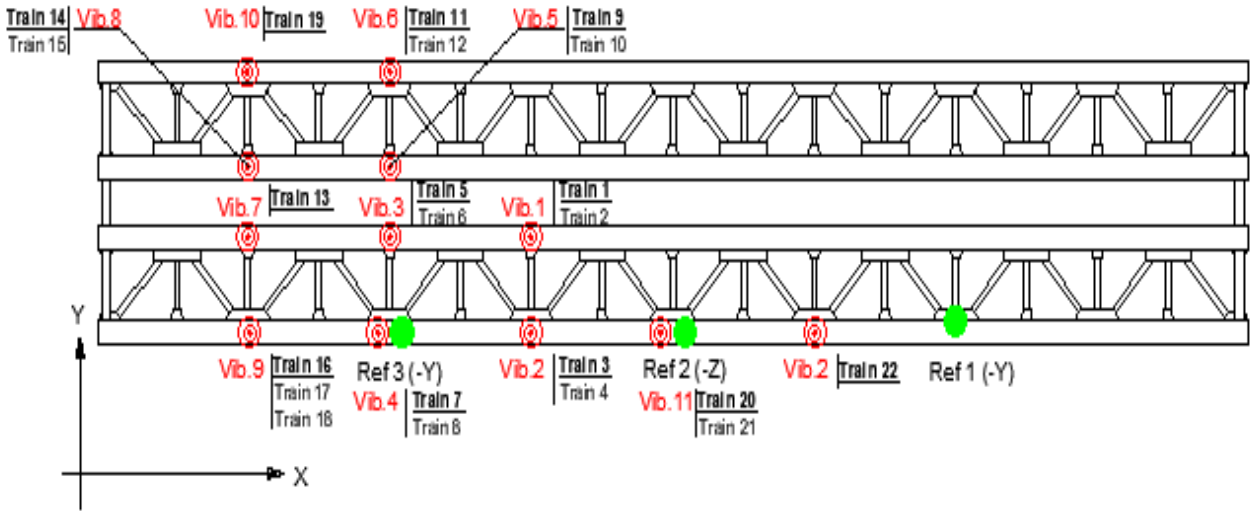

Figure 68: Cos Cob bridge plan view (Track 4 & Track 2); Vib. 1 to Vib. 11 representing nodes where the responses were collected using LDV and Ref 1, Ref 2 and Ref 3 representing nodes where reference accelerometers were attached

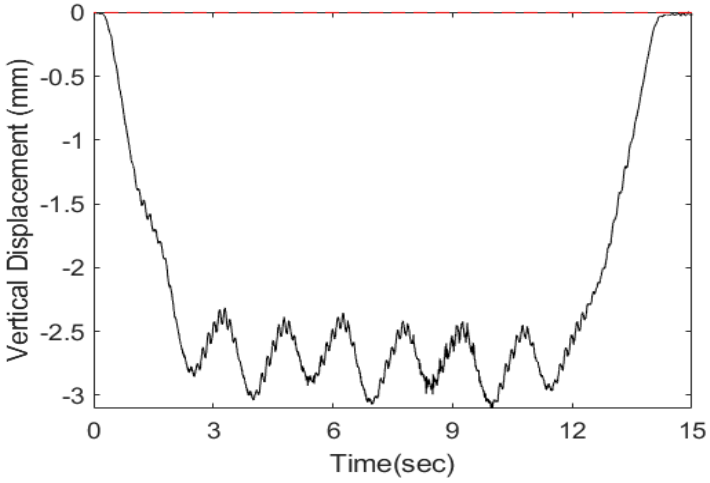

Figure 69: Vertical displacement vs. time at node Vib.1 (Figure 68) subjected to 8-car Metro North train moving at 34 mph from New York to New Haven on track 4 of Cos Cob bridge, CT. (Raw Data: Train2-Appendix B-1)

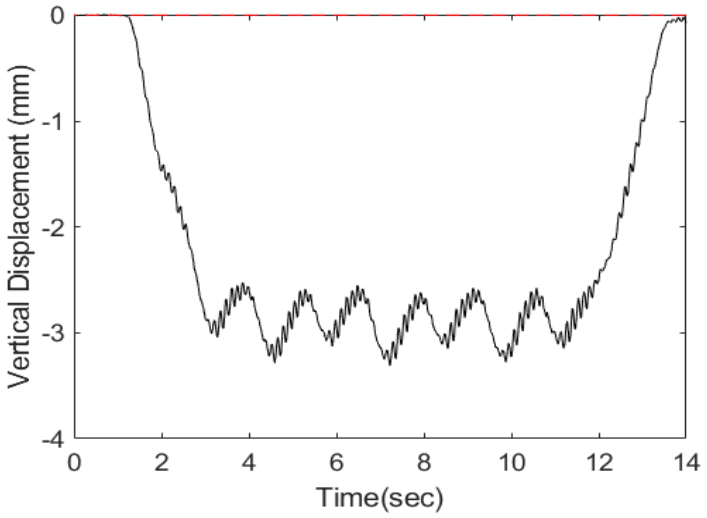

Figure 70: Vertical displacement vs. time at node Vib.2 (Figure 68) subjected to 8-car Metro North train moving at 17 mph from New York to New Haven on track 4 of Cos Cob bridge, CT. (Raw Data: Train 4-Appendix B-1)

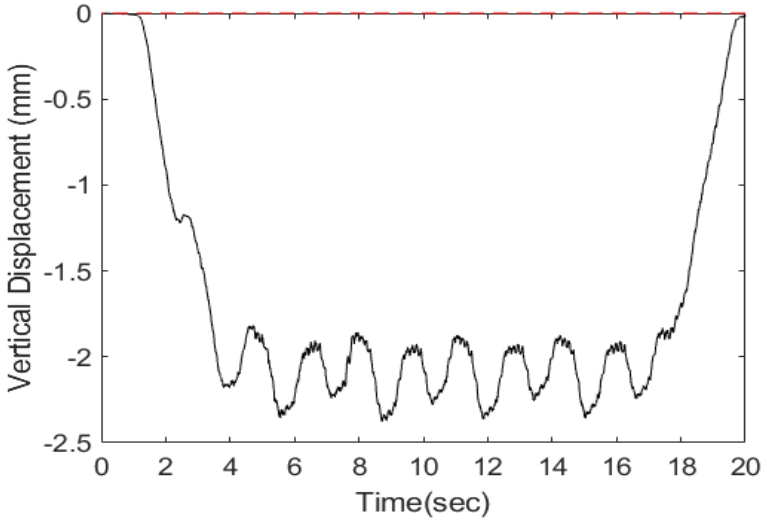

Figure 71: Vertical displacement vs. time at node Vib.3 (Figure 68) subjected to 8-car Metro North train moving at 14 mph from New York to New Haven on track 4 of Cos Cob bridge, CT. (Raw Data: Train 5-Appendix B-2)

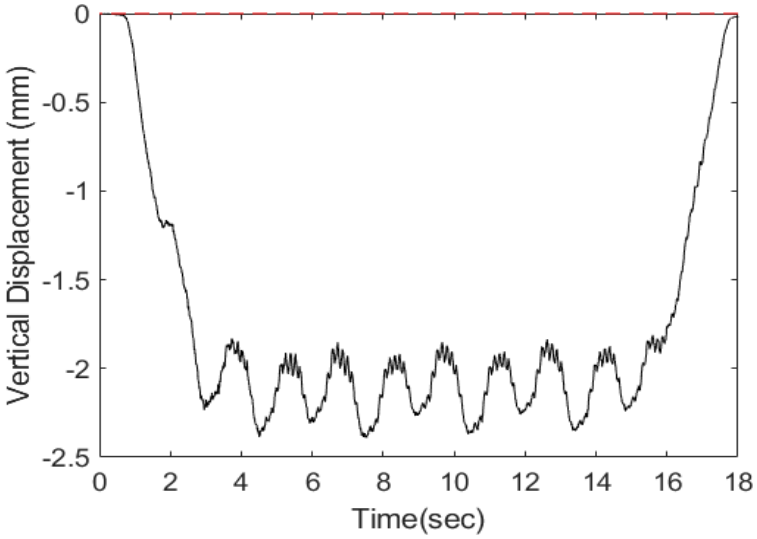

Figure 72: Vertical displacement vs. time at node Vib.3 (Figure 68) subjected to 8-car Metro North train moving at 21 mph from New York to New Haven on track 2 of Cos Cob bridge, CT. (Raw Data: Train 6-Appendix B-2)

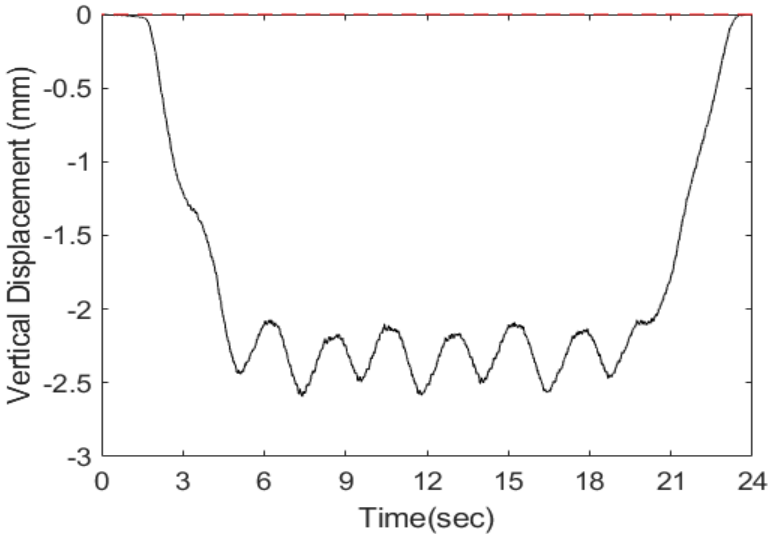

Figure 73: Vertical displacement vs. time at node Vib.4 (Figure 68) subjected to 8-car Metro North train moving at 16 mph from New York to New Haven on track 4 of Cos Cob bridge, CT. (Raw Data: Train 8-Appendix B-3)

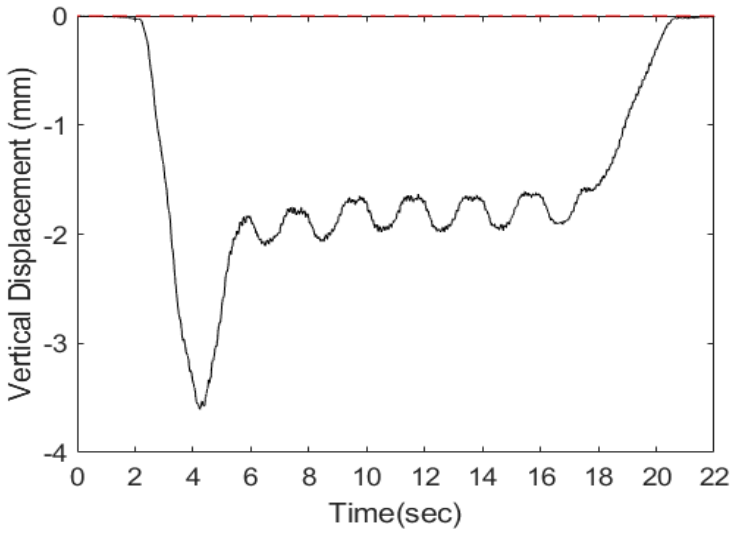

Figure 74: Vertical displacement vs. time at node Vib.5 (Figure 68) subjected to 8-car Amtrak Regional train moving at 14 mph from New York to New Haven on track 2 of Cos Cob bridge, CT. (Raw Data: Train 9 – Appendix B-3)

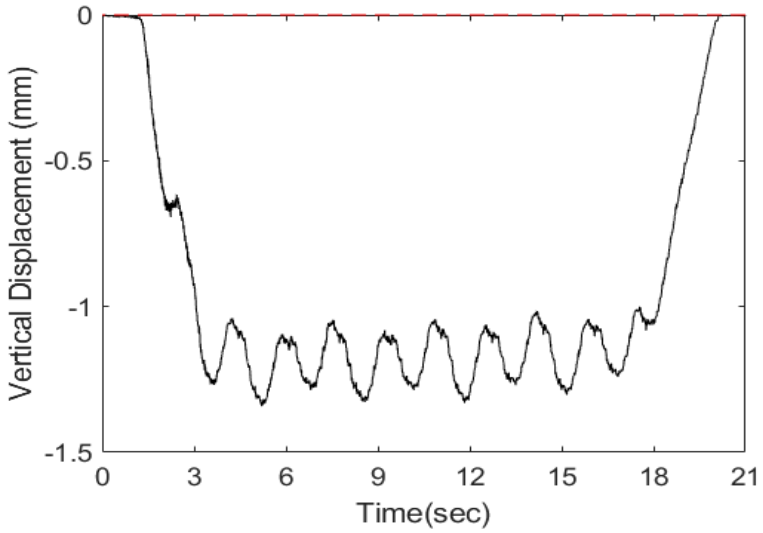

Figure 75: Vertical displacement vs. time at node Vib.7 (Figure 68) subjected to 10-car Metro North train moving at 13 mph from New York to New Haven on track 4 of Cos Cob bridge, CT. (Raw Data: Train 13-Appendix B-4)

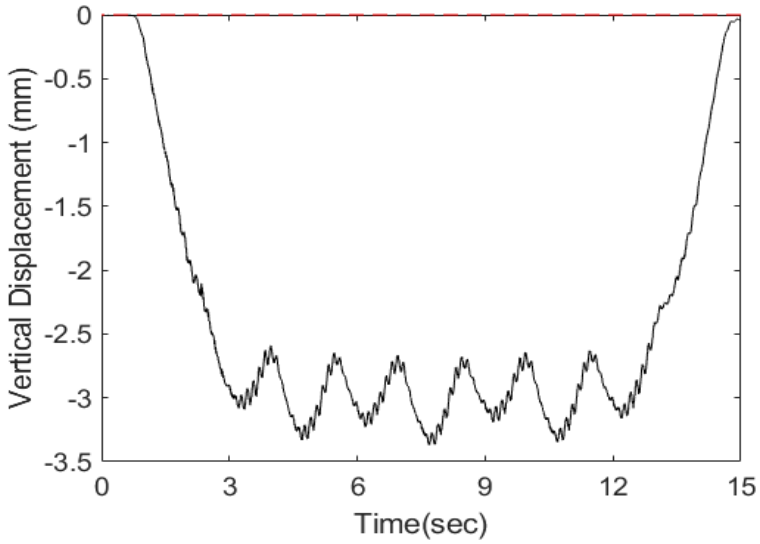

Figure 76: Vertical displacement vs. time at node Vib.11 (Figure 68) subjected to 8-car Metro North train moving at 31 mph from New York to New Haven on track 4 of Cos Cob bridge, CT. (Raw Data: Train 21-Appendix B-4)

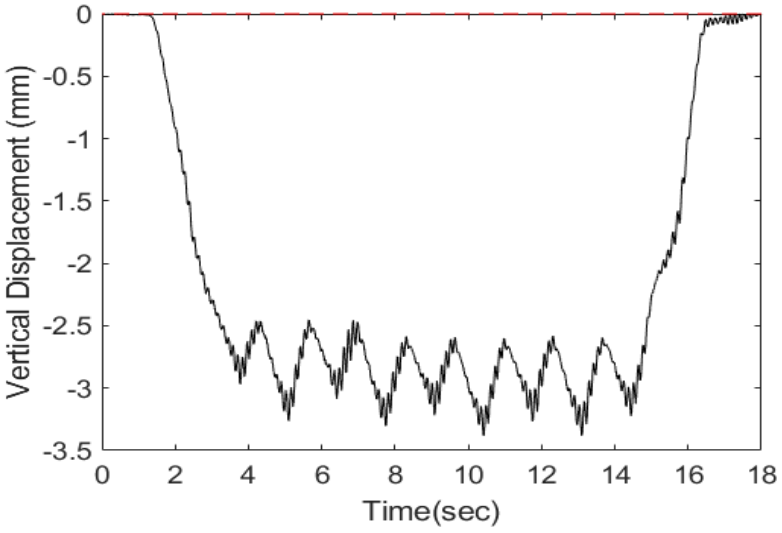

Figure 77: Vertical displacement vs. time at node Vib.12 (Figure 68) subjected to 10-car Metro North train moving at 37 mph from New York to New Haven on track 4 of Cos Cob bridge, CT. (Raw Data: Train 22-Appendix B-5)

From the plots presented in Figures 68-76, it is observed that the magnitude of the vertical displacement depends on the node where the bridge response is recorded. For the same train, vertical displacement is higher at the midpoint and decreases as we move towards the right and left ends of the bridge. The displacement is however independent of the number of cars in the train, as observed for train 5 and train 8. This is physically reasonable, because the fully loaded bridge can fit only one-and-a-half cars of the train.

Thus, the obtained nodal displacement-time histories can be helpful in classification of the train passing over the bridge. This is illustrated in the figure below, which represents the displacement-time history of the node Vib.11 when an 8-car Metro North train passes over the bridge span. It is observed that the number of valleys is one less than the number of cars in the Train. These valleys are produced by the combination of rear axle of one car and the front axle of another car. For example, in Figure 78, the loading from the front axle of first car displaces the node down to around 1.5 mm but as soon as the rear wheel of the first car and the front wheel of the second car hits the bridge, the valley appears. This trend continues until the rear wheel of seventh car and the front wheel of the eighth car hit the bridge resulting in the seventh valley. Eventually, the bridge span comes to rest after the rear axle from the eighth car hits and the train passes over the bridge. This can be noticed in other trains as well. So, by counting the number of valleys and the trend shown by the curve, one can easily distinguish the type and number of cars in the train. In case of Amtrak Acela, the first valley would be large in comparison to other

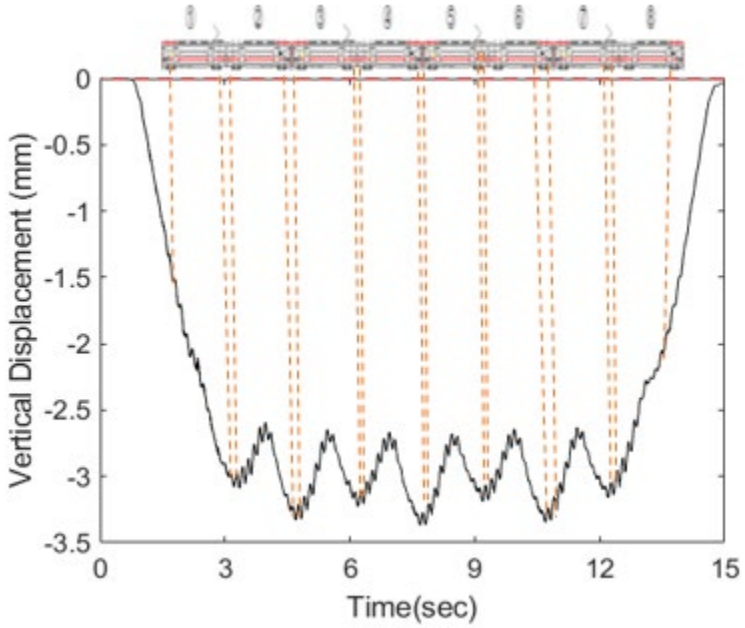

Figure 78: Typical displacement-time history with each peak and valleys representing axle configuration of M8 train when the train passes over the bridge at node Vib.11 (Figure 68)

valleys, as shown in Figure 74, due to the heavy load coming from the engine while the first and the last valley would be large in case of Amtrak Regional because of the heavy engine loading coming from these cars as seen in displacement results from the Devon Bridge.

Similarly, displacement-time history plot can be helpful in estimating the travelling speed of the train over the bridge as described in section 3.2.1.1.

Table 20 summarizes the relevant time-domain information from nine trains that passed over the Cos Cob bridge span, on track 2 or 4 during the field test.

Table 20: Cos Cob bridge: Time domain result summary using LDV

Train	Traveling Direction	Track	Cars	Train Type	Vib. Loc	Estimated Traveling Speed	Maximum Displacement
2	W-E	4	8	MTNR	1 (Node)	37.87 mph (60.94 km/h)	-0.122 in (-3.11 mm)
4	W-E	4	8	MTNR	2 (Node)	42.41 mph (68.23 km/h)	-0.131 in (-3.32 mm)
5	W-E	4	10	MTNR	3 (Node)	37.36 mph (60.12 km/h)	-0.094 in (-2.38 mm)
6	W-E	4	10	MTNR	4 (Node)	39.98 mph (64.34 km/h)	-0.094 in (-2.39 mm)
8	W-E	4	8	MTNR	3 (Node)	41.93 mph (67.48 km/h)	-0.103 in (-2.61 mm)
9	W-E	2	8	AMTK Regional	5 (Node)	28.07 mph (45.17 km/h)	-0.142 in (-3.61 mm)
13	W-E	4	10	MTNR	7 (Node)	36.32 mph (58.45 km/h)	-0.053 in (-1.34 mm)
21	W-E	4	8	MTNR	11 (Node)	37.85 mph (60.91 km/h)	-0.133 in (-3.38 mm)
22	W-E	4	10	MTNR	12 (Node)	45.15 mph (72.66 km/h)	-0.133 in (-3.39 mm)

Note: Direction: W-E represents New York to New Haven

3.2.2.2 *Bridge Frequency from LDV data*

From the free vibration response after the train passes the bridge, the natural frequencies of the Cos Cob Bridge were identified from the most recurring peaks of the PSD vs frequency curves.

The first as well as the second modes of the bridge were identified in the lateral direction at frequencies of 3.42 Hz and & 7.89 Hz, respectively (Figure 83). The first vertical mode of the bridge vibration was identified at frequency 7.54 Hz (Figure 86). Analysis of the free vibration response from several other trains shows the consistency in these recurring peaks as well. Identification of other higher modes and frequencies from the free vibration of the bridge at a particular train speed was not possible because the peaks were inconsistent at higher frequencies. See Figure 68 for train number and corresponding nodes where responses are recorded.

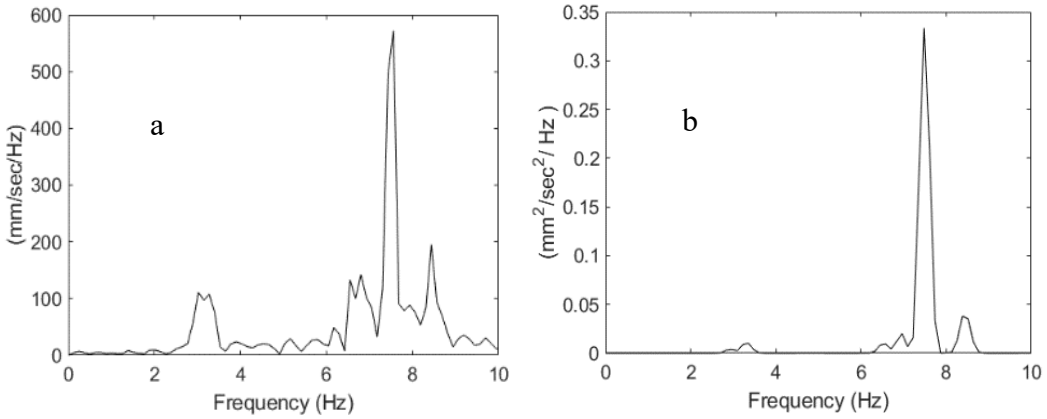

Figure 79: Lateral free vibration frequencies after passage of train 1 (Amtrak Acela) over the Cos Cob bridge (a) FFT and (b) PSD

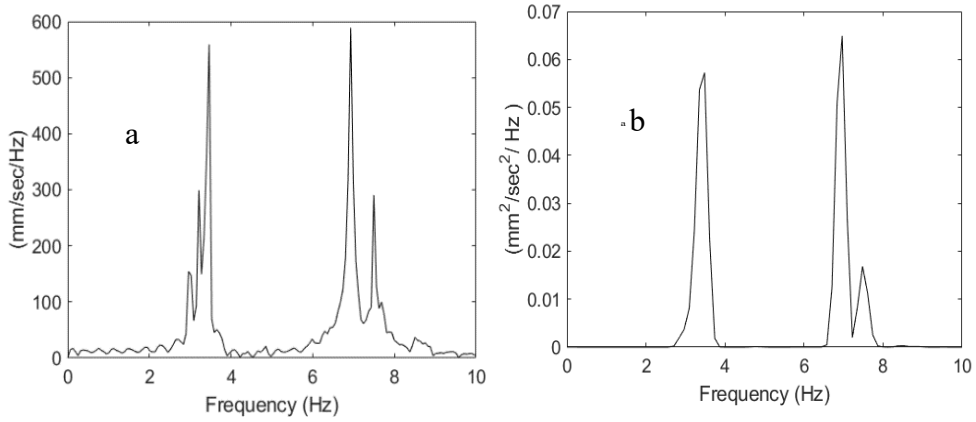

Figure 80: Lateral free vibration frequencies after passage of train 3 (Metro North) over the Cos Cob bridge (a) FFT and (b) PSD

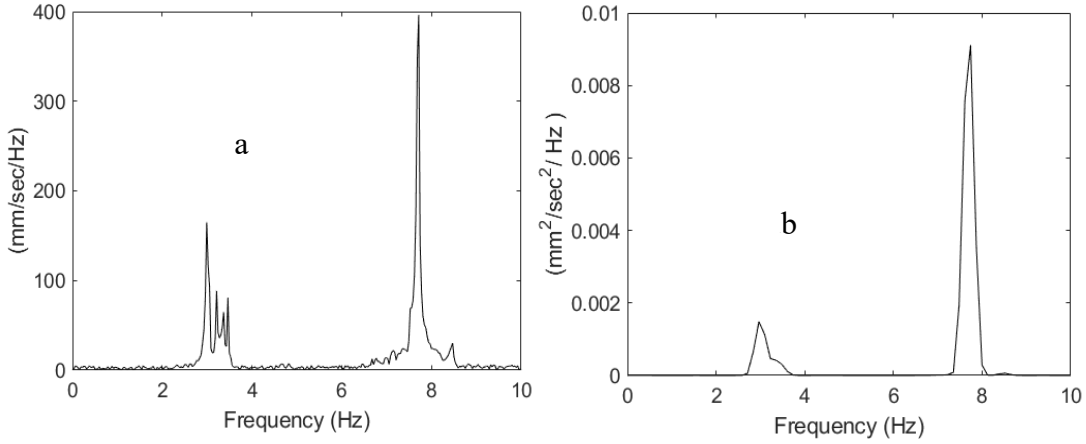

Figure 81: Lateral free vibration frequencies after passage of train 15 (Metro North) over the Cos Cob bridge (a) FFT and (b) PSD

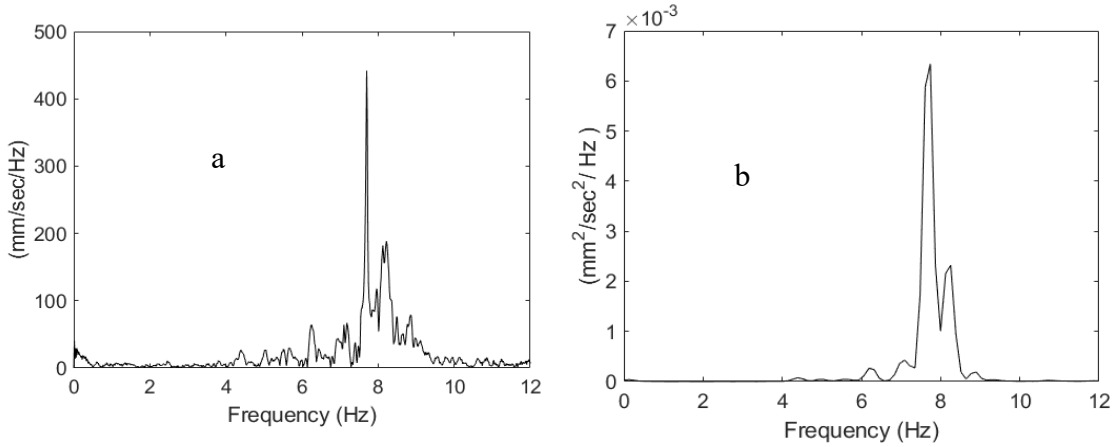

Figure 82: Vertical free vibration frequencies after passage of train 2 (Metro North) over the Cos Cob bridge (a) FFT and (b) PSD

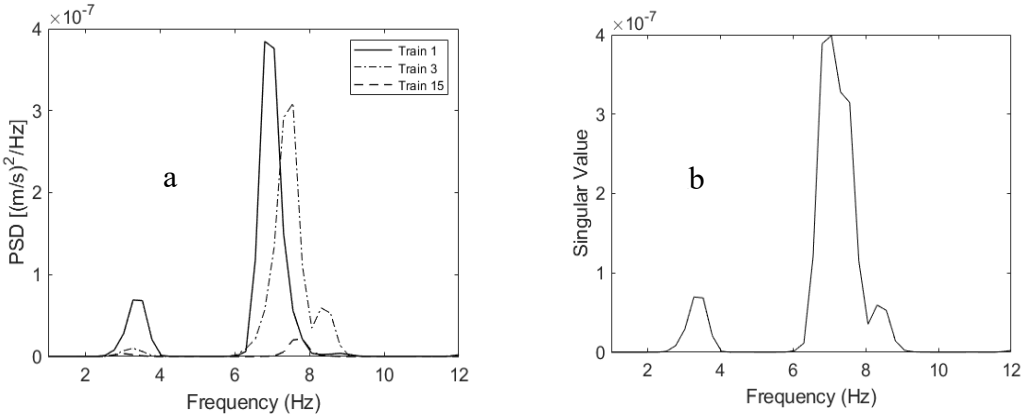

Figure 83: Lateral free vibration frequencies from Trains 1, 3, and 15; (a) PSD and (b) SVD

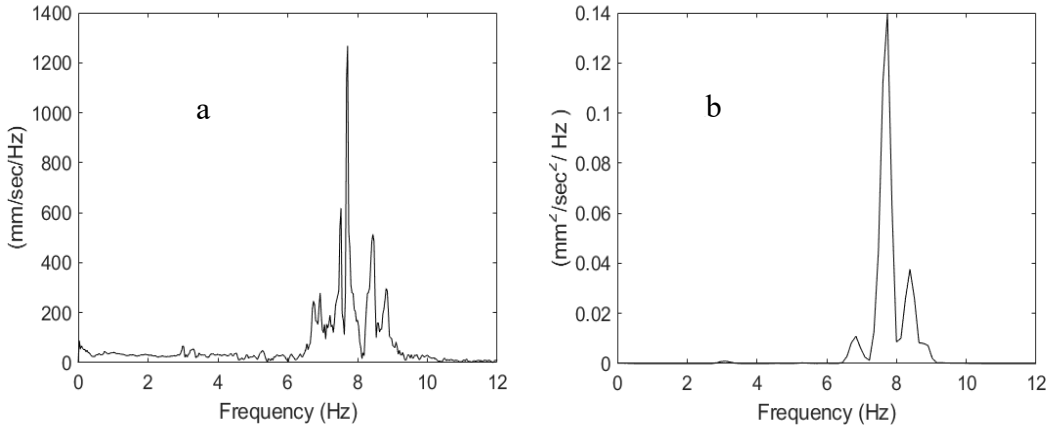

Figure 84: Vertical free vibration frequencies after passage of train 4 (Metro North) over the Cos Cob bridge (a) FFT and (b) PSD

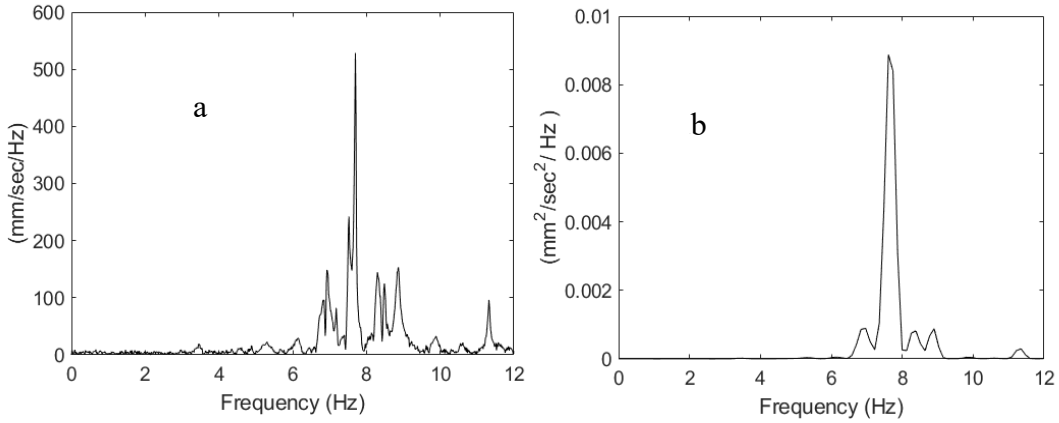

Figure 85: Vertical free vibration frequencies after passage of train 10 (Metro North) over the Cos Cob bridge (a) FFT and (b) PSD

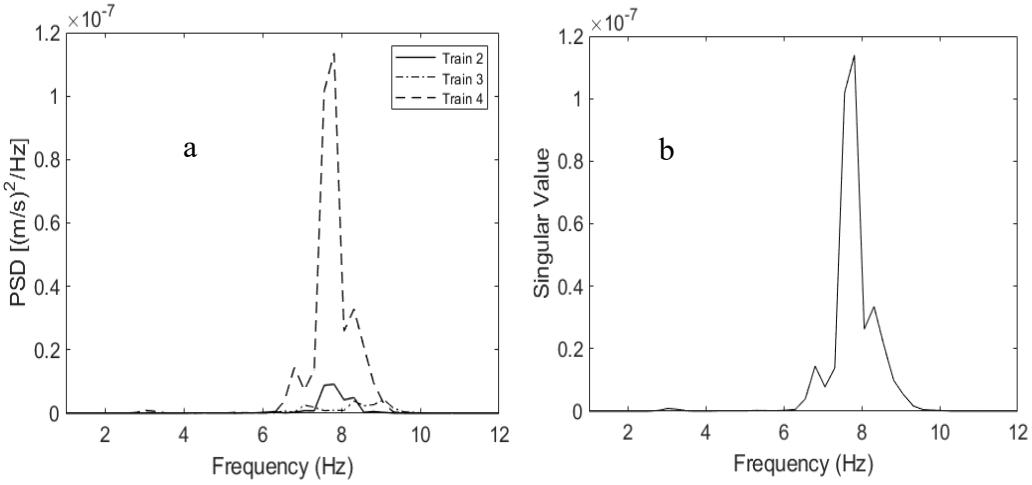

Figure 86: Vertical forced vibration frequencies for Trains 2, 3, and 4; (a) PSD and (b) SVD

3.2.2.3 Frequency Response from Accelerometer Data

The vertical and lateral free vibration responses obtained from the reference accelerometers attached to the bridge were also processed to find the natural frequencies of the bridge. Thus, the present results are compared with the estimates obtained from the free vibration response recorded using a Laser Doppler Vibrometer. The comparison shows that recurring peaks occur at the same frequencies. See Figure 68 for accelerometer location (Reference 1, 2 and 3 denoted as Ref 1, Ref 2 and Ref 3 respectively).

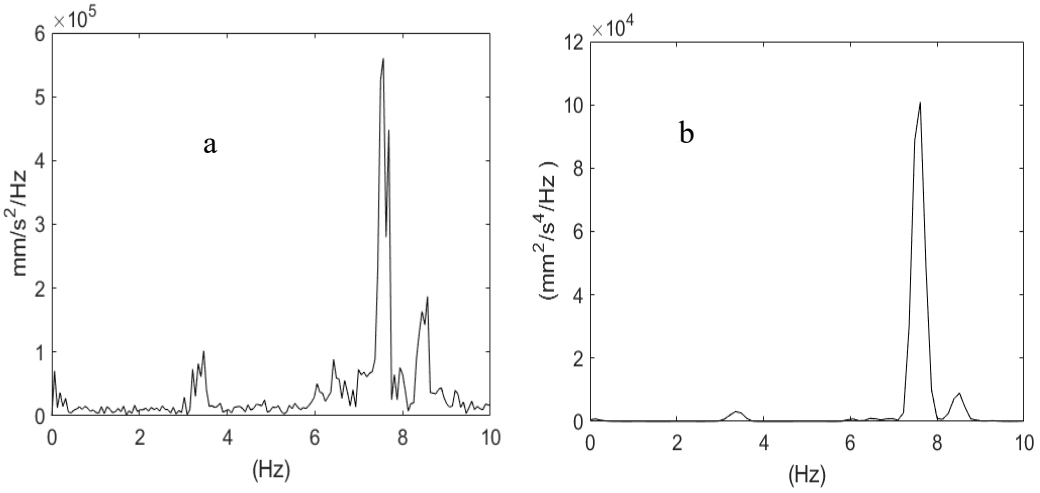

Figure 87: Lateral free vibration frequencies after passage of train 12 (Metro North) over the Cos Cob bridge (Reference 1) (a) FFT and (b) PSD

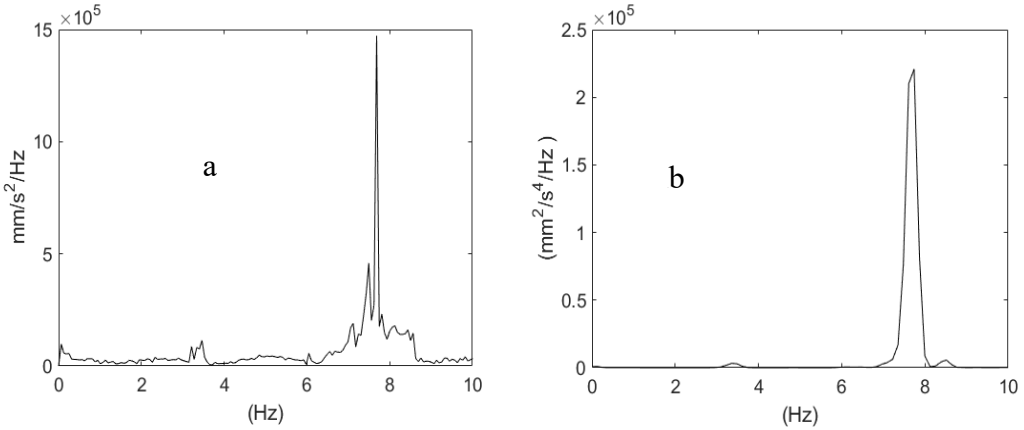

Figure 88: Lateral free vibration frequencies after passage of train 12 (Metro North) over the Cos Cob bridge (Reference 3) (a) FFT and (b) PSD

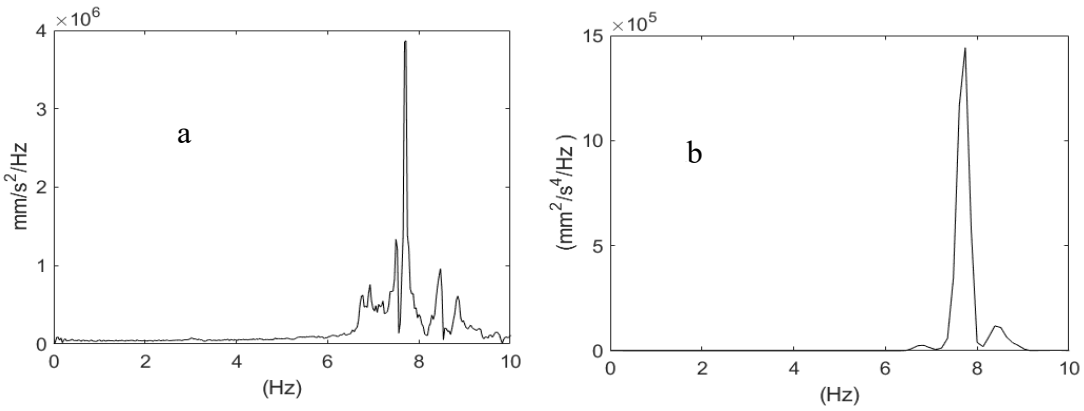

Figure 89: Vertical free vibration frequencies after passage of train 12 (Metro North) over the Cos Cob bridge from accelerometer (Reference 2) (a) FFT and (b) PSD

3.3 Finite Element Results and Comparison with Field Tests

This report has used existing inspection reports, as-built drawing, and field test data to compare and establish confidence in the FE model.

The first step was to compare the dead load from the model with the original drawing's specification. Second, the bridge FE modal analysis model results are compared with the field test data in the frequency domain (Mottershead and Friswell, 1993). Finally, a transient analysis involving the moving load is performed using the FE model, and the results are compared with the field test data.

3.3.1 Devon Bridge

Per current AREMA specifications, "the camber of trusses shall be equal to the deflection produced by the dead load plus a live load of 3,000lb per foot of track" (AREMA, 2022). Although the bridge was designed in the past century, the camber principle has been unchanged, as shown in Figure 90, where the bridge designer estimated dead load could be extracted by subtracting the camber diagram without stress in any member from the camber diagram under dead load.

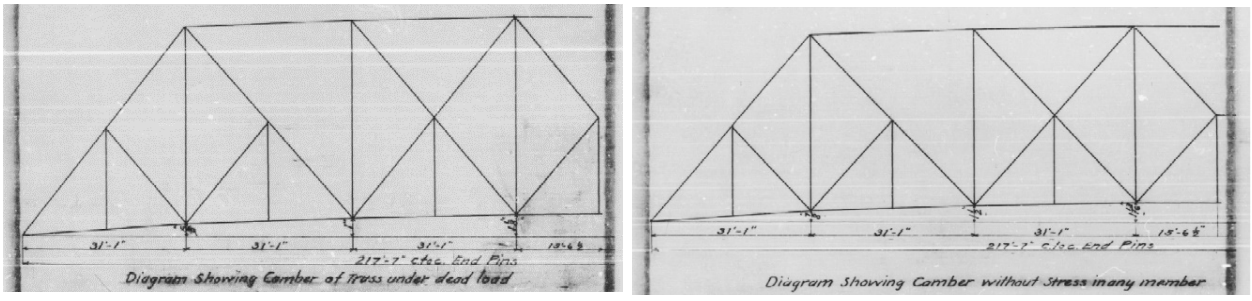

Figure 90: Devon bridge original drawings of camber diagram, (a) without stress in any members, (b) under dead load

The static model was used to verify and calibrate the bridge behavior and response under static equilibrium conditions. The bridge span self-weight was used to estimate the camber under dead load, Figure 91-a. The dead load camber diagram was used to verify the FE model behavior initially designed in the past century. Recently a few studies have shown that most eye bars do not take axial load equally even though initially they are designed to do so (Jacobs, Dhakal, and Malla, 2021). Figure 91-b shows the snapshot of the FE model that demonstrates the uneven axial load distribution on the eyebars, where the annotation tabs show the difference in the axial load from the same bundle of eyebars.

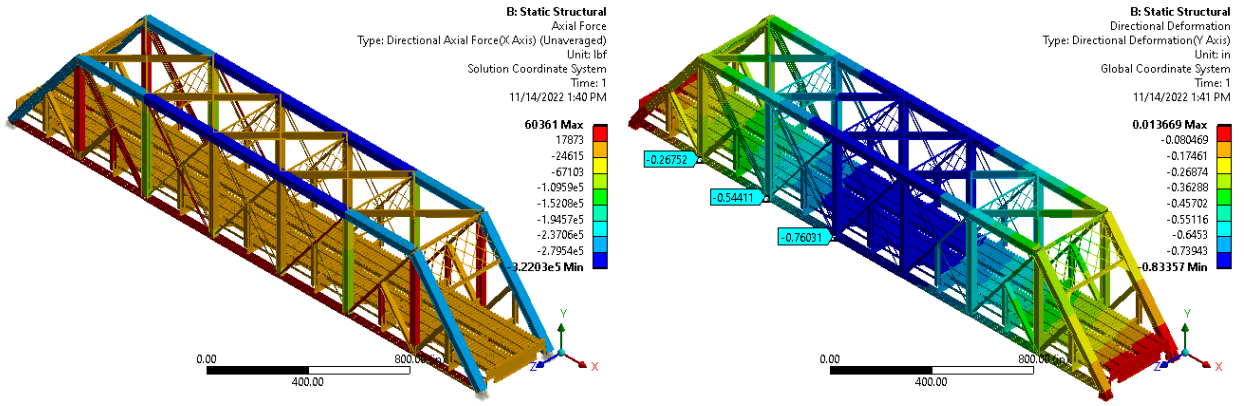

Figure 91: Devon bridge static model under self-weight, (a) vertical displacement, (b) member axial force

Table 21 compares the camber values between the as-built drawings and the FE model. The maximum difference is 20% between the design and the FE model self-weight analysis.

Table 21: Devon bridge: Dead load displacement FE model vs As-built drawings

Node @ Span Length	Camber [As-Built drawings]	FE model displacement	Difference camber with respect to FE model
L2 & L12	0.250 in (6.35 mm)	0.268 in (6.80 mm)	7.2%
L4 & L10	0.500 in (12.7 mm)	0.544 in (13.8 mm)	8.8%
L6 & L8	0.625 in (15.86 mm)	0.760 in (17.17 mm)	21.1%

The bridge's natural frequencies are one of the most critical parameters for a correct dynamic study of the bridge. These frequencies can be used to estimate the vehicle speed(s) required to create bridge resonance, and also the dynamic magnification factor assuming harmonic vibration (Tedesco, McDougal, and Ross, 1999). A modal analysis was carried out on the FE model to estimate more than 100 modes of vibration. Although most of the modes are local, it identified six global modes shown in Table 22. Table 22 shows the summary of the bridge span natural

frequencies compared with the mean-field test data natural frequencies. The results show a maximum error of 20% on the first lateral mode of vibration and an average of 3% for the remaining modes. Figure 92 shows the first four identified global mode shapes at auto scale factor.

Table 22: Devon bridge: Natural frequencies comparison, FE model vs field test (LDV and accelerometers)

FE model Mode	Mode of Vibration	FE model natural frequency (Hz)	Mean LDV natural frequency (Hz)	ACC natural frequency (Hz)	Difference FE model natural frequency with respect to LDV	Difference FE model natural frequency with respect to ACC
1	1st Lateral	1.431	1.783	1.784	19.35%	22.63%
6	Lateral + twist	2.556	2.556	*	0.40%	*
11	1st Longitudinal	3.223	3.596	*	11.57%	*
21	2nd Lateral	3.991	4.125	4.186	3.35%	4.88%
35	1st Vertical	4.442	4.474	4.895	-0.72%	10.19%
40	3rd Lateral	5.294	4.996	*	-5.62%	*
45	1st Twist	6.088	5.940	6.084	-2.43%	0.07%

* Bridge's natural frequency was not identified.

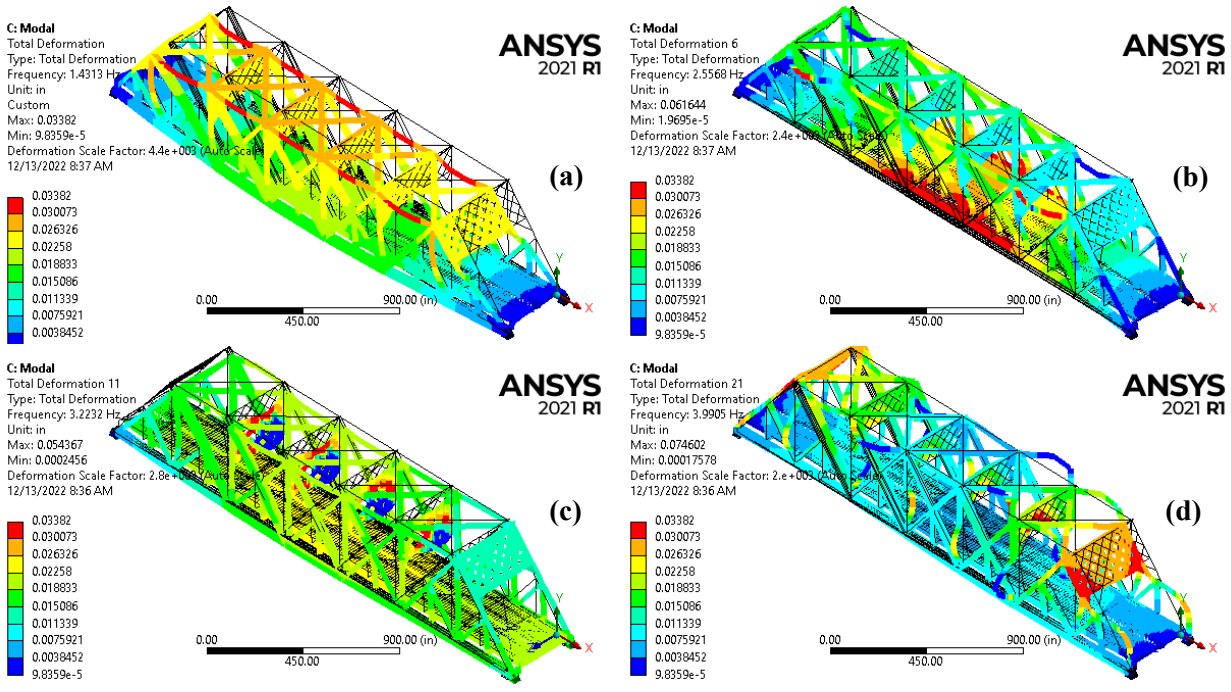

Figure 92: Devon bridge - FE model modal analysis: Mode shapes (a) first lateral, (b) lateral + twisting, (c) first longitudinal, and (d) second lateral

After the model was adjusted in static and modal analysis, the same model was used to replicate the data from the trains passing over the bridge span, recorded during the field tests. Figures 93 and 94 show the comparison between the computational model, in static and dynamic analysis, and the respective node displacement-time variation of the LDV field test data (Mottershead and Friswell, 1993). Table 23 shows the comparison of maximum and minimum displacement between the transient FE model and the field test data.

Table 23: Devon bridge: Summary results of time-domain parameters of relevant trains

Train	Travel Direction	Track	Car	Train Type	LDV	Travel Speed	Max. Vertical Displacement		Diff. with respect to LDV
							LDV	FE model	
1	East-West	4	9	MTNR M8	1	42 mph (68 km/h)	-0.30 in (-7 mm)	-0.16 in (-4 mm)	45%
3	East-West	4	8	AMTK Regional	2	43 mph (69 km/h)	-0.35 in (-9 mm)	-0.21 in (-5 mm)	40%
4	East-West	4	11	MTNR M8	2	41 mph (67 km/h)	-0.26 in (-6 mm)	-0.17 in (-4 mm)	32%
5	East-West	2	8	AMTK Acela	3	42 mph (68 km/h)	-0.41 in (-10 mm)	-0.27 in (-6 mm)	34%
7	East-West	4	8	AMTK Regional	3	41 mph (67 km/h)	-0.28 in (-7 mm)	-0.21 in (-5 mm)	24%
10	West-East	2	8	MTNR M8	4	17 mph (28 km/h)	-0.30 in (-7 mm)	-0.29 in (-7 mm)	3%
11	East-West	4	8	AMTK Regional	5	41 mph (66 km/h)	-0.65 in (-16 mm)	-0.39 in (-9 mm)	40%

The results presented in Figures 93 and 94 show that the displacements from the FE model are relatively smaller than the displacements from the field test using LDV. In the FE model developed for Devon bridge, this behavior is expected since the real-life bridge accounts for the bridge's aging, tear and wear, whereas the FE model assumes perfect conditions. The displacement comparison between the FE model and LDV data has shown good agreement regarding behavior and magnitude under the loading of typical cars (coaches). However, the maximum FE model displacement magnitude from locomotive/engine (Amtrak Regional and Amtrak Acela) has shown a significant difference. Some of the main reasons for this difference could be that the FE model did not account for the members' and connections' tear and wear, and the bridge-vehicle interaction as well. All data recorded using the LDV has observed an uplift on the east abutment side. and by overlapping with the FE model is possible to see that the uplift happens when the train is outside of the bridge span. The uplift phenomenon needs further study to understand the bridge behavior better. The displacement comparison has shown the need for further calibration of the FE model, with special focus on the connections and critical members. This is a part of the PI's ongoing research study related to railroad bridges.

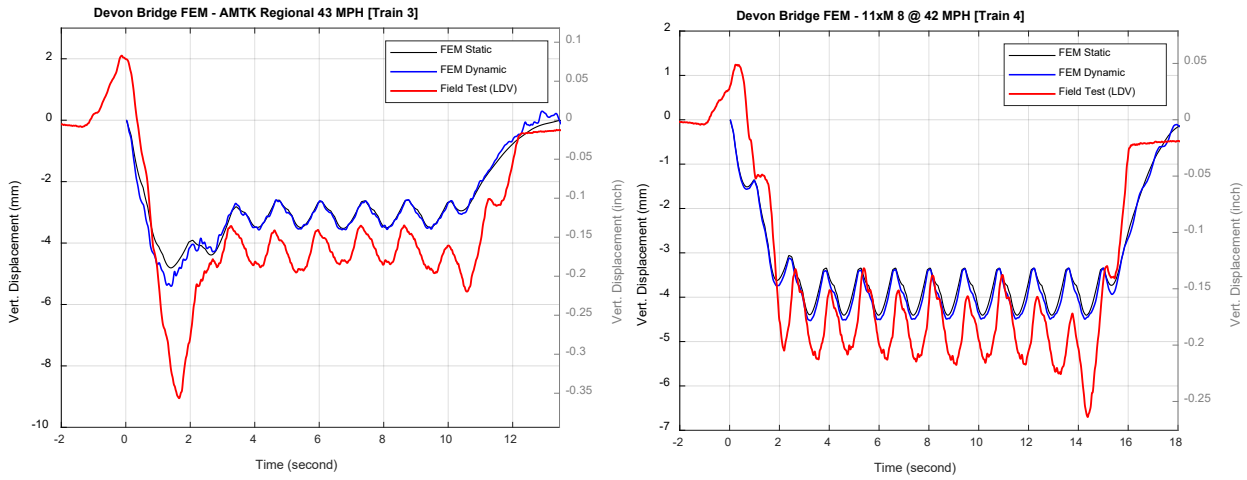

Figure 93: Devon bridge: FE model vs field test LDV plots at L12 node, (a) Train 3 and (b) Train 4

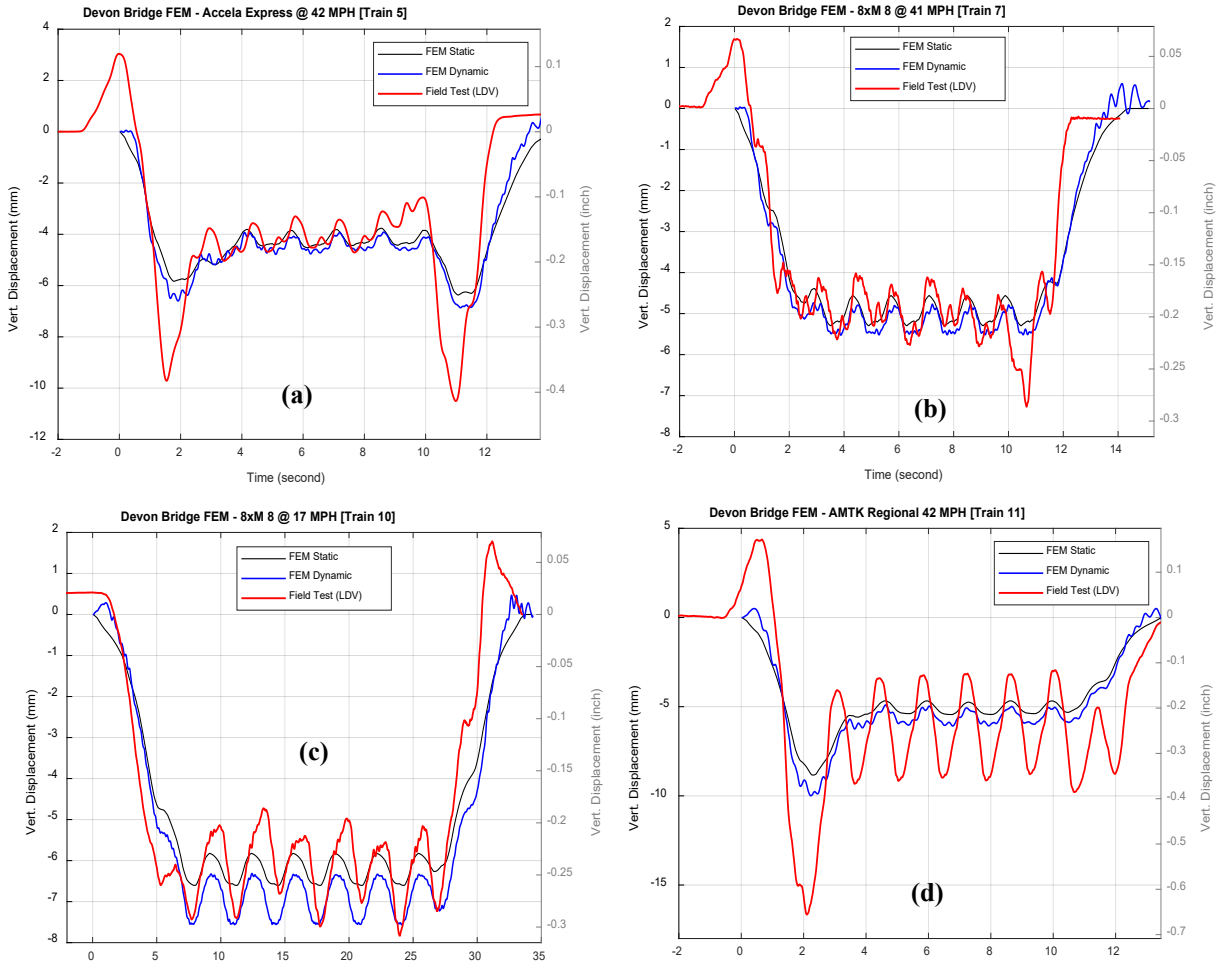

Figure 94: Devon bridge: FE model vs field test displacement vs time LDV plots at floor beam mid-span, (a) Train 5 at L10, (b) Train 7 at L10, (c) Train 10 at L8 and (d) Train 11 at L7

3.3.2 Cos Cob Bridge

The frequency analysis and the displacement results obtained from the field tests are compared with the results from the FE model analysis.

3.3.2.1 Modal Analysis

The modal analysis of the finite element model of the Cos Cob Bridge was performed in ANSYS to obtain the natural frequencies and mode shapes of the vibration. The first 150 modes of the bridge vibration along with their natural frequencies are obtained from the modal analysis. This analysis shows that the local modes are dominant over the global modes. This can be attributed to the presence of many components in this truss bridge. The first 20 modes of the bridge vibration along with their natural frequencies are presented in Table 24. Three global mode shapes of the bridge (also identified from field experiment and listed in Table 25) are presented in Figures 95 and 96, which include two lateral modes and one vertical mode. No longitudinal mode was observed in the 150 extracted mode shapes.

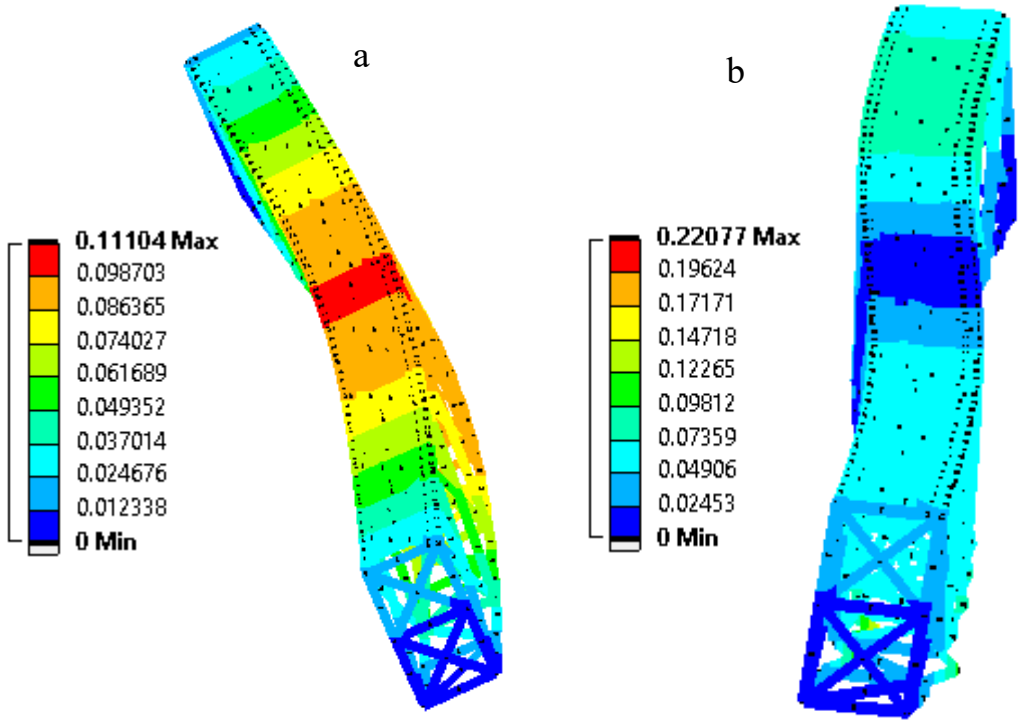

Figure 95: Global Mode Shapes: (a) first lateral and (b) second lateral

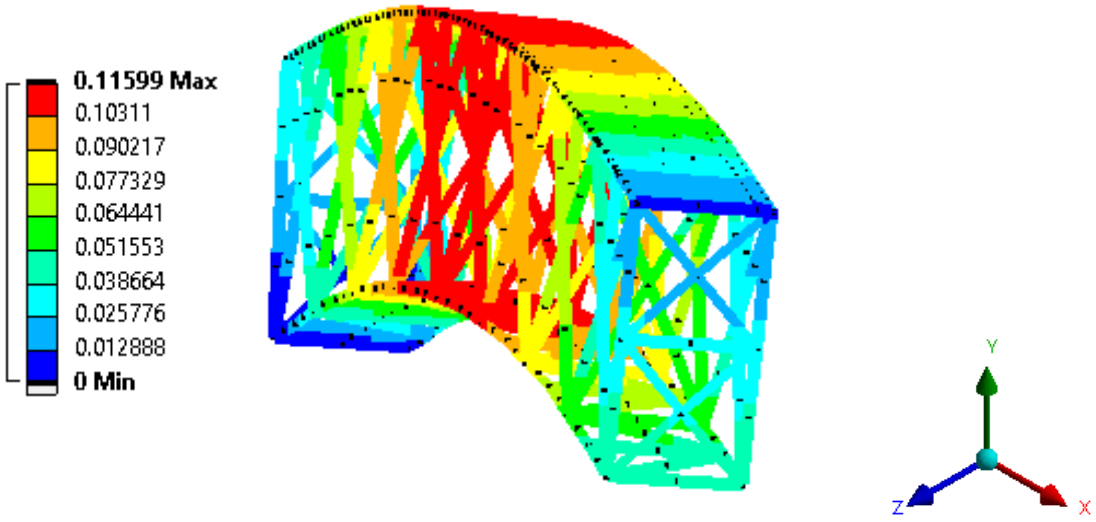

Figure 96: Global First Vertical Mode Shape

Table 24: First 20 modal frequencies and mode shapes of the Cos Cob bridge from the FE model

Mode	Frequency (Hz)	Mode Type
1	3.7985	First Lateral (Global Mode)
2	8.0432	First Twist (Global Mode)
3	8.2457	First Vertical (Global Mode)
4	8.6978	Second Lateral (Global Mode)
5	10.323	Local
6	10.376	Local
7	10.404	Local
8	10.427	Local
9	10.428	Local
10	10.438	Local
11	10.439	Local
12	10.441	Local
13	12.723	Third Lateral (Global Mode)
14	13.332	Local
15	14.579	Local
16	14.622	Local

17	14.644	Local
18	14.67	Local
19	14.724	Local
20	14.765	Local

3.3.2.2 Natural Frequency Comparison: Field Test vs FE model

The first three natural frequencies of bridge vibration obtained from the field tests are compared to the natural frequencies from FE analysis as shown in Table 25. From the comparison, it is found that the natural frequencies obtained from FE analysis are close to those obtained from the field tests, with a maximum difference of about 10% in the first mode.

Table 25: Comparison of first three natural frequencies obtained from field experiments and FE analysis

Modes	FE model (Hz)	Field Exp. (LDV) (Hz)	% Difference w.r.t field values
First Lateral	3.79	3.42	9.96
Second Lateral	8.69	7.89	9.28
First Vertical	8.24	7.54	8.55

3.3.2.3 Vertical Displacement Comparison: Field Test (LDV) vs FE model

The vertical displacement results estimated from the field test are compared with the results from the FE model. The comparison shows that the results are in reasonable agreement. The results are summarized in Table 26 and Figures 97-99 below.

Table 26: Nodal Displacement: FE model vs Field Test using LDV

Train	Traveling Direction	Track	No. of Cars	Train Type	Vib. Loc	Estimated Traveling Speed	Maximum Displacement (Field Test: LDV)	Maximum Displacement (FE model Transient)	% Difference w.r.t Field Test
2	W-E	4	8	MTNR	1 (Node)	37.87 mph (60.94 km/h)	-0.122 in (-3.11 mm)	-0.141 in (-3.59 mm)	15.4
4	W-E	4	8	MTNR	2 (Node)	42.41 mph (68.23 km/h)	-0.131 in (-3.32 mm)	0.116 in (-3.57 mm)	7.53
5	W-E	4	10	MTNR	3 (Node)	37.36 mph (60.12 km/h)	-0.094 in (-2.38 mm)	-0.116 in (-2.95 mm)	19.3
6	W-E	4	10	MTNR	4 (Node)	39.98 mph (64.34 km/h)	-0.094 in (-2.39 mm)	-0.1125 in (-2.86 mm)	19.6

8	W-E	4	8	MTNR	3 (Node)	41.93 mph (67.48 km/h)	-0.103 in (-2.61 mm)	-0.1047 in (-2.81 mm)	7.66
9	W-E	2	8	AMTK Regional	5 (Node)	28.07 mph (45.17 km/h)	-0.142 in (-3.61 mm)	-0.169 in (-4.31 mm)	19.3
21	W-E	4	8	MTNR	11 (Node)	37.85 mph (60.91 km/h)	-0.133 in (-3.38 mm)	0.169 in (-3.68 mm)	8.87

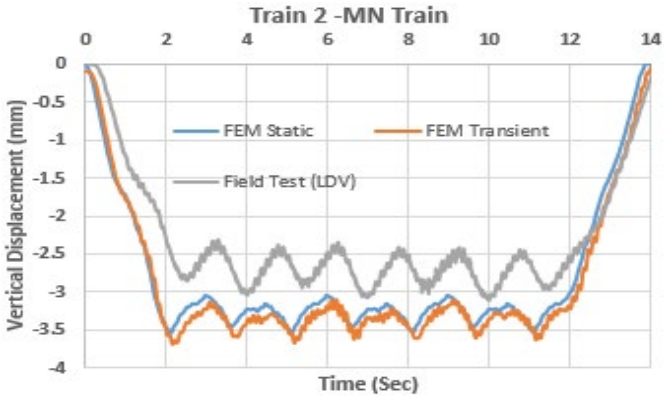

Figure 97: Vertical displacement vs. time at node Vib.1 subjected to 8-car Metro North train moving at 34 mph from New York to New Haven on track 4 of Cos Cob bridge, CT. (Train 2)

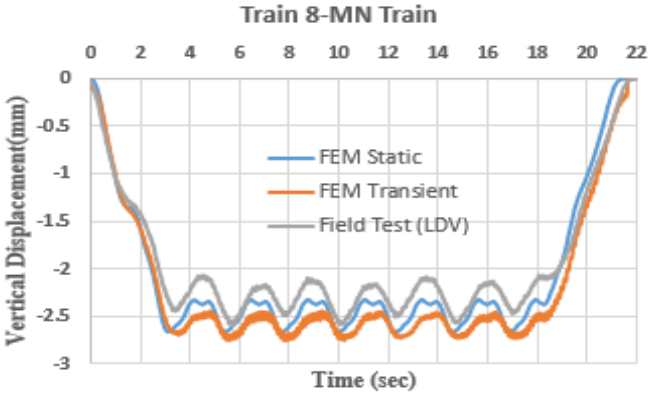

Figure 98: Vertical displacement vs. time at node Vib3 subjected to 8-car Metro North train moving at 41.93 mph from New York to New Haven on track 4 of Cos Cob bridge, CT. (Train 8)

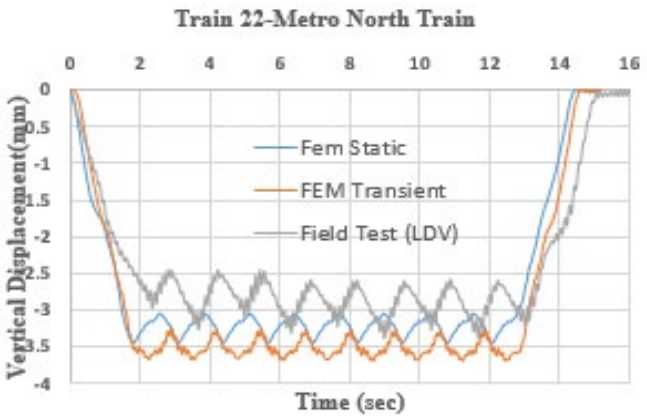

Figure 99: Vertical displacement vs. time at node Vib.12 subjected to 10-car Metro North train moving at 37 mph from New York to New Haven on track 4 of Cos Cob bridge, CT. (Train 22)

The results presented in the Figure 97-99 show that the displacements from the FE model are greater than the displacements from the field test using LDV. One reason could be that the gusset plate, lacing bars and the discontinuous cover plate along the length of the top and the bottom chords of the bridge span are not included in the FE model, and the FE model did not account for the bridge-vehicle interaction. Another reason could be that the actual end conditions are more flexible than the one modeled in FE model. These reasons could have made the FE model less stiff than the actual bridge contributing to slightly higher deflection in comparison to field test results. Therefore, further improvement/refinement in the FE model is needed. This is a part of the PI's ongoing research investigation on Railroad Bridge.

Chapter 4: Summary, Conclusions and Recommendations

This chapter presents the research summary, conclusions, and recommendations. First, a summary of the material testing, field testing, and FE model results are presented and interpreted. Second, the seven point's conclusion is presented. Finally, the report recommends a future study of the combination of material testing, field testing, and FE model of long-span open-deck truss railroad bridges.

4.1 Summary

The dynamic responses from two old, more than 115 years, long-span steel truss bridges (Cos Cob Bridge and Devon Bridge) located in Connecticut were studied to determine natural frequencies, mode shapes, and nodal displacements under service loading of Amtrak Acela, Amtrak Regional, and Metro-North trains at various speeds. This was achieved by field testing using two types of sensors (LDV and accelerometers), Finite Element Modeling (FE model) using ANSYS, and result comparison. Apart from this, the bridge materials used in constructing these bridges, in addition to other two old bridges, Atlantic Street Bridge located in Connecticut (demolished), and Aroostook Street Bridge located in Maine, which is still in operation, were tested to determine the tensile properties.

To study the bridge structural dynamic response, the first comprehensive FE models of these two bridges were developed in ANSYS using as-built drawings and load rating reports from the Connecticut Department of Transportation (CONN DOT). Static, modal, and dynamic analyses were performed to determine the static displacement, natural frequencies and mode shapes, and dynamic displacement. Later, to validate the FE model, field tests were performed on the bridges over one year under two different phases. The first field testing phase includes the excitation of the bridge with a shaker and the collecting of responses with a laser scanner. However, this phase proved less fruitful to the research team because the shaker excitation needed more power to vibrate these superstructures. Therefore, minimal outcomes achieved from this testing are presented in earlier sections. The second research phase includes collecting data under the service loading excitation using accelerometers and LDV. The bridge responses were measured in terms of acceleration-time and velocity-time histories. These data were processed and analyzed to determine the bridge's natural frequencies and displacements at various nodes. Finally, the parameters obtained from the field tests were compared and correlated with the results of FE analyses performed on the computational models developed for this study.

To study the tensile properties of these bridge materials, virgin samples obtained from these bridges were first lead abated from sandblasting. Then the specimen was prepared and tested as per ASTM standards to determine the yield strength, ultimate tensile strength, breaking point strength, and corresponding strains. The results thus obtained were compared to results in other literature. The comparison shows that these materials have retained the yield strength property, but the ultimate tensile strength has been reduced slightly.

4.2 Conclusion

The conclusions drawn from this research study are summarized below:

1. A methodology has been established to process and analyze the acceleration-time and velocity-time signals collected from the accelerometer and LDV, respectively, to determine natural frequencies of the railroad bridge under service loading using free vibration response after the train passes over the bridge. The field experiment identified seven natural frequencies (two lateral, one vertical, one longitudinal, and three torsional) and three natural frequencies (two lateral and one vertical) for the Devon bridge and the Cos Cob bridge, respectively. The observations show that both bridges are less stiff in the lateral direction since the first identified modes are lateral. The forcing frequencies of the train are also identified by processing the field data.

2. Another methodology has also been established to determine the displacement on the bridge under the service loading condition from the velocity-time response collected using LDV. The nodal displacement-time history has been determined for the nodes where the laser beam was pointed. The results show that the magnitude of peak displacement depends on the type of train traveling over the bridge. The displacement decreases as we move left or right toward the supports. For example, from the recorded data, the maximum midpoint displacement of 16.65 mm (0.656 in) is determined for the Devon Bridge when Amtrak Regional passes over the bridge span at 41.28 mph (66.43 km/hr.). Similarly, the maximum midpoint displacement of 3.38 mm (0.133 in) is determined for the Cos Cob bridge when the Metro-North M8 train passes over the bridge at 37.85 mph (60.91 km/hr).

3. The LDV displacement plot from Devon bridge has shown an uplift on the east abutment. The uplift was between 20% and 25% of the maximum displacement in the same node. Additional study is required to understand and evaluate this uplift phenomenon observed in the Devon bridge.

4. A technique has been developed to model old railroad bridges composed of members with complex cross-sections (unlike standard cross-sections in most FE packages). The finite element (FE) models of the Cos Cob and Devon bridges have been developed to perform static, modal, and dynamic analyses. The results from the modal and dynamic FE analyses were compared to the results from the field test and have shown good agreement.

5. The results obtained from the tensile test are compared to ASTM A7 material specification dated back to 1939, the Fritz Laboratory Report (Rao, 1963) and the data in the technical paper “Development and Use of High-Performance Steel” (Reidar, 2004). The comparison shows that the materials have maintained their yield strength while the ultimate tensile strength is slightly reduced. The ASTM A7 material specification from 1939, defines the average yield stress and ultimate stress as 33.00 ksi (227.52 MPa) and 66.00 ksi (455.05 MPa) respectively. Reider (2004) found that the yield strength could vary from 220 MPa to 240 MPa.

6. The yield strength of the material from the Aroostook Bridge increases with the extension rate, but this is more significant when the extension rates are significantly higher. When the extension rates are relatively low (1 mm/min and 4 mm/min), the yield strength remains almost unaltered.

7. Ultimate tensile strength of the material from the Aroostook Bridge also increases with an increase in extension rate, but this also is more significant when the extension rates are higher (8 mm/min, 100 mm/min, and 500 mm/min). At a lower extension rate (4 mm/min), slightly lower yield strength is observed.

8. No significant change in breaking point strength is observed with an increase in the material extension rate from the Aroostook Bridge. However, a slightly lower breaking point strength is observed at 8 mm/min.

The combination of field test data and computational models has shown the potential to evaluate old railroad bridges better. The comprehensive FE model represents the bridge's perfect operation scenario without any wear and tear. The correlation between the field test data and the FE model helps to determine the extent of defects in the bridge. A greater correlation shows lesser damage and loss of stiffness.

Practicing bridge engineers can use the methodologies presented in this report to better understand the dynamic behavior of old railroad bridges. In addition, the methodologies described here can be helpful for the condition assessment of aging bridge structures, which in turn can promote and enhance their service life.

4.3 Recommendations

Although this study has highlighted some bridges' dynamic responses using field testing, FE modeling, and the material testing to determine the tensile properties of the bridge materials, the research team recommends a better understanding of some discrepancies. Those discrepancies include uplifting in the displacement-time history of the Devon Bridge observed in the field tests, as well as the quantitative difference in the displacement results obtained from FE analysis and those derived from the field tests described in this report:

- The dynamic response of a railroad bridge structure is a complex interaction between the bridge and the train. However, the dynamic analysis in the FE model does not consider this interaction. Detail study is needed considering the effect of train mass, stiffness, and damping from the suspension system to predict dynamic response more accurately.
- The free vibration frequencies that are estimated in this report are determined from the free vibration response after the train passes over the bridge. There should also be forced vibration frequencies of the bridge subjected to the loading of each train. A thorough analysis of the forced vibration response is needed to determine the forced vibration frequencies of the bridge. Validation of the results is also necessary.
- This study does not address the effects of train speed on the dynamic response of the bridge. Further field testing is required at various speeds of trains to understand this effect.
- In the current study the displacement results from the finite element models and the field tests are not as close as expected. Therefore, further research to improve and refine the finite element models of such complicated long span truss type railroad bridges are recommended.

- Tensile test results from the Aroostook Bridge in Maine show an increase in yield strength with an increase in extension rate, which is more pronounced at higher extension rates (8 mm/min, 100 mm/min, and 500 mm/min), although the yield strength at 1 mm/min and 4 mm/min remained almost identical. A detailed study is needed to explain this behavior.
- Although the tensile testing has highlighted some tensile properties of these vintage ASTM A7 materials, fabricated and used for more than a century, more mechanical testing (e.g., Fatigue Test) is needed to understand the fatigue life. In addition, these bridges have been under operation for almost 115 years and have gone through many cycles under operation. Therefore, it is reasonable to surmise that fatigue may be a more critical failure mode for these bridges.

References

AAR (1968). *Field Investigation of a Truss Span on the Great Northern Railway*. Association of American Railroads (AAR). Chicago, IL.

A.G. Lichtenstein & Associates (1989). *Repair Plan Drawing: Cos Cob Bridge No. 29.91, Rehabilitation of New Haven Line Moveable Bridges*. Metro North Commuter Railroad Company, Connecticut Department of Transportation, Newington, CT.

American Bridge Company (1905). *Fabrication Drawings: Bridge #106 Over Housatonic River, Naugatuck Jct, Conn., N.Y. div.* Connecticut Department of Transportation. Newington,CT.

ANSYS (2009). *Theory reference for the mechanical APDL and mechanical applications*. ANSYS Inc. Canonsburg, PA.

AREMA (2017). "Special consideration for structures and HSR operations." Structure and HSR Recommendations. High speed rail structures task force - American Railway Engineering and Maintenance-of-Way Association (AREMA), Lanham, MD.

AREMA (2022). "Manual for railway engineering, Chapter 15 - Steel Structures." American Railway Engineering and Maintenance-of-Way Association (AREMA). Lanham, MD.

ASTM (1939). "Standard Specifications for Steel for Bridges and Buildings." *ASTM Standard A7*, ASTM International. West Conshohocken, PA.

ASTM (2016). "Standard Test Method for Tension Testing of Metallic Materials." *ASTM Standard E8/E8M-a*. ASTM International. West Conshohocken, PA.

ASTM (2017). "Standard Test Method for Young's Modulus, Tangent Modulus, and Chord Modulus." *ASTM Standard E111-a*, ASTM International. West Conshohocken, PA.

Bajer, C. I., and Djniewicz, B. (2012). *Numerical analysis of vibration of structures under moving inertial load.* Springer. New York, NY.

Baniya, S. (2015). "Modeling and Analysis of a Steel Truss Railroad Bridge Traversed by Trains at Various Speeds." *M.S. Thesis*. Department of Civil & Environmental Engineering, University of Connecticut. Storrs, CT.

Biggs, J. M. (1964). *Introduction to Structural Dynamics.* McGraw-Hill Inc. New York, NY.

Bolotin, V. V. (1964). *The dynamic stability of elastic systems.* Holden-Day: San Francisco, CA.

Bro, R., and Age, K. S. (2003). "Centering and scaling in componet analysis." *Journal of Chemometrics*, 17, 16-33.

Burns, A. (2022). "Amtrak's Acela Express." America Rails. https://www.american-rails.com/ (October 20, 2022).

Cantero, D., M. Ülker-Kaustell, and Karoumi R. (2016). "Time-frequency analysis of railway bridge response in forced vibration." *Mech Syst Signal Process 76–77*, 518–530. (https://doi.org/10.1016/j.ymssp.2016.01.016).

CFR (2022). *Title 49 – Transportation. Part 213 - Track Safety Standards*. Code of Federal Regulations (CFR) National Archives .Washington, DC. https://www.ecfr.gov/current/title-49 (November 10, 2022)

Chopra, A. K. 2017. *Dynamics of structures.* Pearson. New York, NY.

Clough, Harbour and Associates (2011). *Load Rating Report: Project No. 17888, Cos Cob Railroad Bridge Project*, Connecticut Department of Transportation, Bureau of Highways Bridge Safety and Evaluation, Newington, CT.

FRA (2018). *Bridge safety Standards compliance manual.* Federal Railroad Administration (FRA). Washington, DC. https://railroads.dot.gov/sites/fra.dot.gov/files/fra_net/18208/Bridge%20Safety%20Standards%20Compliance%20Manual%20Final.pdf (June 20, 2022).

Frýba, L. (2000). "A rough assessment of railway bridges for high speed trains." *Engineering Structures*, 548-556.

Golub, G., and Kahan W. (1965). "Calculating the Singular Values and Pseudo-Inverse of a Matrix." *Journal of the Society for Industrial and Applied Mathematics B*.

Hatch, M. R. (2000). *Vibration simulation using MATLAB and ANSYS.* CRC Press LLC. Boca Raton, FL.

Hilal, M. A., and Zibdeh, H. S. (1999). "Vibration analysis of beams with general boudary conditions traversed by moving load." *Jornal of sound and vibration*, 377-388.

Jacobs, D. W., Dhakal, S., and Malla, R. B. (2021a). "Live-load response of eyebars on a 110-year-old steel truss railroad bridge." *Pract. Period. Struct. Des. Constr.* 26(1): 04020045. (https://doi.org/10.1061/(ASCE)SC.1943-5576.0000523).

Jacobs, D. (2021). "Dynamic Impact Factors Produced by Trains on Long Span Open Deck Steel Truss Railroad Bridges". Ph.D. Thesis. Department of Civil & Environmental Engineering, University of Connecticut. Storrs, CT.

Kaium, S. A., S. A. Hossain, and J. S. Ali. (2020). "Modal parameter extraction from measured signal by frequency domain decomposition (FDD) technique." *International Journal of Structural Integrity 11 (2)*, 324–337. (https://doi.org/10.1108/IJSI-06-2019-0062).

Lochner (2011). *Connecticut Rairoad Equipment - Equivalent Cooper Load Charts.* Connecticut Department of Transportation, Office of Rail. Newington, CT.

Löwenborg, P. B., Gustafsson, O., and Wanhammar, L. (1999). "Filter design using MATLAB." *ReserchGate*.

https://www.researchgate.net/publication/228945801_Filter_design_using_MATLAB (March 15, 2022).

Malla, R. B., Baniya, S., and Jacobs, D. W. (2016). "Study of Dynamic and Static Response of an Old Truss Railroad Bridge." *Procs*, *Earth & Space 2016 Conference*. ASCE, Reston, VA. 1052-1062. (https://doi.org/10.1061/9780784479971.101).

Malla, R. B., Jacobs, D. W., Dhakal, S., and Baniya, S. (2017). "Dynamic Impact Factors on Existing Long-span Railroad Bridges." *Final Report, IDEA Rail Safety Project, RS-25*. Trasnportation Reserch Boad, Washignton DC. (http://onlinepubs.trb.org/onlinepubs/IDEA/FinalReports/Safety/Safety25.pdf).

MATLAB (2022). *Signal Processing Toolbox - User's Guide (as R2022a).* The MathWorks Inc. Natick, MA.

Mottershead, J. E., and Friswell, M. I. (1993). "Model updating in structural dynamics: A survey." *Journal of sound and vibration 167-2*, 347-375.

Nagaraja, Rao, (1963). "Material properties of structural carbon and high strength steels." *Lehigh Preserve Institutional Repository*, Allentown, PA. https://preserve.lib.lehigh.edu/islandora/object/preserve%3Abp-3378273 (Accessed: Nov. 21, 2022)

Nassif, H. H., Gindy, M., and Davis, J. (2005). "Comparison of laser Doppler vibrometer with contact sensors for monitoring bridge deflection and vibration." *NDT&E International 38*, 213-218.

Norén-Cosgriff, K., and Kaynia, A. M. (2021). "Estimation of natural frequencies and damping using dynamic field data from an offshore wind turbine." *Marine Structures 76,* 1-14. 102915. (https://doi.org/10.1016/j.marstruc.2020.102915).

Petrescu, F. I. (2012). *A new doppler effect.* Books on Demand GmbH. Norderstedt, Germany.

Polytec (2015). *Polytec scanning vibrometer - PSV theory (As of software 9.1 ed.)*. Polytec Inc. Hudson, MA.

Reidar, B., (2004). "Development and use of high-performance steel." *J Constr Steel Res*, 60 (3–5): 393–400. (https://doi.org/10.1016/S0143-974X(03)00118-4.)

Reiterer, M., Lachinger, S., Fink, J., and Bruschetini-Ambro, S. Z. (2018). "In-Situ Experimental Modal Testing of Railway Bridges." *Procs., 18th International Conference on Experimental Mechanics 2*, 413. (https://doi.org/10.1016/j.marstruc.2020.102915).

Rossi, G., Gussella, V., and Gioffré, M. (2002). "Comparison between accelerometer and laser vibrometer to measure traffic excited vibrations on bridges." *Shock and Vibration 9*, 11-18.

Schiefer, M. I., and Dosch, J. (2012). *ICP® Based reference accelerometers.* PCB Piezotronics. Inc Depew, NY.

Stantec (2011). *Load Rating Report: Bridge No. 08080R, In-Depth Inspection of Devon Railroad Bridge.* Connecticut Department of Transportation, Bureau of Higways Bridge Safty and Evaluation. Newington, CT.

Siemens (2019). *Amtrak Cities Sprinter ACS-64 - Electric Locomotive.* Siemens Mobility. Munich, Germany. https://assets.new.siemens.com/siemens/assets/api/uuid:cf24f8f7-5392-4c70-9d2e-915e3e0600df/amtrak-acs64-cities-sprinter.pdf (September 30, 2022).

TransSystem and Lochner (2021). *Railroad Bridge Inspection: Bridge No. 08080R, Volume 3: Load Rating Analysis of Span 5,6 & 7.* Connecticut Department of Transportation, Office of Rail. Newington, CT.

Tedesco, J. W., McDougal, W. G., and Ross, C. A. (1999). *Structural Dynamics: Theory and application.* Addison Wesley Longman, Inc. Menlo Park, CA.

Underwater Construction (1990). *As Built Drawings: Cos Cob Bridge No. 29.91, Rehabilitation of New Haven Line Movable Bridges Superstructure Repair.* Metro-North Commuter Railroad Commuter Co. Connecticut Department of transportation, Newington, CT.

Wenzel, H. (2009). *Health monitoring of bridges.* John Wiley & Sons Ltd. Chichester, UK.

Yang, Y. B., Yau, J. D., and Wu, Y. S. (2004). *Vehicle-bridge interaction dynamics - with appilcation to high-speed railways.* World Scientific Publishing Co. Hackensack, NJ.

Yang, Y. B., Zhang, B., Wang, T., Xu, H., and Wu, Y. (2019). "Two-axle test vehicle for bridges: Theory and applications." *International Journal of Mechanical Sciences 152*, 51-62. (https://doi.org/10.1016/j.ijmecsci.2018.12.043).

Yoon, H., Chin, W. J., Kang, J. Y., Kwark, J., and Hwang, E.-S. (2013). "Computation of impact factor of high-speed railway bridge by KTX train riding Test." *Scientific research 5*, 751-755. (http://dx.doi.org/10.4236/eng.2013.59090).

Appendix A: Devon Bridge Field Measured Raw Data

During the field test performed on Devon bridge on June 8th, 2021, the research team recorded the bridge response under 11 service trains crossing the bridge at five different LDV locations and using two accelerometers in a vertical and horizontal position, designated ACC 1, and ACC 2, respectively. Figure A-1 shows the LDV locations (LDV 1 to LDV 5) and vertical and horizontal accelerometer locations, ACC 1, and ACC 2, respectively.

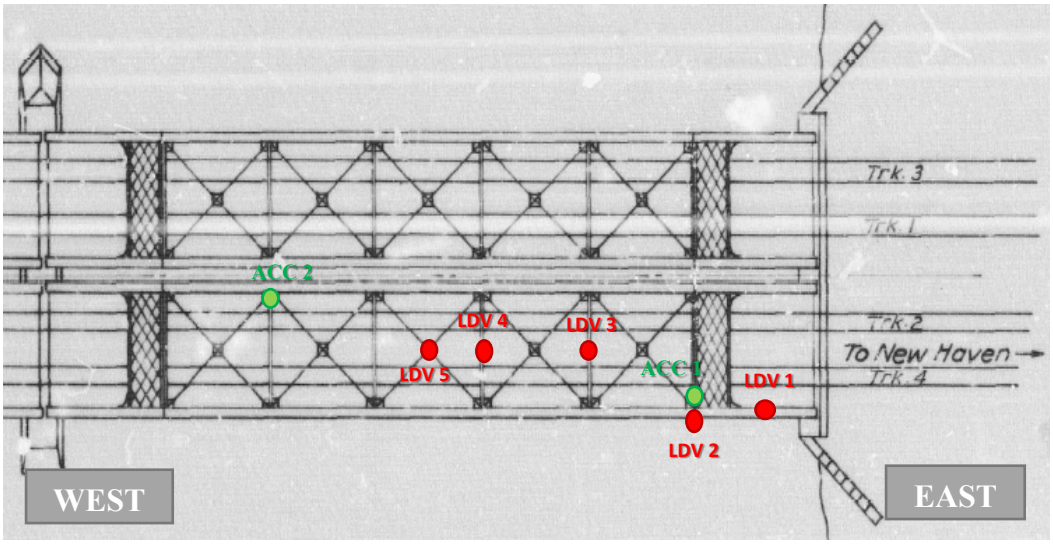

Figure A-1: Devon Bridge LDV and accelerometer location

The raw data recorded from the field, as mentioned earlier, is presented below. The data is presented in and uniform to the fashion matter. Starting with a clarification paragraph describing the train composition, traveling direction, and LDV recorded location. Then, two plots from the recorded bridge response are presented. The left side plot represents the relative velocity response collected from the bridge at one of the five LDV locations, the prepossessing, and the converted displacement time variation response. The right-side plots compare the relative acceleration obtained from the LDV and the bridge acceleration obtained from the vertical and horizontal accelerometers, ACC 1 and ACC 2, respectively. Furthermore, Train 4 and Train 11 show the acceleration comparison on a grander scale and the RMS values using the current bandwidth in red.

Below are the eight most relevant raw data from the trains passing directly above the studied bridge span, the south bridge.

Train 1: Typical MTRR M8 composition with eight couches, traveling East-West direction on track 4, and LDV data recorded at the hangar node, denominated LDV 1.

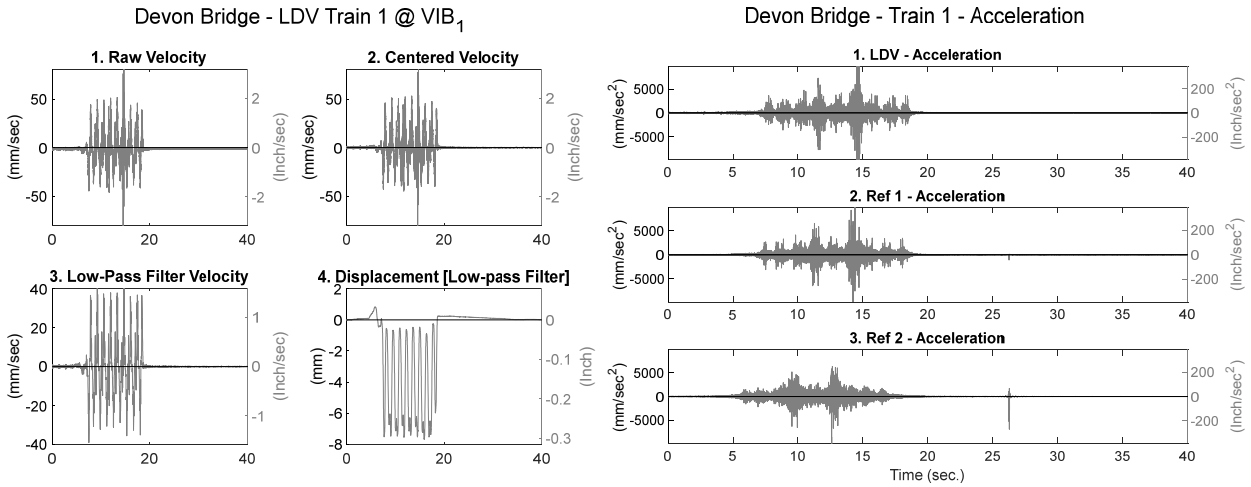

Figure A- 2: Train 1: Time variation data, velocity, displacement, and acceleration

Train 3: Typical AMTK Regional composition with seven couches and power engine, traveling East-West direction on track 4, and LDV data recorded at the vertical post node, denominated LDV 2.

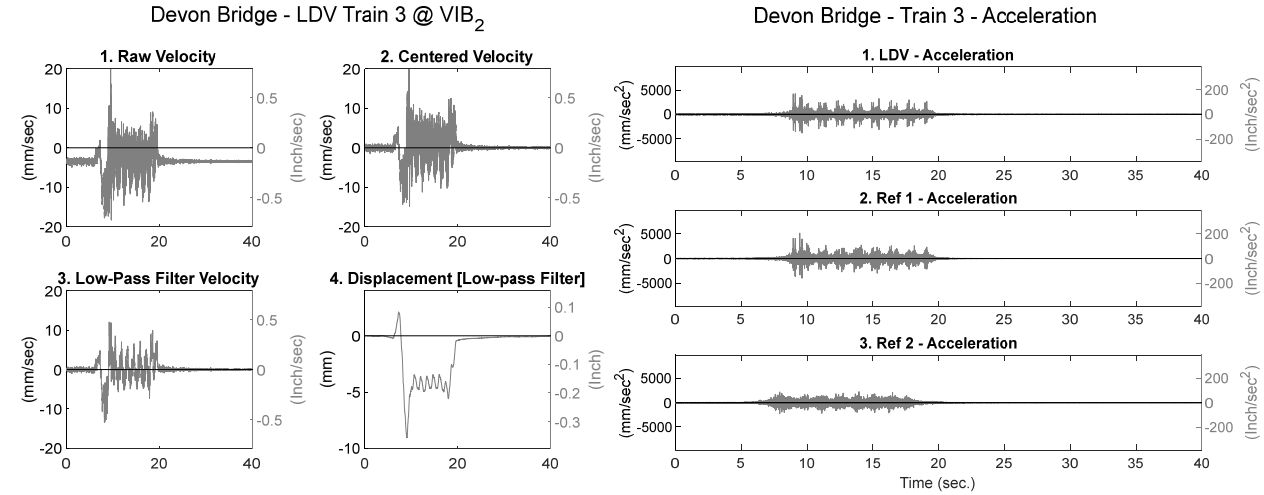

Figure A- 3: Train 3: Time variation data, velocity, displacement, and acceleration

Train 4: MTRR M8 composition with eleven couches, traveling East-West direction on track 4, and LDV data recorded at the vertical post node, denominated LDV 3.

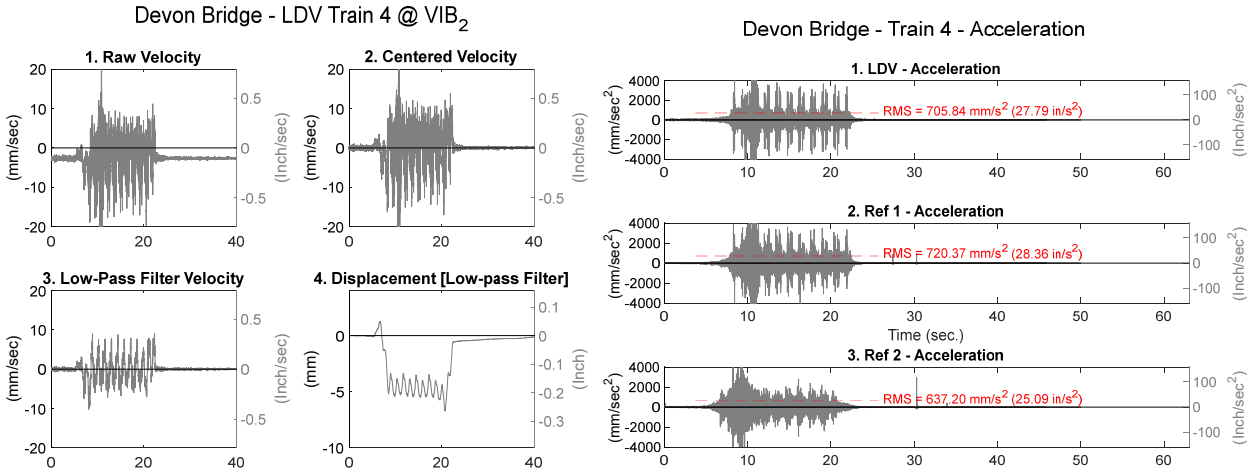

Figure A- 4: Train 4: Time variation data, velocity, displacement, and acceleration

Train 5: AMTK Acela composition with six couches and two power engines, traveling East-West direction on track 4, and LDV data recorded at the middle of the floor beam at hangars, denominated LDV 3.

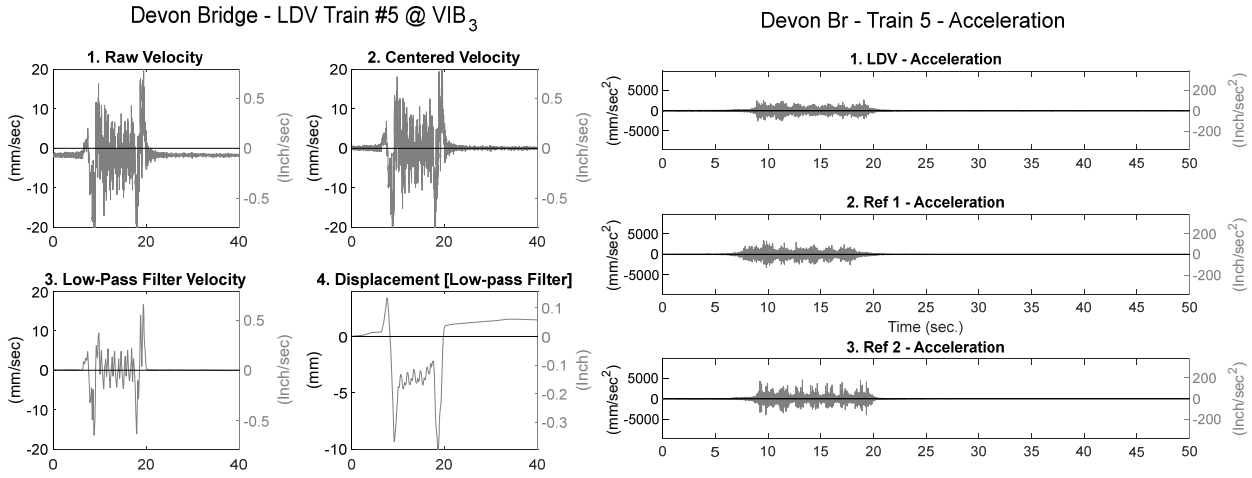

Figure A-5: Train 5: Time variation data, velocity, displacement, and acceleration

Train 6: Unknown freight train composition with eleven cars and couches and power engines, traveling East-West direction on track 2, and LDV data recorded at the middle of the floor beam at hangars, denominated LDV 4.

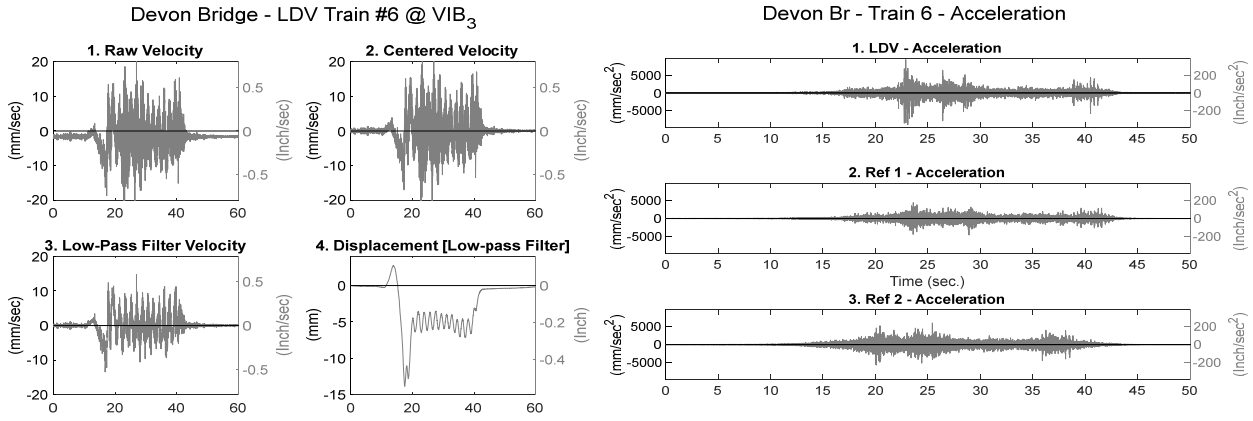

Figure A-6: Train 6: Time variation data, velocity, displacement, and acceleration

Train 7: Typical MTRR M8 composition with eight couches, traveling East-West direction on track 4, and LDV data recorded at the middle of the floor beam at hangars, denominated LDV 4.

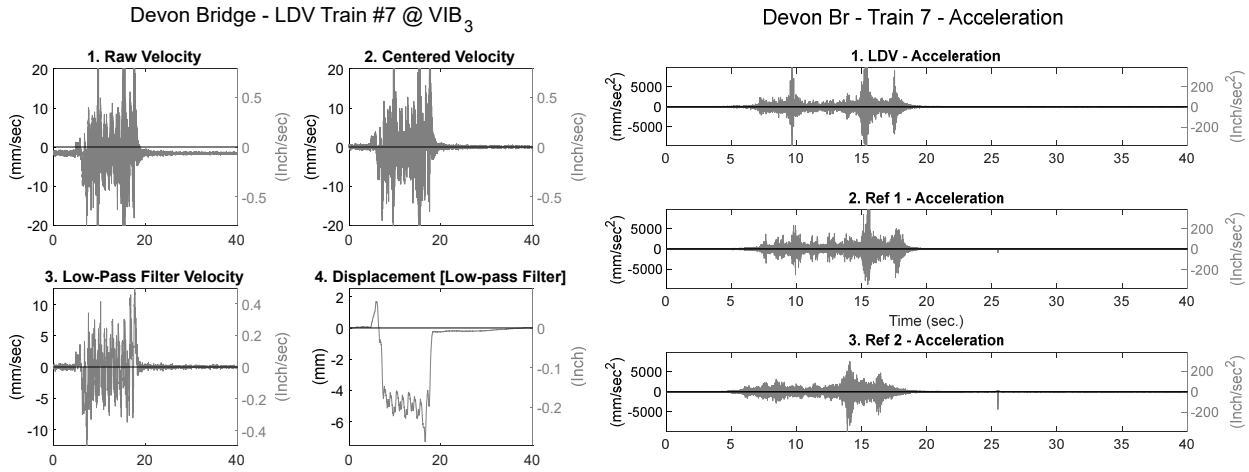

Figure A-7: Train 7: Time variation data, velocity, displacement, and acceleration

Train 10: Typical MTRR M8 composition with eight couches, traveling West-East direction on track 2, and LDV data recorded at the middle of the floor beam at vertical post, denominated LDV 4.

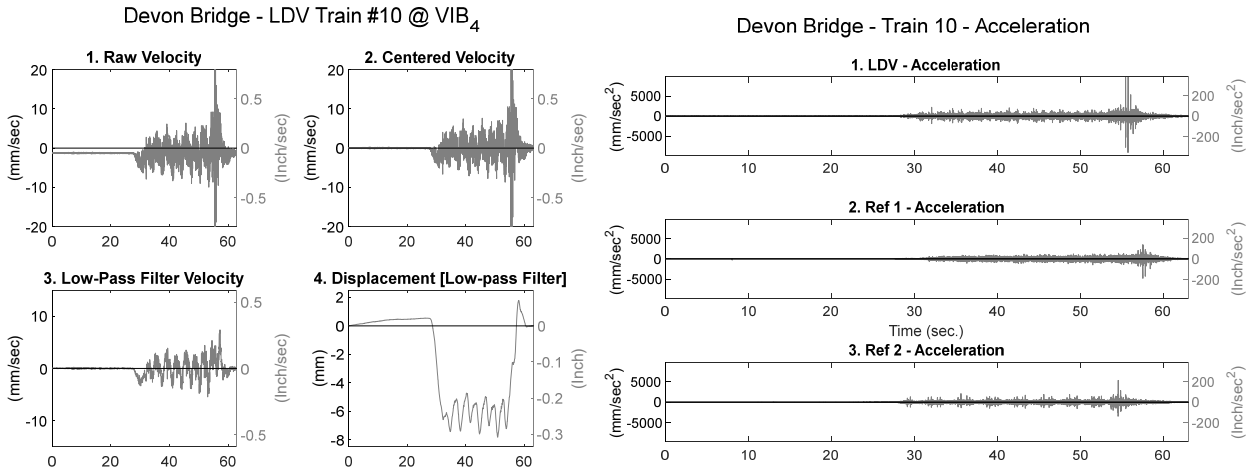

Figure A-8: Train 10: Time variation data, velocity, displacement, and acceleration

Train 11: Typical AMTK Regional composition with seven couches and power engine, traveling East-West direction on track 4, and LDV data recorded at the middle of the floor beam at hangars, denominated LDV 5.

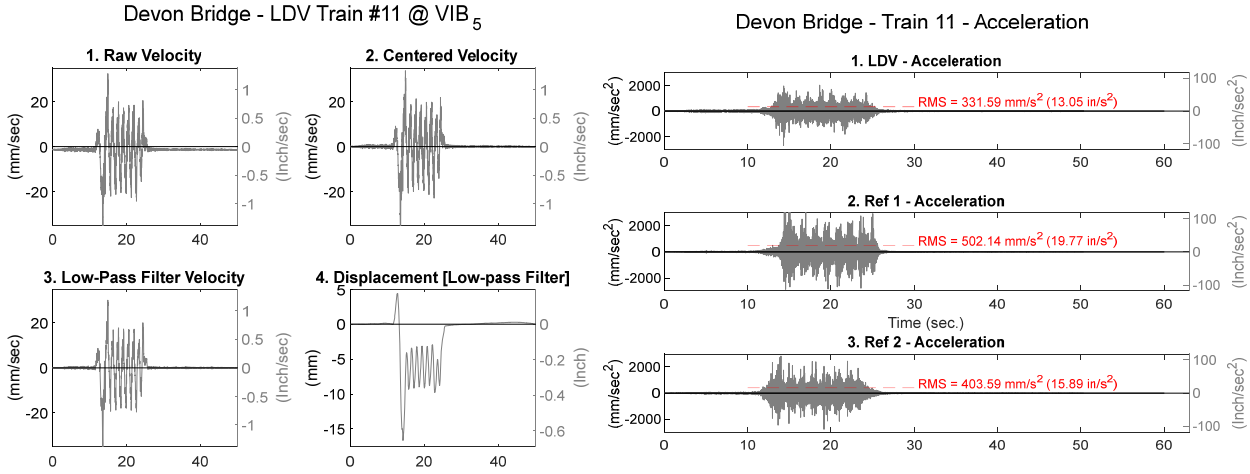

Figure A-9: Train 11: Time variation data, velocity, displacement, and acceleration

Appendix B: Cos Cob Bridge Field Measured Raw Data

The raw data recored on the Cos Cob Bridge processed to obtain results presented in the sub section 3.2.2.1 are presented in the Figure B-1 to B-9. Measured data includes vertical and the horizontal velocity-time and the acceleration-time response due to service loading of Amtrak Acela, Amtrak Regional and the Metro North trains at various speeds. See Figure 68 for the location of nodes (defined as Vib.1 Vib. 2 and so on).

LDV Vertical Response

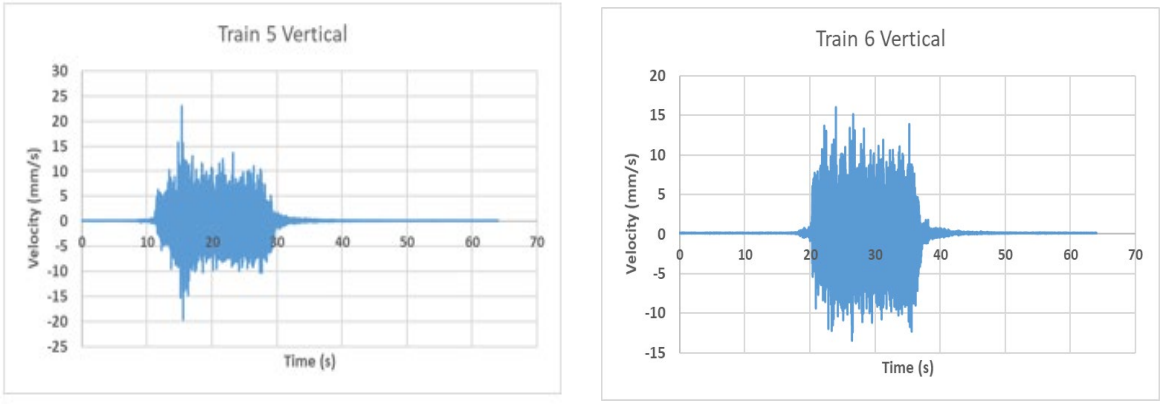

Figure B- 1: Velocity-time response at node Vib.1 under/subjected to 8-car Metro North train moving at 37.87 mph from New York to New Haven on track 4 of Cos Cob bridge, CT (left) and at node Vib.2 under/subjected to 8-car Metro North train moving at 42.41 mph from New York to New Haven on track 4 of Cos Cob bridge, CT.

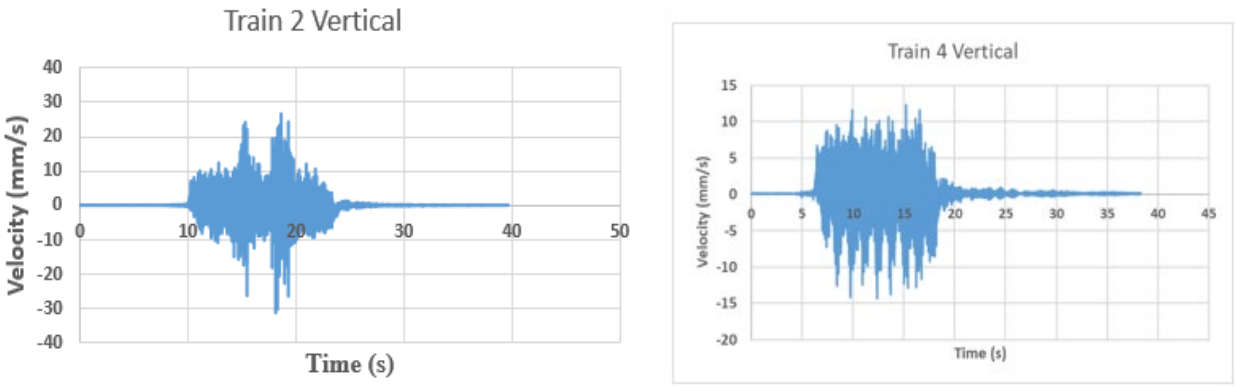

Figure B- 2: Velocity-time response at node Vib.3 under/subjected to 10-car Metro North train moving at 37.56 mph from New York to New Haven on track 4 of Cos Cob bridge, CT (left) and at node Vib.3 under/subjected to 10-car Metro North train moving at 39.98 mph from New York to New Haven on track 2 of Cos Cob bridge, CT. (right)

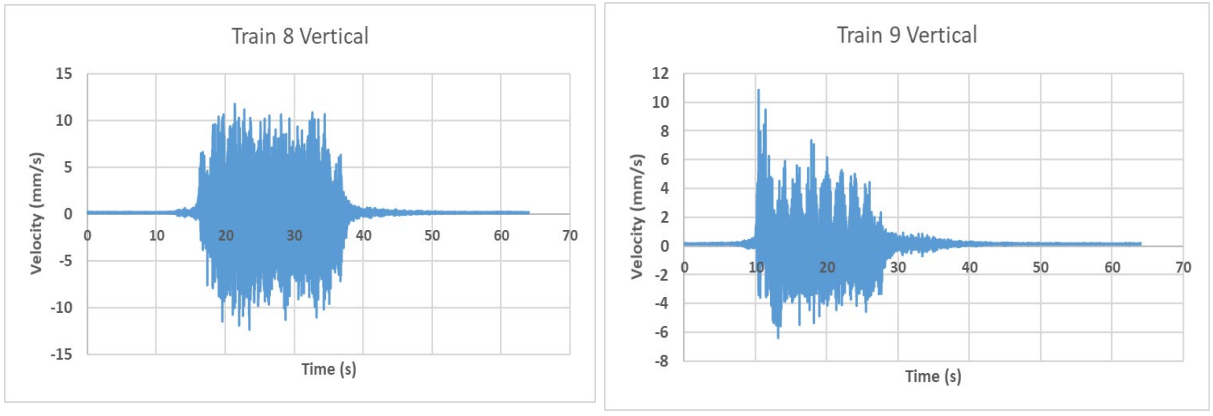

Figure B- 3: Velocity-time response at node Vib.4 under/subjected to 8-car Metro North train moving at 41.53 mph from New York to New Haven on track 4 of Cos Cob bridge, CT (left); and at node Vib.5 under/subjected to 8-car Amtrak Regional train moving at 28.07 mph from New York to New Haven on track 2 of Cos Cob bridge, CT. (right)

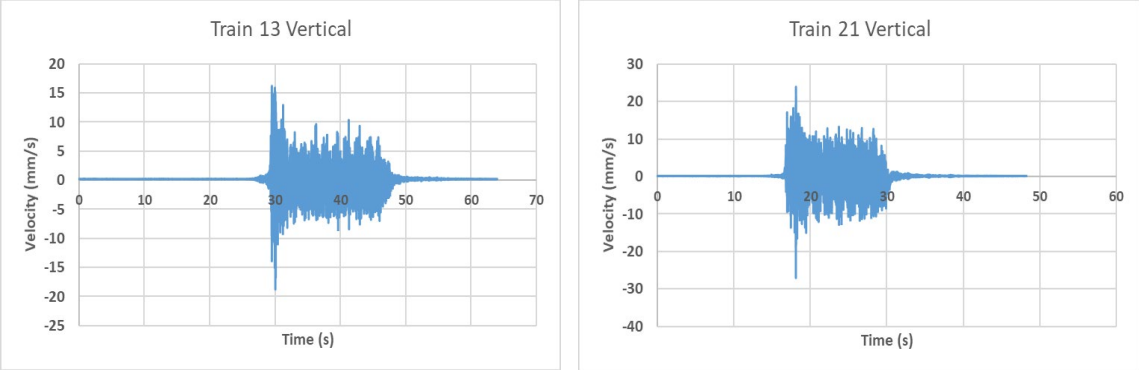

Figure B- 4: Velocity-time response at node Vib.7 under/subjected to 10-car Metro North train moving at 36.32 mph from New York to New Haven on track 4 of Cos Cob bridge, CT (left) and at node Vib.11 under/subjected to 8-car Metro North train moving at 37.85 mph from New York to New Haven on track 4 of Cos Cob bridge, CT. (right)

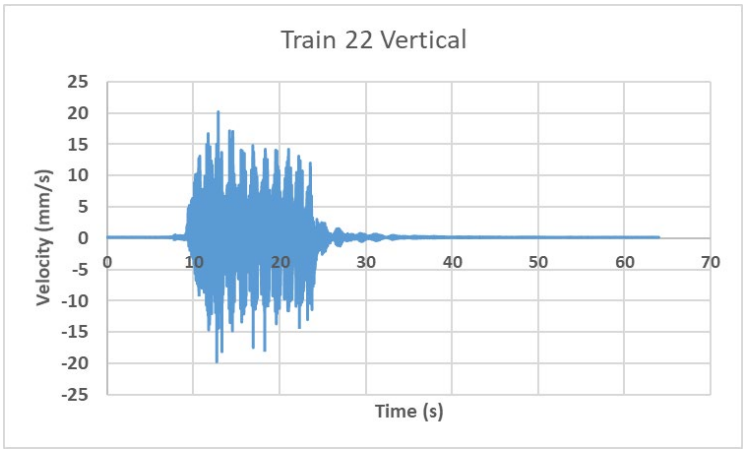

Figure B- 5: Velocity-time response at node Vib.7 under/subjected to 10-car Metro North train moving at 45.15 mph from New York to New Haven on track 4 of Cos Cob bridge, CT

LDV Lateral Response

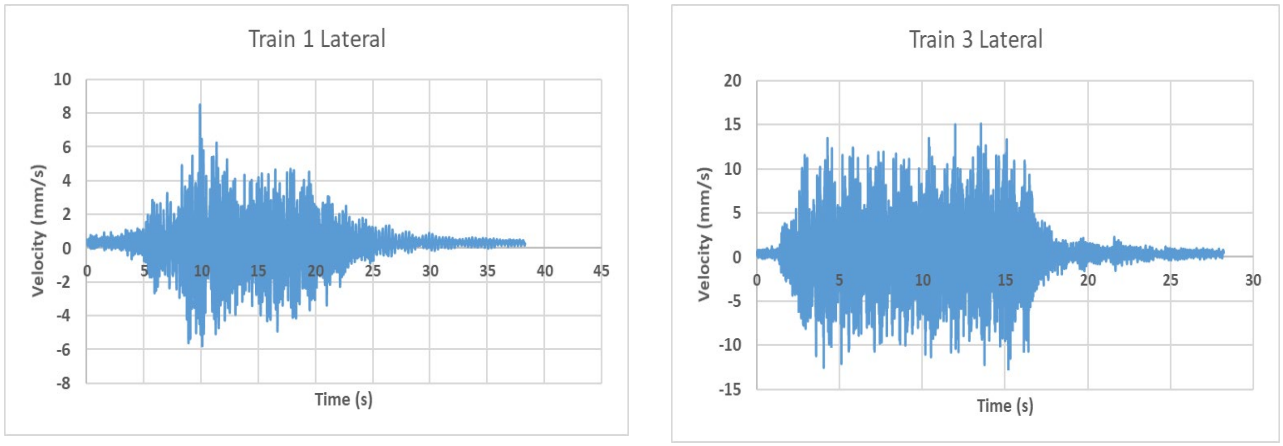

Figure B- 6: Velocity-time response at node Vib.5 under/subjected to Amtrak Acela train moving from New Haven to New York on track 3 of Cos Cob bridge, CT (left) and at node Vib.5 under/subjected to Metro North train moving from New York to New Haven on track 3 of Cos Cob bridge, CT. (right)

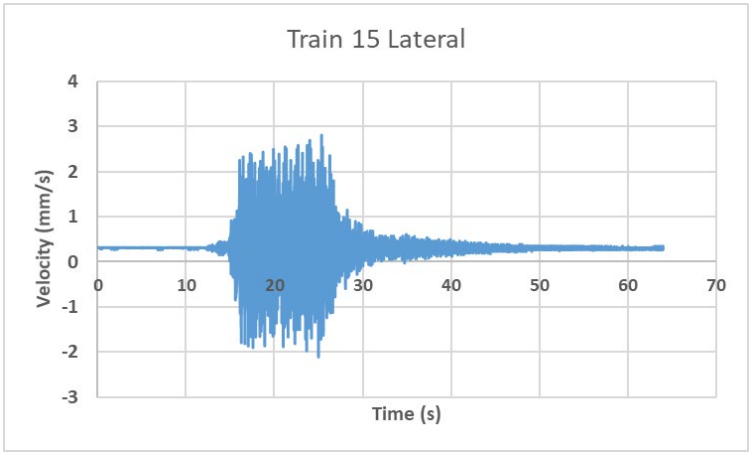

Figure B- 7: Velocity-time response at node Vib.3 under/subjected to 8-car Metro North train moving at 15 mph from New York to New Haven on track 4 of Cos Cob bridge, CT

Reference Accelerometer Data

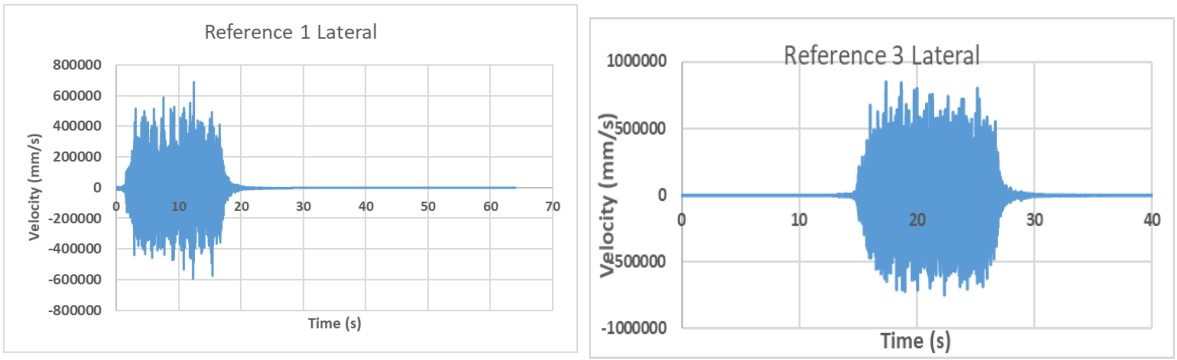

Figure B- 8: Lateral acceleration-time response (left reference 1; right: reference 3) under/subjected to 10-car Metro North train moving at 36.32 mph from New York to New Haven on track 4 of Cos Cob bridge, CT

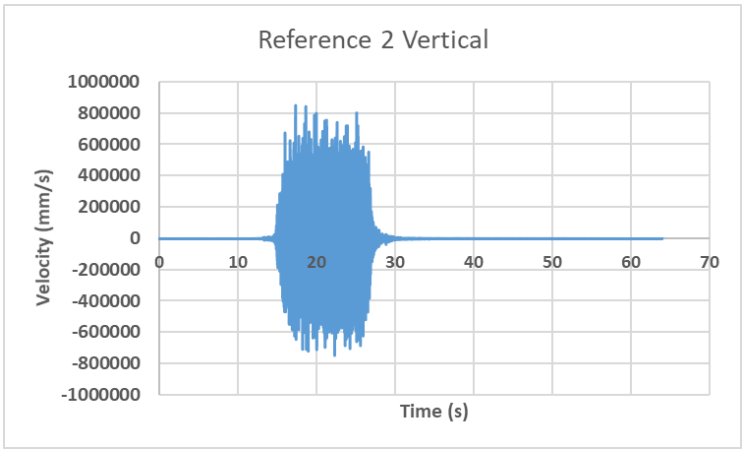

Figure B- 9: Vertical acceleration-time response for reference 2 under/subjected to 10-car Metro North train moving at 36.32 mph from New York to New Haven on track 4 of Cos Cob bridge, CT

Transportation Infrastructure Durability Center
AT THE UNIVERSITY OF MAINE

35 Flagstaff Road
Orono, Maine 04469
tidc@maine.edu
207.581.4376

www.tidc-utc.org